DEVELOPMENT OF PLATINUM ALLOYS FOR HIGH-TEMPERATURE SERVICE

by

Graham Bruce Fairbank

Department of Materials Science and Metallurgy

Darwin College

Cambridge

A dissertation submitted for the degree of Doctor of Philosophy
at the University of Cambridge

Preface

This dissertation is an account of research undertaken between October 1997 and March 2003 in the Department of Materials Science and Metallurgy under the supervision of Professor Colin Humphreys, and is submitted to the university of Cambridge in fulfilment of the requirements of the University for the degree of Doctor of Philosophy.

The work described is of the author alone, except where due reference is made to the work of others and any work done in collaboration. No part of this dissertation has been or is being currently submitted for any other degree, diploma or qualification at this or any other university. This dissertation is less than 60000 words in length.

Parts of this work have been published or have been submitted for publication in the following papers:

1. G. B. Fairbank, C. J. Humphreys, A. Kelly, and C. N. Jones, Ultra-high temperature intermetallics for the third millennium, Intermetallics **8** (2000) 1091-1100

2. G. B. Fairbank, C. J. Humphreys, and C. N. Jones, New platinum alloys for ultra high temperature applications, *Paper presented to the Fifth International Charles Parsons Turbine Conference, Cambridge, 3-7 July 2000*

3. G. B. Fairbank, C. J. Humphreys, B. Roebuck, and C. N. Jones, Properties and phase equilibria of Pt-Rh-Hf alloys, *Paper presented at HTM2001 Conference in Tsukuba, Japan, and to be published in Materials Science and Engineering A*

4. P. J. Hill, G. B. Fairbank, and L. A. Cornish, New developments in high-temperature platinum alloys, JOM **53** (2001)

Acknowledgements

I would like to thank Professors Colin Humphreys, Alan Windle and Derek Fray for the provision of laboratory facilities and office space during my time in the Department. Professor Humphreys has been an understanding and generous supervisor, and for this I am most grateful. I also wish to thank Neil Jones from Rolls Royce for his time and assistance with the program of work.

Funding for this work came from several sources – the EPSRC (through a Foresight Challenge Grant), the Cambridge Australia Trust, and the Overseas Research Scholarship Fund. I also wish to acknowledge the generous provision from NIMS in Tsukuba, Japan, that allowed a visit to the research group of Prof. Hiroshi Harada.

Material for the work was loaned by the Platinum Development Initiative of South Africa, and I must thank the two chairpeople who saw fit to arrange for the material loan – Dr Ira Wolff and Dr Lesley Cornish. I also send a special thankyou to the staff at MINTEK, particularly Drs Wolff, Cornish, Cortie and (especially) Dr Patricia Hill, who have been a constant source of enthusiasm and encouragement.

I also wish to thank the many technical staff whose valuable assistance has been greatly appreciated, particularly Andrew Moss and Mary Vickers for XRD help, David Duke and Nathan Cliff for keeping things running smoothly, Kevin Roberts for the alloy melting and heat treatment assistance, and Robin Taylor, David Nicol and David Vowles for the assistance with the various electron microscopes. Thanks are also to thank Dr. Bryan Roebuck at NPL, for use of the ETMT.

I must give special mention to those who have made my time in Cambridge so enjoyable – Sarah and Ron, whom I shared an office with, the various squash opponents from the department, and all the folks in Darwin College.

And a very special thanks to my beautiful wife, Kirsteen, for her patience and support.

Abstract

This dissertation describes the results of investigations carried out by the author into the alloying behaviour and high temperature mechanical properties of a number of binary and ternary systems based on Pt. The main focus of the investigation was to determine whether two-phase superalloy analogues based on Pt could be produced, and whether these alloys had any potential as a turbine material.

An examination of the phase equilibria of the Pt-Hf and Pt-Zr systems (chosen due to the possibility of producing a two-phase f.c.c. – $L1_2$ ($\gamma - \gamma'$) alloy, analogous to the Ni-base superalloys) led to the discovery of a new compound, Pt_8Hf, and confirmation of the existence of the compound Pt_8Zr. The presence of these two phases eliminates the possibility of producing a superalloy analogue in either binary system. In addition to the above compounds, the existence of a non-stoichiometric $L1_2$ intermetallic (γ') was also confirmed in both systems. The existing Pt-Zr binary phase diagram was modified on the basis of these results, and the Pt-Hf binary phase diagram was plotted for the first time.

Formation of the low temperature phases Pt_8Hf and Pt_8Zr was suppressed by the addition of Rh, and in the Pt - Rh - Hf and Pt - Rh - Zr systems a $\gamma - \gamma'$ two-phase field was identified. Tentative isothermal sections of the ternary phase diagrams of both the Pt - Rh - Hf and Pt - Rh - Zr systems were suggested. In addition to these two systems, the Pt-Ti-Cr system was also investigated. It was found that the two γ' intermetallics Pt_3Ti and Pt_3Cr were likely to be connected, such that a $\gamma - \gamma'$ alloy could be produced in the Pt-Ti-Cr system.

The high temperature mechanical properties of a Pt - Rh - Hf alloy and a Pt - Ti - Cr alloy were investigated. The Pt - Rh - Hf alloy consisted of γ' precipitates in a γ matrix, whilst the Pt - Ti - Cr alloy tested was in the as-cast condition and contained dendrites of γ' ($Pt_3(Ti,Cr)$) in a γ matrix. The composition Pt – 8.5 at%Rh – 17 at%Hf was found to possess higher proof stress over the temperature range investigated (1000 °C – 1500 °C) than other known single-phase and two-phase Pt alloys. The Pt - Ti - Cr alloy had far lower proof stress than the Pt - Rh - Hf alloy over the same temperature range. The Pt - Rh - Hf alloy was also shown to have promising creep resistance, when compared to other Pt-based alloys designated for high temperature service.

Contents

Development of Platinum Alloys for High-Temperature Service

Graham Bruce Fairbank

This dissertation describes the results of investigations carried out by the author into the alloying behaviour and high temperature mechanical properties of a number of binary and ternary systems based on Pt. The main focus of the investigation was to determine whether two-phase superalloy analogues based on Pt could be produced, and whether these alloys had any potential as a turbine material.

An examination of the phase equilibria of the Pt-Hf and Pt-Zr systems (chosen due to the possibility of producing a two-phase f.c.c. – $L1_2$ ($\gamma - \gamma'$) alloy, analogous to the Ni-base superalloys) led to the discovery of a new compound, Pt_8Hf, and confirmation of the existence of the compound Pt_8Zr. The presence of these two phases eliminates the possibility of producing a superalloy analogue in either binary system. In addition to the above compounds, the existence of a non-stoichiometric $L1_2$ intermetallic (γ') was also confirmed in both systems. The existing Pt-Zr binary phase diagram was modified on the basis of these results, and the Pt-Hf binary phase diagram was plotted for the first time.

Formation of the low temperature phases Pt_8Hf and Pt_8Zr was suppressed by the addition of Rh, and in the Pt-Rh-Hf and Pt-Rh-Zr systems a $\gamma - \gamma'$ two-phase field was identified. Tentative isothermal sections of the ternary phase diagrams of both the Pt-Rh-Hf and Pt-Rh-Zr systems were suggested. In addition to these two systems, the Pt-Ti-Cr system was also investigated. It was found that the two γ' intermetallics Pt_3Ti and Pt_3Cr were likely to be connected, such that a $\gamma - \gamma'$ alloy could be produced in the Pt-Ti-Cr system.

The high temperature mechanical properties of a Pt-Rh-Hf alloy and a Pt-Ti-Cr alloy were investigated. The Pt-Rh-Hf alloy consisted of γ' precipitates in a γ matrix, whilst the Pt-Ti-Cr alloy tested was in the as-cast condition and contained dendrites of γ' ($Pt_3(Ti,Cr)$) in a γ matrix. The composition Pt – 8.5 at%Rh – 17 at%Hf was found to possess higher proof stress over the temperature range investigated (1000 °C – 1500 °C) than other known single-phase and two-phase Pt alloys. The Pt-Ti-Cr alloy had far lower proof stress than the Pt-Rh-Hf alloy over the same temperature range. The Pt-Rh-Hf alloy was also shown to have promising creep resistance, when compared to other Pt-based alloys designated for high temperature service.

Chapter 1 Introduction

1.1 The Need for New Ultra-High Temperature Materials

Much attention has been given in recent years to the search for, and development of, materials capable of operating in structural components at temperatures above 1000 °C. Such materials may have many exotic applications in spacecraft (e.g. thruster rocket nozzles) and less exotic ones in manufacturing (such as in chemical processing), but much of this development is being driven by the aeroengine industry. As there are approximately 13,500 commercial aeroplanes in operation [1], spending up to 80 % of the time in the air, their fuel consumption is significant and airlines are constantly looking for ways to reduce their fuel bill. One way to reduce this is through engine design, specifically by increasing the turbine entry temperature (TET), which at present is limited by achievable material properties.

The historical development [2] of turbine entry temperature (TET) is shown in figure 1.1. The general trend is upwards with time, and developments in materials processing and chemistry have enabled blades and vanes to operate in gas streams above the melting point of the material from which they are made. Recent developments, such as thermal barrier coatings, might give rise to another step change, though some efforts to increase temperature capability of a component incur a cost and efficiency penalty [2]. Developments since Whittle's first engine include the removal of all grain boundaries, development of vacuum casting, inclusion of heavy and expensive elements, use of cooling air within the blade (resulting in increased complexity of blade architecture and manufacture) and, more recently, trial of thermal barrier coatings (a thermally-sprayed porous ceramic) [2].

The thermodynamic reason for the upwards trend in figure 1.1 toward higher temperatures is not driven by overall efficiency gains [2] (see figure 1.2) but by thrust considerations [2] (see figure 1.3). Figure 1.2 shows that the overall efficiency of the engine, given by the product of propulsive and cycle efficiencies, is essentially constant at TETs above 1600 K.

Propulsive efficiency is positively influenced by increasing the "bypass ratio" (BPR) of the engine – the ratio of air passing through the fan and out of the bypass vents compared to that going through the fan and turbine. Modern commercial engines have bypass ratios up to 9 [2], which is why they are commonly called "turbofan" engines – the fan in front provides up to about 80 % of the thrust, with only a small component coming from the gas expanding through the turbine. In contrast, figure 1.3 shows that the thrust output of the engine is a linear function of temperature, and that any increase in temperature will increase the thrust.

The main reason for increasing the turbine entry temperature is to produce more work from a given fuel flow rate [3] (as shown in figure 1.4), which has a desirable influence on the thrust-specific fuel consumption. For example, referring to figure 1.4, one can see that for an increase in turbine entry temperature from 1600 °C to 1800 °C at a BPR of 9, the thrust-specific fuel consumption decreases by approximately 0.02 kg of fuel per kilogram of thrust per hour (equivalent to a 3 % decrease). This results from an increase in gas turbine work (see figure 1.3) of approximately 20 % over the same temperature range.

The main US funding organisations emphasised the importance of this area of superalloy and turbine material research by describing a set of revolutionary objectives in 1984 for future turbine materials (specifically hot section components) [3]. These were initially too optimistic for the near term and were revised to targets that implied an increase in specific creep strength to 1.5 - 1.8 times that of existing (in 1984) materials and a TET of 3000 - 4000 °F (as stoichiometric combustion occurs at close to 4000 °F). This was to be obtained partly through density reductions and partly through operating temperature gains. While lowering density is desirable while maintaining other properties (such that weight savings are realised in (e.g.) the blade itself), there will also be an associated reduction in the weight of the support structure and hence a larger decrease in weight of the whole turbine [4].

An additional goal of the US funding organisations was to design materials capable of operating in any atmosphere, as current materials are designed to withstand oxidising and

neutral atmospheres only [3]. Reducing atmospheres have grave consequences for current turbine materials, and Sims [3] gives the example of blades "burning off" in less than a minute when a faulty combustor produced a reducing atmosphere in the turbine.

Nathal and Levine [5] described the six most important properties of a turbine material as being:

1. Operating temperature (which is to a large extent linked to melting temperature);
2. Specific high-temperature strength or creep life;
3. Toughness at all temperatures, and most significantly, at room temperature;
4. "processablility";
5. thermal conductivity; and
6. oxidation resistance.

The first property is easily explained - to cope with a high operating temperature the material must have an even higher melting temperature. Coatings and advanced cooling allow the Ni-base superalloys (NBSAs) to operate in a gas stream well above their melting temperature (T_m), but there are limits to how much benefit can be realised by this method (due to the properties of the coating and negative effect of blade cooling on engine efficiency).

The second property is essential for load-bearing components such as turbine blades. Toughness is a requirement for three reasons. At room temperature, the engine must be able to be assembled with component damage. At operating temperatures, the component must be able to withstand impact at high speed from debris passing through the engine. The third reason is the need to withstand thermal stresses, induced by thermal gradients in the blade.

The third property, processability, is the requirement for the material to be able to be processed to the desired shape reasonably easily and reproducibly without incurring large costs. Current turbine blades are cast single-crystal alloys, but without a suitable liquidus

range, heat-treatment window, or suitable mould materials, they would not be able to be produced in the shape desired.

High thermal conductivity is a requirement for many reasons, including assisting cooling effectiveness, and minimising the effect of "hot spots", thereby avoiding local melting and minimising thermally-induced stresses. These stresses arise through variations in thermal expansion of the material with temperature.

The last attribute is essential - while materials can be protected to some extent by coatings, any flaw will reveal the underlying substrate and cause substrate oxidation. If the blade oxidises excessively then material loss and component failure will result.

With the NBSAs approaching an obvious temperature limit, research into other materials as potential replacements is being conducted in six main areas. Sims [3] identified several of these as being worth pursuing, whereas some are relatively new fields or resurrections of old work. They are:

1 Refractory Metal Alloys;

2 Intermetallics;

3 Monolithic Ceramics;

4 Carbon Matrix Composites;

5 Ceramic Matrix Composites; and

6 Platinum Group Metal (PGM) alloys.

The first five of these will be briefly described in sections 1.2.1-1.2.5, whilst the sixth will be discussed in detail later in this chapter in section 1.4.

1.2 High Temperature Materials

1.2.1 Refractory Metal Alloys

Of all metallic materials, the refractory metal alloys show the most promise as successors to the NBSAs in hot-section components within the gas turbine. There was great interest in alloys of Re, Nb, W, Cr, Ta and Mo in the 1960s, when investigators examined the strength of single-phase alloys and the pure metals. Their poor oxidation resistance was also discovered during this period, and recent attention has been quite limited in most cases, with the two notable exceptions being Nb and Re.

1.2.1.1 Alloys of Re

Alloys of Re possess excellent strength and creep resistance [6] due to their very high melting points (in the region of 3000 °C). Whilst Re suffers catastrophic failure due to oxidation at high temperatures, this can be overcome to some extent by coating with a ceramic, such as Al_2O_3, a high-MP intermetallic such as Pt_3Zr [7] or a pure metal such as Ir. Rocket nozzles and thrust chambers have been successfully fabricated from Ir-coated Re, which exhibit good performance for short periods [8].

1.2.1.2 Alloys of Nb

In recent years there has been great interest in the potential of Nb alloys as replacements for the NBSAs in temperature-critical components within gas turbines. Most of this work has been conducted at General Electric in the USA and at the US Air Force Wright Laboratory, though more recent work has been conducted in Japan.

The series of publications by Jackson and Subramanian [9-12] detail the GE / Wright program. Their investigations have focussed on the use of Nb_3Si and Nb_5Si_3 as the strengthening precipitates in a Nb matrix. This system was chosen over $MoSi_2$-based alloys (a competing promising candidate) due to its lower density, better (but not always

adequate) oxidation resistance, higher toughness and better fatigue behaviour. These Nb alloys have melting points in excess of 1700 °C, a density of approximately 7 g/cm^3 and fracture toughness of greater than 20 MPa.m$^{1/2}$, indicating great potential should the mechanical and oxidation properties be sufficient. The presence of the Si leads to a glassy silicon oxide phase on the surface in oxidising atmospheres, but the penetration of binary Nb - Si alloys by oxygen is high and other elements such as Cr and Al must be added to modify the oxidation behaviour. Addition of these elements, however, degrades the creep performance of the alloy, and other elements must be added to strengthen the (Nb) matrix. This has led to complex alloys containing some or all of Ti, Hf, Si, Al, Cr, Mo, Ta, W, Sn and Ge.

It has been shown [9] that for good oxidation resistance the Nb : (Ti + Hf) ratio should be 1.8 - 2.1, and that the Si content should be 17 - 19 at%. A high Si content is also desirable for creep resistance, as are solid-solution strengthening elements such as Mo, Ta and W. The amount of these transition metals should be kept quite low (typically < 2 %) so as not to affect oxidation performance. The elements Ge and B may be substituted for some of the Si without detrimental effect on oxidation behaviour whilst improving creep properties. The problem of "pesting" (preferential oxidation at microstructural features, such as grain boundaries) can be eliminated in the 750 °C - 950 °C regime by small additions of Sn (1.5 at%) without affecting oxidation behaviour at 1200 °C.

Alloys have been produced [9] that are superior in terms of oxidation and creep performance to NBSAs, though they do not meet the targets of the GE / Wright program. The creep target of the program is less than 1 % creep deformation in 125 h at 1200 °C under an applied stress of 175 MPa (presumably in air), whilst the oxidation target at 1315 °C is to match the long-term material loss experienced by coated NBSAs at 1150 °C. No single alloy has yet been produced which meets both targets, though the creep goal has been demonstrated in several binary and higher systems. The material loss target has been achieved at 90 °C below the temperature target in the best-performing alloy. It is thought, though, that any alloy operating at the elevated temperatures envisaged will require coating.

Several coating compositions have been investigated, and will probably be based on $MoSi_2$ with additions of W, B and/or Ge. These coatings have excellent oxidation resistance, are adherent to a bond coat, non-spalling, self-healing, and do not react with the substrate.

The Nb alloy work described above is very promising and shows great potential for allowing the turbine entry temperature of the gas turbine to increase through materials development. There may be several problems, however, with processing of these alloys. Due to their high melting points, interaction with ceramics in the mould and crucible during casting is likely and special coatings on these components will be required. In addition, Balsone [12] *et al* argue that the (typically) 5-year development cycle of engines, being much shorter than that of new materials (10 years), is a barrier to introduction of new materials, especially ones such as these Nb alloys which are quite different in nature to the NBSAs to which engine designers are accustomed.

The research in Japan [13] has picked up on the above work, focussing on the relationship between processing routes and the resultant mechanical properties of the alloys. Sha and co-workers have produced directionally solidified alloys with the composition Nb - 10 %Mo - 10 %Ti - 18 %Si - (0-15) %W, and performed compression tests at room temperature, 1670 K and 1770 K. The microstructures produced comprised, in all cases, (Nb) + Nb_5Si_3. The hardness and proof stress were shown to be strong functions of tungsten content. Hardnesses of 700 HV1 (0 %W alloy) to 850 HV1 (15 %W alloy) at room temperature were measured, and similar strength gains were observed in the elevated temperature mechanical tests. The 15 %W alloy has compressive proof stresses of 900 MPa and 600 MPa at 1670 K and 1770 K respectively, gains of 55 % and 150 % respectively over the 0 %W alloy. The oxidation properties of these alloys were not reported, though as the W levels should be kept below 2 % so as not to affect oxidation performance (see above), it is possible they will suffer oxidation problems.

Ma and co-workers [14] have produced binary Nb-Si alloys by ball-milling and reactive hot pressing. The microstructures produced after hot pressing were very fine, with phase

sizes in the region of 1 μm. They found that the compressive proof stress at 1773 K after hot pressing was 20 - 30 MPa in all cases (for Si contents of 3.5 - 16 at%), and that room-temperature strength was a strong function of Si content, increasing from 950 MPa at 3.5 %Si to 1850MPa at 16 %Si. The high-temperature strength was improved by high-temperature annealing (for example, annealing at 2073 K improved the 1773 K proof stress of the 16 %Si alloy from 23 MPa to 100 MPa). This was attributed to the larger grains present after annealing leading to a decrease in grain boundary sliding. When compared to the results of Sha, the proof stress of the binary alloys investigated by Ma *et al* are far lower at 1773 K.

Despite the mixed results, the above work is very encouraging. If the creep - oxidation resistance trade-off can be satisfactorily resolved, then (assuming all other requirements are met) Nb alloys may appear in service towards the end of this decade.

1.2.2 Intermetallics

This category encompasses transition metal aluminides, carbides and silicides, as well as miscellaneous high-MP intermetallic compounds such as RuAl and IrAl.

The best-known intermetallic compound is probably Ni_3Al, which is responsible for the excellent performance of the NBSAs, it being the strengthening precipitate. Ni_3Al exhibits the curious “yield strength anomaly” whereby its yield strength increases with increasing temperature over the range 600 - 1000 K before peaking and falling again. This is opposite to the behaviour of pure metals, most alloys, and many intermetallics, which soften continuously with increasing temperature. Kear and Wilsdorf, using the mechanism of "Kear-Wilsdorf" locks, have adequately explained the anomalous yield strength relationship described above [15].

According to Kear and Wilsdorf, above about 400 °C, ½ <011>{111} glide dislocations in γ' become susceptible to thermally activated cross-slip onto {001} glide planes ("cube slip"). Some sections undergo cross-slip onto {001} and back onto {111}, leaving behind

sessile 'kinks' of <011>{001} dislocations. These kinks can only move via diffusion at these temperatures, and consequently cause rapid work hardening of the alloy. At a temperature of about 700 °C the sessile segments become mobile under stress, causing the locks to be lost, and the alloy reaches a strength peak at approximately 800 °C and then softens continuously up to its melting temperature [12].

Despite this hardening with increasing temperature, the melting point of Ni_3Al is too low to be considered for use at temperatures much above those at which the NBSAs currently operate. The same is true of TiAl, which is being examined for lower-temperature applications. In contrast, the compound NiAl has been receiving more attention in recent years, due to its higher melting point and range of attractive properties [16]. Two other high melting point intermetallics that have generated interest in recent years are RuAl and IrAl.

1.2.2.1 NiAl

This compound is very interesting due to its high MP (1638 °C), lower density than NBSAs (5.35 - 6.50 g/cm^3), good environmental resistance and good thermal conductivity [16]. Despite these advantages, its room temperature ductility is poor - in single crystals, failure occurs in the elastic region along the "hard" <100> direction while along the "soft" <110> direction ductility is only about 2 % [17]. Small additions of some elements (Fe, Ga, Mo) have been shown to increase ductility to as much as 6 %. The material also has a ductile-to-brittle transition at approximately 400 °C, above which the ducilitity can be as high as 40 %.

The temperature dependence of the proof stress of NiAl is shown in figure 1.5. It can be seen that, despite the high melting temperature of NiAl, its proof stress is only as good as the superalloy Rene 80 [16]. However, addition of 0.2 %Hf can improve the high-temperature strength several times, as demonstrated in the same figure.

The creep deformation of single-crystal and polycrystalline NiAl is also much higher than for Rene 80. When density is taken into account (in specific creep strength), NiAl is found to be equivalent to Rene N4 in specific stress-rupture life [17].

The addition of a second phase (such as a Heusler phase) also has a dramatic effect. In directionally-solidified eutectics of NiAl + α-(Cr, Mo or both), sometimes with a Ta-rich Laves phase as well, the toughness is much improved for a slight decrease in creep resistance [17].

At present, however, the major factor limiting the potential of NiAl in all forms is its low-temperature impact strength [16,17].

1.2.2.2 RuAl

This material is unusual among intermetallic compounds in that it has both room-temperature toughness and reasonable high-temperature oxidation resistance. In publications beginning a decade ago [18-21], Fleischer and co-workers describe the effects of stoichiometry and ternary additions on the mechanical properties and oxidation resistance of RuAl, and that the best mechanical properties are obtained in alloys with a slight excess of Ru and some Sc substituted for the Al. An alloy with the composition $Ru_{52}Al_{48}$ was shown to have a room-temperature proof stress of 620 MPa, a maximum stress of 1620 MPa, and compressive strain to fracture of 13 %.

Further research was conducted by Wolff and Sauthoff [22-25], who looked at substitution of Ru by less expensive elements such as Ni and Co. Small amounts of Ni were shown to have no deleterious effects, but no high-temperature results were reported. In addition, they produced alloys with a grain boundary ("necklace") phase, which substantially improved proof stress without degrading the ductility.

1.2.2.2.1 Ru - RuAl two-phase alloys

The B2 compound RuAl has a melting point of 2060 °C and forms a eutectic at 1920 °C with Ru (which is hexagonal) [18]. A microstructure can be formed such that there is a compliant grain-boundary layer composed of the Ru – RuAl eutectic with primary dendrites of RuAl. This compliant layer increases strength substantially up to approximately 0.5 T_m [18], above which the strength falls fairly rapidly due to interfacial sliding. Substitution of Ni and Sc can improve the strength further but not avoid the strength drop [21,22]. Fine dispersions of Ru in RuAl can be achieved by reactive hot isostatic pressing of the alloy powder [25], and this improves strength in the region 1000 – 1300 °C.

1.2.2.3 IrAl

IrAl is isostructural with RuAl but has a higher melting point (2120 °C) and has a higher eutectic temperature (2000 °C) when in equilibrium with Ir [22]. The strength of this system is quite high: $Ir_{70}Al_{30}$ has a proof stress of 250 MPa at 1300 °C. The drawback, however, is the poor environmental resistance at high temperatures of Ir. It has been determined that at 1400 °C a minimum of 55 at%Al is required for formation of a protective alumina scale [26,27].

1.2.3 Monolithic Ceramics

1.2.3.1 SiC

Silicon carbide is already in use at high temperatures in applications such as furnace elements [28]. It is an attractive material due to its low density (3.2 g/cm^3), useful strength over a wide temperature range (320 MPa at 25 °C and at 1350 °C) and excellent oxidation resistance up to 1400 °C. Above this temperature, however, the glass that forms on the surface is viscous enough to flow, resulting in continuous oxidation of the material [28].

A drawback to the material is its brittleness. As processing is normally by the powder route, pores are particularly common and failure generally initiates at these flaws. Sintering aids (such as Al_2O_3 and MgO) which fill these pores may be added to alleviate this problem to some extent [28], but other impurities lead to low melting point intergranular phases.

1.2.3.2 Si_3N_4

Silicon nitride has been generating a lot of interest in recent years [28]. Its low density (3.22 g/cm^3), excellent strength (430 MPa at 1100°C) and protective glassy surface in oxidising environments (like SiC) indicate that it is likely to be useful as a high-temperature material [28]. Again, it is processed via the powder route, and low melting point phases again may form at the grain boundaries if impurities are present. The impact resistance of the polycrystalline material is generally poor, though modification of the aspect ratio of the grains can improve it to some extent [29].

In 1996 Easley and Smyth [29] reported initial engine tests of Si_3N_4 nozzles totalling 910 h, with blade testing planned for 1998. While the blades performed well in most respects, it was found that they were very sensitive to friction via rubbing against the shroud seal.

Recent research at NIMS in Tsukuba, Japan [30] has investigated additions of a high melting point, low volume fraction constituent to act as a grain boundary phase, and in initial work the chosen addition was $Yb_4Si_2O_7N_2$. Little research had been carried out on the high-temperature strength, creep and oxidation behaviour at the time of publication of the article, but this work was planned for the next few years.

1.2.4 Ceramic Matrix Composites

1.2.4.1 Mullite ($3Al_2O_3.2SiO_2$ to $2Al_2O_3.SiO_2$, MP = 1828 °C)

Clegg, Kelly and Pitchford [31] have demonstrated the remarkable creep resistance of mullite, which is an "in-situ" composite. Single crystals of mullite consist of regions of stoichiometrically correct material and of oxygen-depleted material. The oxygen-depleted regions are a result of the presence of Al, substituting for Si, which means oxygen must be removed to balance the electronic charge. The presence of these regions is thought to lower overall free energy (though this depends on their size), which means there is no driving force for coarsening of these regions. These local disruptions might be expected to improve the mechanical properties by impeding dislocation progress. Additionally, the effective diffusion coefficient has been shown to be extremely low in polycrystalline material (based on creep rate measurements) when compared to other ceramics such as pure Al_2O_3, spinel and ThO_2, which is thought to result from the unusual microstructure. No creep was observed after 200 h at 1400 °C under a load of 493 MPa, which is remarkable for a material at 0.74 T_m. Based on the charge balance requirement, Clegg *et al* have identified two higher melting point systems of a similar nature to mullite, which are $2Y_2O_3.GeO_2$ and $2Sm_2O_3.ZrO_2$ and have melting points of > 2000 and 2190 °C respectively.

1.2.4.2 SiC - SiC

As noted above, SiC has limited potential in monolithic form as a high-temperature material due to its brittleness. When reinforced with SiC fibres, the toughness and elongation can be improved, though the reinforcing fibres require coating to avoid coalescence with the matrix [32]. Common coatings are hexagonal boron nitride, pyrolytic carbon (pyC), and SiC - pyC multilayers [32]. For the SiC - pyC - SiC configuration, the fracture strength in tension is 100 MPa at 1100 °C at a ductility of 0.3 %. This strength level is somewhat below that quoted in section 1.2.3.1 (which may be a figure for compression loading or a converted hardness value).

1.2.5 Carbon-Carbon Composites

Carbon is not oxidation resistant, even at low temperatures, and therefore requires protection either by alloying or coating. In some applications it may be used uncoated if the planned life is short, and if severe material losses are accounted for in the design. Its toughness may be improved by incorporation of a woven carbon fibre matrix, and possible oxidation resistant coating materials [32-34] for this configuration include stable intermetallics, such as Pt_3Zr. It has been reported that this material has been used in a demonstrator gas turbine, where the short-term operating temperature was 2000 °C [33].

1.3 Nickel-Base Superalloys – Design and Behaviour

The Ni-base superalloys (NBSAs) are perhaps the most notable metallurgical achievement of the 20th century. These alloys first appeared early in the century [35], in the form of the alloy Ni - 20 wt%Cr (Nicrome). With Whittle's invention of the gas turbine came a need for better materials, able to withstand extreme conditions for long periods under load. As seen above in section 1.1, the efficiency and output of a turbine both increase with increasing turbine entry temperature, and so development of the engine has driven development of the NBSAs since the main limit to the TET was the temperature capability of the materials from which the turbine was built.

These alloys all have one common feature - they are predominantly two-phase, based on Ni, with a matrix phase based on Ni solid solution (γ) and a precipitate phase based on the intermetallic $Ni_3(Al,Ti)$ (γ') [35]. Other phases may be present, some unintentionally, and the microstructures obtained vary widely, depending on composition and processing.

The first NBSAs were wrought alloys, and hence needed to have hot strength low enough to ensure successful hot forging. Advances in casting and solidification [36] technology led to directionally-solidified components, first yielding components with only longitudinal grain boundaries, then single-crystal components. With these advances came

compositional modification which improved the high-temperature strength significantly. Modern alloys contain as much as 6 %Re [36], and with complex internal cooling architecture as well as the use of coatings, these alloys can operate with metal temperatures approaching 1150 °C.

Modern single-crystal alloys employ a cuboidal γ' morphology [35]. This morphology is a result of alloy misfit at the heat treatment temperature, the crystal structures, and elastic compliance differences between the matrix and the precipitate. Whilst room-temperature misfit is approximately 0.2 - 0.5 % (precipitate lattice parameter > matrix lattice parameter), the misfit is close to zero or slightly negative at the service temperature due to thermal expansion differences between the phases [35].

Recent research at NIMS in Tsukuba, Japan, has indicated that still further improvement in possible, as shown in figure 1.6 [37]. This shows that the TMS series of alloys, in particular TMS-64, are purportedly superior in high-temperature performance to other alloys [38]. Recent compositions (TMS-75, TMS-82+) are undergoing in-service testing, and are expected to afford significant advantages over third generation alloys in terms of mechanical properties and/or cost [38]. A proportion of the current research effort is aimed at reducing the cost of alloys without sacrificing mechanical behaviour, corrosion and oxidation resistance and density.

At least three current NBSA research programs are investigating the influence of PGM additions to NBSAs [39-41]. Research in General Electric Corporation in the US has identified Ru as the element of choice in their alloys [39], and this seems to be the conclusion likely to be reached by the program at NIMS [40]. Alloy compositions in the program at the University of Cambridge [41] differ somewhat to those above, so whether the same conclusion will be reached is uncertain.

A prior program to the three mentioned in the above paragraph, investigating addition of PGMs to polycrystalline NBSAs [42-44], showed that Pt additions improved sulfidation and cyclic oxidation performance without affecting their mechanical properties. The

timing of this work was unfortunate as second-generation single-crystal alloys (containing small amounts of Re) appeared at about the same time, and the service life extension benefit of Pt was not sufficient to fit in with maintenance cycles [45]. The alloys were not investigated further.

The microstructural trends over the period described above have been towards higher γ' volume fractions and a change from spherical to cuboidal precipitates [35]. In addition, heat treatments consisting of several steps have been used to give a bimodal size distribution of γ', termed coarse (500 nm - 1 μm) and hyperfine (50 nm). A microstructure typical of modern superalloys is shown in figure 1.7.

1.3.1 Constituent Elements of NBSAs

Superalloys may contain as many as 16 elements [35]. These will partition to γ (e.g. W, Co, Cr, Mo, Re), γ' (e.g. Al, Ti, Nb and Ti) or the grain boundaries (B, C, Mg, Zr, Hf). The move towards single crystal alloys has simplified the alloy composition as grain boundary modifiers are not required. The effect of these additions may be classed as follows [35]:

1. melting point promoters;
2. γ solid-solution strengtheners;
3. γ stabilisers/promoters;
4. γ' formers; and
5. γ' modifiers.

In addition to the above classes, several other secondary effects exist. Addition of certain elements allows more of another to be added without destabilising the microstructure. The balance of elements partitioning to the γ and γ' phases must be considered so as to keep the service-temperature misfit close to zero, and certainly not outside a narrow range either side of this. The reason for this will be discussed later in this section.

The alloy composition must also take into account the potential for formation of topologically close-packed phases (TCPs), which are a critical issue for all modern alloys [35]. These phases are thermodynamically stable over intermediate temperature ranges. Whilst these TCPs may facilitate nucleation and transmission of cracks, their main deleterious effect is to capture the refractory metals and other potent solid-solution strengtheners from the alloy, leading to a surrounding zone denuded of these elements, hence resulting in a localised degradation of the mechanical properties.

1.3.2 γ Solid-Solution Strengtheners - Strengthening Mechanisms

Several mechanisms have been proposed to explain the observed strengthening of γ by alloying [35]. The elements partitioning to γ have a size difference from Ni of 1 – 13 %, and an electron hole number difference of 1 - 7 %. The electron hole number is defined as the number of empty orbitals in the d-shell.

Mott and Nabarro proposed that a hardening mechanism in dilute binary solid solutions was local lattice distortion due to atomic over/undersize [35]. Their model fitted dilute binary Ni solutions, and described the change in yield stress upon alloying as being proportional to the atomic modulus, atomic mismatch and concentration of solute.

Fleischer believed the strength increase due to alloying is also partly due to the local increase in elastic modulus of the lattice [35]. More work is required to force a dislocation through a 'hard' region than a 'soft' region.

Polloux and Grant observed a secondary effect. For fixed lattice strains, they showed the change in yield stress to be proportional to the change in electron hole number [35].

Beeston showed that the yield stress increased with decreasing stacking fault energy [35]. This may be explained by the formation of partial dislocation pairs bounding a stacking fault within the alloy. These partial dislocations are sessile and result in pinning of

portions of the dislocation, leading to the requirement of dislocation bowing for further dislocation motion which only occurs under increased stress.

1.3.3 Interfacial Strengthening in NBSAs

The γ/γ' interface is very important in superalloys, as it determines factors such as precipitate shape, size and stability [35]. Fine precipitates give the largest area of interface and increase the yield strength, though larger precipitates are more beneficial to creep resistance. The practical limit to the γ' volume fraction is approximately 70 %, as above this level the precipitates coalesce and the creep resistance diminishes. The coarsening of γ' is a function of the interfacial energy. At zero misfit the γ/γ' interfacial energy is very low as the coherence strain is minimised, and the precipitate is hence quite stable. The main effect of Re in modern alloys is to reduce the coarsening rate by approximately 30 % [35]. This is because the diffusion of Re in Ni is extremely slow. Solubility of Re in γ' is very low, so the rate-limiting step for γ' coarsening hence becomes the diffusion of Re away from the moving γ/γ' interface.

The strengthening effect conveyed by γ' precipitation in γ is dependent on a number of factors. These are [35]:

1. volume fraction of γ';
2. γ' particle size;
3. solid solution strengthening of constituent phases; and
4. presence of hyperfine γ'.

The γ / γ' interface brings more mechanisms into play, such as the following that have all been proposed [35]:

1. coherency strains;
2. matrix/precipitate elastic modulus differences;
3. precipitate ordering;

4. stacking fault energy differences between γ and γ';
5. energy of creating additional particle / matrix interfacial area; and
6. increase of 'lattice resistance' of particles with temperature.

Whilst many models have been proposed to describe the above effects, the above effects can all be considered to contribute to the yield strength and creep performance of the superalloys. When the misfit is zero, there is no coherency strain, and the volume fraction of γ' is the most significant variable [35].

The effect of the volume fraction of γ' and test temperature on the flow stress of a simple ternary alloy (Ni – Al - Cr) is shown in figure 1.8, which demonstrates very well the dependence of yield strength at low temperature on the interfacial strength [35]. At high temperature, it can be seen that the yield strength increases continuously with increasing volume fraction of γ'. This is due to the load transferral to the γ' at high temperature [35]. The peak is at a surprisingly low fraction of γ' at room temperature.

The misfit and volume fraction of γ' affects creep rupture life significantly [35]. This is shown in figures 1.9 and 1.10. The peak is at zero misfit, which is due to the ability to maintain hyperfine γ' precipitates without coalescence [35].

Some modern alloys exhibit "rafting" at intermediate temperatures under stress [46]. Those that have a slightly negative misfit raft perpendicular to the applied stress. The effect of the rafting is to increase the distance dislocations must climb to bypass the larger obstacle, hence lowering creep strain and improving creep life for a given set of conditions.

Whilst significant improvements have been made over the past 60 years, the temperature capability of these alloys are approaching an asymptote. Current-generation alloys have solidus temperatures in the region of 1360 °C, and bulk material temperatures in the most critical components are greater than 0.85 T_m. Further material developments are likely to be quite limited, since the law of diminishing returns applies - the cost of the alloy

development program is the same as for the previous alloys, but the temperature advantage realised by each subsequent research effort is constantly reducing.

1.4 High-Strength PGM alloys

1.4.1 The Pure Metals

The room-temperature mechanical and physical properties of the pure PGMs are given in table 1.1 [47]. Due to the extreme difficulties in handling Os, no successful tensile tests have been performed, and as a result only its elastic modulus is known. The range of ductility given for Ir is very broad, as it is a very impurity-sensitive material. The general impression amongst metallurgists for several decades has been that Ir is inherently brittle, and that grain boundary impurities are the cause [48-49]. Doping Ir with Th has alleviated the brittleness to a degree [50], and single crystals of Ir have been shown to be quite plastic [51]. A recent ab-initio study [52], however, has indicated that the bonding in Ir takes on a "pseudocovalent" component under shear deformation, leading to an unusually large value for its shear modulus that is the ultimate cause of its brittleness. From the table it is also evident that the recrystallisation temperatures of the four f.c.c. PGMs scale with their melting points, and are all about 0.4 T_m with the exception of Ir (0.58 T_m) [53].

The creep performance of the four f.c.c. PGMs in a vacuum again scales with the melting point (see figure 1.11) [53]. In oxidising atmospheres such as air, Ir suffers catastrophic oxidation that significantly affects its creep performance [54]. Coating the Ir with a 100 μm Pt sheath has been shown to alleviate the problem, such that an Ir sample withstood 53 MPa for 100 h at 1250 °C [55]. This is in contrast to 100 MPa for 160 h at the same temperature under vacuum [55]. Rhodium can withstand stress an order of magnitude greater than Pd, and Pd is generally poorer than Pt, with the exception of low stress values at 1300 °C [53]. This general relation is again in keeping with the melting points of these elements.

Of the six PGMs, the best oxidation performance is exhibited by Pt and Rh [56]. All the metals form oxides that volatilise - RhO_2 at 1400 °C, IrO_2 at 1120 °C, PtO_2 at 280 °C - 450 °C, PdO_2 at 870 °C, RuO_2 at 1540 °C and OsO_2 at 650 °C [56]. Above the dissociation temperature the metals lose weight continuously, the rate of which is dictated by the air flow rate the and equilibrium partial pressure of the oxide [56]. The mass loss rate as a function of temperature is given in figure 1.12 for all PGMs [56]. The effect of higher flowrates is to increase the mass loss rate, as shown in figure 1.13.

Table 1.1 Some physical and mechanical properties of the PGMs at 20 °C [47,53]

Element	**Ru**	**Rh**	**Pd**	**Os**	**Ir**	**Pt**
Atomic Number	44	45	46	76	77	78
Crystal Structure	h.c.p.	f.c.c.	f.c.c.	h.c.p.	f.c.c.	f.c.c.
Melting Point (°C)	2310	1963	1552	2700	2447	1769
Density (g/cm^3)	12.45	12.41	12.02	22.61	22.65	21.45
Tensile Strength, Annealed (MPa)	500	690	170	†	1100	125
Modulus of Elasticity in Tension (GPa)	420	316	120	560	520	170
Hardness, Annealed (HV)	200-350	100-102	40-42	300-670	200-240	40-42
Lattice Parameters: a	2.7056	3.8029	3.8906	2.7340	3.8392	3.9229
c	4.2816			4.3194		

† Not available

1.4.2 PGM Alloys

1.4.2.1 Single-Phase Alloys

Of the PGMs, the metallurgy of the four cubic metals has been studied more than that of the hexagonal metals. The effect of binary additions to each cubic metal has been extensively studied, and a general rule is that the PGMs all strengthen one another to

varying degrees at room temperature [56]. This is probably due to the size difference between the matrix and solute atoms.

The effect of small additions of solute elements on the proof stress of Pt is shown in figure 1.14. From this it can be seen that the most potent strengtheners at room temperature are Ni, other PGMs and W [56].

The most widely-used single-phase PGM alloys in high-temperature applications are the Pt-Rh alloys [59]. These are used due to the strengthening effect of Rh in Pt, as well as their extremely good environmental resistance. Such alloys find application in thermocouples, furnace windings, glass processing, and as catalyst gauzes for high-temperature chemical processing.

Due to its high melting point and possibly also its unique bonding (see above), Ir is a good strengthener of Pt, and is used in alloys for service at temperatures where pure Pt is too soft [60]. The increase in creep life obtained by Ir addition is significant, though any use in an oxidising atmosphere will degrade this benefit. In these two-component alloys, the element with poorer oxidation resistance (Ir in this case) will selectively oxidise and cause surface cavitation, which is detrimental to the strength in a loaded component [60].

1.4.2.2 Oxide Dispersion-Strengthened Alloys

The high-temperature melting points of single-phase alloys can be greatly improved by the inclusion of a finely-dispersed refractory oxide [61]. The purpose of the oxide is to pin grain boundaries, such that the normal grain-boundary sliding process that dominates high-temperature creep of single-phase polycrystalline alloys is greatly reduced.

Oxide Dispersion-Strengthened (ODS) alloys were first produced in the 1950s [35], with early superalloys utilising this strengthening mechanism (before the advent of directional solidification and single-crystal casting). It was subsequently used in Pt alloys for the

glass industry [62,63], as well as other high-temperature alloys such as PM2000 (an ODS FeCrAlY alloy) [64].

1.4.2.3 Multiphase Alloys

The area of PGM-based fcc-$L1_2$ alloys was pioneered by Harada and co-workers [65-67] at NRIM (now NIMS) in Tsukuba, Japan (see below), using Ir and Rh as the base for a range of new alloys. The proof stresses of these alloys (see figure 1.15) were extremely high over a wide temperature range, an example being the alloy Ir - 16 at%Nb that had a proof stress of 200 MPa at 1800 °C [65]. Subsequent work has focussed on using ternary and higher additions to improve strength, modify the microstructure, reduce cost and decrease density [68-73].

In a parallel and collaborative program of work to that described within this dissertation, Patricia Hill and co-workers [74-76] at Mintek in South Africa investigated the phase equilibria, mechanical properties and oxidation behaviour of several Pt-based systems. The aim of Hill's work was to produce a superalloy analogue based on Pt which offered a 200 °C temperature advantage over PM2000, an ODS Fe-based alloy considered to possess excellent high-temperature mechanical and oxidation properties [77].

The PhD dissertation of Hill [77] describes a three-stage investigation into Pt-based f.c.c.- $L1_2$ alloys, with a view towards development of a superalloy analogue.

The first stage consisted of identifying ternary systems in which a f.c.c.-$L1_2$ two-phase field existed, and performing (preliminary) screening tests on these alloys to examine the oxidation behaviour, hardness and deformation behaviour. The ternary systems were chosen to consist of a precipitate forming element (specifically Ti, Ta, Al and Nb) and a solid-solution strengthening element (Ni, Re and Ru).

The oxidation tests performed at this stage were stepped tests up to 1400 °C, while the deformation behaviour and mechanical properties could be qualitatively examined in a

rudimentary fashion by hardness testing. Cracking at the corners of the indent indicates brittleness; straight slip steps in the regions near the indentation indicate limited plasticity, whilst wavy slip steps and wavy indent edges indicate strain accommodation by a large number of slip systems. On the basis of the above tests it was determined that Al was essential for high-temperature oxidation resistance whilst suppression of the low-temperature form of Pt_3Al was desirable.

The second phase of work concentrated on characterisation of Pt - Al - Z systems (Z = Mo, V, Ta, W, Re, Cr, Ti, Ni and Ru) systems, in terms of mechanical properties, microstructure and oxidation behaviour. On the basis of these tests the systems Pt - Al - Cr, Pt - Al - Ru and Pt - Al - Ti were recommended for further study, as the chosen elements promoted a favourable microstructure, imparted good solid solution strength to the (Pt) matrix and did not affect the oxidation resistance imparted by the Al. Whilst Re was also examined, and was known to be a potent solid-solution strengthener of Pt, its presence degraded the oxidation resistance more than was acceptable, and little benefit was gained by adding smaller amounts that did not adversely affect the alloy. The addition of Ta, unsurprisingly, had a similar effect to Re, though as it was less severe up to 3 at% was thought to be acceptable.

Since submission of her PhD, Hill has published a paper [78] describing initial results of the third phase of work. In this paper the creep behaviour of Pt - Al - Cr alloys are examined, and one has been found to offer some temperature advantage over single-phase (Pt) alloys (see figure 1.16). The proof stresses of some of the alloys discussed above are given in figure 1.17 as a function of temperature. These alloys will be discussed again in chapter 4, when they are compared to the alloys produced in the current work.

It should be noted that the Pt-Al system has a eutectic reaction between pure Pt and Pt_3Al, and that the latter phase melts congruently at the relatively low temperature of 1556 °C whilst the eutectic temperature is 1507 °C [79]. Hill's alloys experienced the onset of melting at temperatures in the range 1556 °C - 1582 °C [72]. From the standpoint of developing an alloy for use at temperatures in the range 1300 °C - 1350 °C, this presents a

problem as the mechanical properties of an alloy will degenerate as the melting temperature is approached. In the case of third-generation NBSAs, the maximum operating temperature is approximately 1150 °C, with a solidus temperature of approximately 1370 °C [37]. This maximum operating temperature is due to the rapid dissolution of the precipitate phase combined with softening of the precipitate phase γ' leading to loss of strength and creep resistance at temperatures above 1150 °C. A similar restriction on Hill's alloys, based on the solidus temperatures above, would limit their maximum operating temperatures to approximately 1350 °C, which just satisfies their temperature capability objective.

To achieve a higher temperature capability, alloy additions need to be made such that the liquidus temperature is raised. This might be achieved by adding high melting-point elements, or by elements which raise the solidus of pure Pt. Another option may be to attempt to raise the melting point of the Pt_3Al phase through substitution of Al by higher melting point $L1_2$ formers.

The requirement of the presence of Al for oxidation resistance makes such modification relatively difficult, as forcing it from the precipitate to the matrix leads to a loss in melting point of the matrix (evident from the Pt - Al diagram) [79]. The amount of Al required for effective oxidation resistance will depend on the concentration of other alloying elements, but within binary Pt-Al alloys there will be a minimum required Al content for continuous scale formation. This has been determined by Nanko, Ozawa and Maruyama [80] to be 7.6 at%Al, which agrees with the observations of Felten and Petit [81], who found that an alloy containing 4 at%Al formed a non-continuous scale, whereas an alloy containing 17 at%Al formed a protective, adherent, continuous layer of Al_2O_3.

The most effective way of producing an alloy based on Pt but employing an alumina scale may be to find a precipitate with a very high melting point, and with a high solubility for Al (and where the Al segregates preferentially to this phase). In this way the melting point of the matrix phase would be relatively high, whilst the alloy would contain sufficient Al to effect oxidation protection. Such a Pt-based $L1_2$ phase may not exist, in which case an

alternative approach would be to improve the melting point of the Pt_3Al or else balance the ratio of Al to melting-point promoters and solid solution strengthening elements such that large Al additions do not depress the MP greatly. The melting point promoters would also need to be gamma stabilisers, such that their addition allows for large amounts of other elements to be added without affecting phase stability.

1.5 Introduction To The Project

1.5.1 Why Choose Platinum As The Base Element For A New Range Of Alloys?

The purpose of this project was to develop a new high-temperature two-phase alloy, analogous to the NBSAs, but based on a platinum-group metal. The platinum group metals consist of periods 5 and 6 of the group VIIIB transition metals (see Table 1.2, below).

Table 1.2 Global production [82] data for the PGMs. The figures for Ru and Ir are world consumption rather than world production due to unavailability of this data. This will be different, not least because of the amount of Ru recycled annually.

Element	2000 Global Production (troy oz.)	2000 average price ($US/Oz.)
Ru	439,000	130
Rh	766,000	1990
Pd	7.79m	690
Os	-	-
Ir	127,000	415
Pt	5.23m	550

The melting points and densities of the lower atomic number PGMs are significantly lower than those of the higher atomic number PGMs. Of these elements, osmium has by far the highest melting point, but has a hexagonal crystal structure and suffers from catastrophic

oxidation in air at elevated temperature. Ruthenium also has a hexagonal crystal structure and has relatively poor oxidation resistance, but can operate at elevated temperatures if alloyed with elements such as Al to provide a protective oxide. As the project requires a base metal with a cubic crystal structure (to produce a NBSA analogue), the above two elements could be eliminated from consideration.

The remaining four elements have cubic crystal structures. Of these four, the melting point of Pd is too low for consideration as a base, since it only offers a potential temperature advantage of about 100 °C over Ni (melting point: 1453 °C).

One reason for choosing Pt as the base element of the work described in this thesis was due to the NRIM investigations into Ir and Rh as base elements, which are described above. Another consideration was the market economics of the PGMs. The PGMs are produced in relatively small quantities, as seen in table 1.2. Of these, the global production of Rh and Ir are on the order of one-tenth that of Pt and Pd. Their prices are consequently severely affected by differences between production and demand, as was seen in recent years for the Rh and Pd prices (in particular) which increased substantially, and also Pt and Ir to a lesser extent [82].

The demand for Pd and Rh in recent years (mostly from the automotive industry) coupled with decreasing Russian production has seen their prices rise from $130 /oz and $308 /oz respectively in 1996 to $980 /oz and $2000 /oz respectively in 2000 [82]. As Russian deposits are Pd-rich whereas South African deposits are Pt-rich, the falling Russian production will affect the Pd price more than the Pt price. In the case of Rh, its production as a by-product of Pt and Pd mining is one reason for this price increase – that is, it cannot be mined for itself, but relies on mining of Pt and Pd for its production, implying that its production cannot be increased to meet demand without an associated increase in platinum and palladium production.

The Pt price has risen since its 1996 - 1999 plateau of approximately $390 /oz to $550 /oz in 2000 [77]. This is due to the lack of export by Russia and increased demand for its substitution for the more expensive palladium in catalyst applications [82].

From the above discussion it is apparent that the Rh price fluctuates over a wide range due to its low availability, whereas that of Pt is much more stable. The implication of this is that any new application for Pt requiring large amounts (upwards of 50,000 oz p.a.) would not have a significant effect on the price, whereas the same is not true of Rh and Ir. This leads to the conclusion that the most suitable PGM upon which a new high-temperature alloy should be based is Pt.

It should be noted that a further advantage of the PGMs is their recyclability. As the market price of these metals is so high (Pt is approximately $US 16000 /kg) then the recycling costs (at ca. $US 1000 /kg) make scrap recovery extremely financially attractive [83]. The production figures quoted in table 1.2 are for "new" platinum, or that which is mined each year. Recycled PGM figures are difficult to find, though it is likely that the amount of recycled PGM reaching the market each year is at least equivalent to the amount of new PGM.

1.5.2 Pt-Based f.c.c. - $L1_2$ Two-Phase Systems

Several Pt-based two-phase f.c.c. – $L1_2$ systems have been identified during the course of phase equilibria studies. As a result of the work focus being phase equilibria, no mechanical properties have been reported for such alloys [79].

As discussed above in section 1.3, the mechanical properties of single-phase Pt-based f.c.c. alloys are well understood. In a series of publications beginning in 1979, Suzuki and co-workers [84-86] investigated the mechanical properties of Pt-based $L1_2$ phases, from a standpoint of examining the yield stress anomaly in Ni_3Al and other $L1_2$ phases. Their work showed the potential of the Pt-based $L1_2$ phases as high-temperature structural materials, as their proof stress and hardness was above that of Ni_3Al at elevated

temperatures [84-86]. Not all Pt-based phases exhibited the yield stress anomaly – some had a plateau whereas others softened continuously with increasing temperature. These data are plotted in figure 1.18(a) in absolute terms, and in 1.18(b) as specific yield stress versus homologous temperature, T/T_m. From these figures it is apparent that Ni_3Al is unique in terms of its specific strength - that of Ni_3Al is at least double any of the Pt compounds. In terms of the homologous temperature at which the peak occurs, Ni_3Al is not unique - the peaks of Pt_3Cr, Pt_3Al, Pt_3Ga and Pt_3In are at similar temperatures.

Of particular interest are the proof stresses of Pt_3Al and Pt_4Hf [84-86]. The stoichiometry of the latter is not that which is usually associated with $L1_2$ alloys, which possess a 3:1 stoichiometry in ideal cases. As will be discussed later in this thesis, there is a class of intermetallics in which stoichiometry is affected by substitution of one constituent element for the other such that occupation of one or more lattice sites may be mixed.

1.5.3 Overview of Thesis

This thesis contains three experimental chapters. These describe the investigations into binary and ternary phase equilibria of some Pt-based systems, the selection of alloys for further testing and the mechanical properties of two alloys.

In chapter 2, the binary phase equilibria of the Pt - Zr and Pt - Hf systems are described. These elements were chosen due to the possibility of producing a superalloy analogue in these binary systems, as well as the lack of binary phase equilibrium data for these systems. In the Pt - Hf system, one intermetallic compound (Pt_8Hf) has been observed for the first time, and the existence of one other (γ', based on the stoichiometry Pt_4Hf) confirmed. This has allowed the Pt-rich end of the Pt - Hf binary phase equilibrium diagram to be drawn for the first time. In the Pt - Zr system, the existence of Pt_8Zr and the $L1_2$ phase γ' (again, close to Pt_4Zr stoichiometry) have been confirmed, allowing for modification of the existing Pt - Zr binary phase equilibrium diagram.

In chapter 3, investigations into the ternary phase equilibria of the systems Pt - Rh - Zr, Pt - Rh - Hf and Pt - Ti - Cr are described in order to establish composition ranges in which superalloy analogues may be produced. It will be shown that substantial two-phase (Pt)-γ' fields exist in the first two systems, whereas in the third a narrow two-phase field exists. In the latter system, it will also be shown that the Pt_3Cr and Pt_3Ti phase fields may be connected.

Chapter 4 describes the microstructure and properties of two alloys, one a Pt - Rh - Hf alloy and the other a Pt - Ti - Cr alloy. The compositions of these alloys were chosen to consist of approximately 50% $L1_2$ phase, and a two-step heat treatment was employed to produce coarse and fine precipitates. It will be shown that the Pt - Rh - Hf alloy possesses the highest known proof stress of any Pt alloy at temperatures above 1000°C, and exhibits very promising creep strength. It will also be shown that the proof stress of the Pt - Ti - Cr alloy is relatively poor in comparison.

Chapter 5 summarises the main conclusions of the thesis, as well as describing opportunities for further work.

1.6 References

1. J. Bannister, WWW: http://www.generali.com/library/airline/business.html#chart1

2. S. Friedrichs, PhD Thesis, Department of Engineering, University of Cambridge (1997)

3. C. T. Sims, Proc. Superalloys 1988, Eds. S. Reichman, D. N. Duhl, G. Maurer, S. Antonovich and C. Lund, The Metallurgical Society (1988) pp 173-182

4. J. R. Stephens and M. V. Nathal, Proc. Superalloys 1988, Eds. S. Reichman, D. N. Duhl, G. Maurer, S. Antonovich and C. Lund, The Metallurgical Society (1988) pp 183-192

5. M. V. Nathal and S. R. Levine, Proc. Superalloys 1992, Eds. S. D. Antonovich, R. W. Stusrud, R. A. MacKay, D. L. Anton, T. Khan, R. D. Kissinger and D. L. Klarstrom, The Minerals, Metals and Materials Society (1992) pp 329-340

6. ASM Handbook, 10^{th} Edition, Volume 2, ASM International, Warrendale, 1990

7. M. D. Alvey and P. M. George, Carbon, **29** 523-530 (1991)

8. L Schoenman, Journal of Propulsion and Power, **Vol 11** No 6 Nov-Dec 1261 – 1267 (1995)

9. M. R. Jackson, B. P. Bewlay, R. G. Rowe, D. W. Skelly and H. A. Lipsitt, JOM **7** (1) 39-44 (1996)

10. P. R. Subramanian, M. G. Mendiratta and D. M. Dimiduk, JOM **7** (1) 33-38 (1996)

11. P. R. Subramanian, M. G. Mendiratta, D. M. Dimiduk and M. A. Stucke, Mat Sci Eng A, **239-240** 1-13 (1997)

12. S. J. Balsone, B. P. Bewlay, M. R. Jackson, P. R. Subramanian, J.-C. Zhao, A. Chatterjee and T. M. Hefferman, Paper presented at International Symposium on Structural Intermetallics, Jackson Hole, Wyoming, Sept. 2001

13. J. Sha, H. Hirai, T. Tabaru, A. Kitahara, H. Ueno and S. Hanada, Mat Trans JIM **41** 1125-1128 (2000)

14. C. L. Ma, A. Kasama, H. Tanaka, Y. Tan, R. Tanaka, Y. Mishima and S. Hanada, Mat Trans JIM **41** 444-451 (2000)

15. D. L. Anton, "Ni3Al in Nickel-Based Superalloys", in Intermetallic Compounds - Principles and Practice, Vol. 2, eds. J. H. Westbrook and R. L. Fleischer, John Wiley and Sons, Chichester (1995) pp 3-16

16. D. B. Miracle and R. Darolia, "NiAl and its Alloys", in Intermetallic Compounds - Principles and Practice, Vol. 2, eds. J. H. Westbrook and R. L. Fleischer, John Wiley and Sons, Chichester (1995) pp 53-72

17. M. L. Easley and J. R. Smyth, Proc. Superalloys 1996, Eds. R. D. Kissinger, D. J. Deye, D. L. Anton, A. D. Cetel, M. V. Nathal, T. M. Pollock and D. A. Woodford, The Minerals, Metals and Materials Society (1996) pp 571-578

18. R. L. Fleischer, R. D. Field and C. L. Briant, Met Trans A, **22A** 403-414 (1991)

19. R. F. Fleischer, Platinum Metals Review, **36** 138-145 (1992)

20. R. L. Fleischer, Met Trans A, **24A** 227-230 (1993)

21. R. L. Fleischer and D. W. McKee, Met Trans A **24A** 759-763 (1993)

22. I. M. Wolff and G. Sauthoff, Met. Mat. Trans., 1996, **27A** 1395-1400 (May)

23. I. M. Wolff and G. Sauthoff, Met Mat Trans A, **264** 2642-2652 (1996)

24. I. M. Wolff and G. Sauthoff, Acta Mater. **45** 2949-2969 (1997)

25. I. M. Wolff, G. Sauthoff, L. A. Cornish, H. DeV. Steyn, and R. Coetzee, Proc. Structural Intermetallics 1997, Eds. M. V. Nathal, R. Darolia, C. T. Liu, P. L. Martin, D. B. Miracle, R. Wagner, and M. Yamaguchi, The Minerals, Metals and Materials Society, Warrendale (1997) pp. 815-823

26. K. N. Lee and W. L. Worrell, Oxidation of Metals, **32** 357-369 (1989)

27. K. N. Lee and W. L. Worrell, Oxidation of Metals, **41** 37-63 (1994)

28. H. E. Helms, L. C. Lindgre, P. W. Heitman and S. R. Thrasher, Ceramic Applications in Turbine Engines, Noyes Publications, Park Ridge, New Jersey (1986)

29. R. Darolia, W. S. Walton and M. V. Nathal, Proc. Superalloys 1996, Eds. R. D. Kissinger, D. J. Deye, D. L. Anton, A. D. Cetel, M. V. Nathal, T. M. Pollock and D. A. Woodford, The Minerals, Metals and Materials Society (1996) pp 561-570

30. N Hirosaki, T. Nishimura, Y. Yamamoto and Y. Shinoda, Paper presented at the One-day symposium on High Temperature Materials 2000, March 2, 2000, NRIM, Tsukuba, Japan

31. W. J. Clegg, A. Kelly and J. E. Pitchford, Key Engineering Materials, **161-163** 315-320 (1999)

32. R. R. Naslain, Phil. Trans. R. Soc. **351** 485-496 (1995)

33. W. Shields, Jr., JOM **7** 1 (1996)

34. R. F. Fisher, M. D. Alvery and P. M. George, J. Vac. Sci. Technol. A **10** 2253-2260 (1992)

35. N. S. Stoloff, in Superalloys II: High Temperature Materials for Aerospace and Industrial Power, Eds. C. T. Sims, N. S. Stoloff and W. C. Hagel, Wiley Interscience, USA (1987) pp 61-96

36. P. N. Quested and S. Ogersby, Materials Science and Technology, **2** 461 – 475 (1986)

37. H. Harada, Paper presented at the One-day symposium on High Temperature Materials 2000, March 2, 2000, NRIM, Tsukuba Japan

38. T. Yamagata, S. Nakazawa, Y. Koizumi, T. Kobayashi, M. Sato, T. Hino and N. Shibasaki, Paper presented at the One-day symposium on High Temperature Materials 2000, March 2, 2000, NRIM, Tsukuba Japan

39. C. M. Austin, R. Darolia, K. S. O'Hara and E. W. Ross, US patent number 5151249 (1992)

40. Y. Koizumi, T. Kobayashi, T. Yokokawa and H. Harada, Paper presented at High Temperature Materials 2001, May-June 2001, NIMS, Tsukuba, Japan (to be published in Materials Science and Engineering A)

41. A. P. Ofori and C. J. Humphreys, paper presented at Microscopy and Microanalysis 2001, Long Beach, California, August 2001

42. C. W. Corti, D. R. Coupland and G. L. Selman, Platinum Metals Review **24** 2-11 (1980)

43. D. R. Coupland, C. W. Hall and I. R. McGill, Platinum Metals Review **26** 146-157 (1982)

44. T. J. Hurd, PhD Thesis, University of Liverpool, 1985

45. N. Jones, Rolls-Royce plc, Pers. Comm.

46. R. C. Reed, N. Matan, D. C. Cox, M. A. Rist, and C. M. F. Rae, Acta Materialia, **47** 3367-3381 (1999)

47. Platinum Metals Review, **2** 61 (1957)

48. P. Panfilov, A. Yermakov and G. Baturin, J. Mat Sci Lett **9** 1162-1164 (1990)

49. P. Panfilov, V. Novgorodov and A. Yermakov, J. Mat Sci Lett **13** 137-141 (1994)

50. C. T. Liu, H. Inouye and A. C. Schaffhauser, Metallurgucal Transactions A, **12A** 993-1002 (1981)

51. E. M. Savitskii, V. P. Polyakova and N. B. Gorina, Platinum Metals Review **23** 7-13 (1968)

52. Y. N. Gornostyrev, M. I. Katsnelson, N. I. Medvedeva, O. N. Mryasov, A. J. Freeman and A. V. Trefilov, Phys. Rev. B, **62** no 12 7802-7808 (2000)

53. A. S. Darling, International Metallurgical Reviews 91-122 (1973)

54. I. R. McGill, Platinum Metals Review, **21** 85-89 (1977)

55. A. S. Darling, Platinum Metals Rev., **9** 8-19 (1965)

56. J. C. Chaston, Platinum Metals Rev., **9** 51-56 (1965)

57. C. A. Krier and R. I. Jaffee, J. Less-Common Metals **5** 411-431 (1963)

58. G. Schlamp, "Noble Metals and Their Alloys", in "Materials Science and Technology" Vol 8, Eds K. H. Matucha, R. W. Cahn, P. Haasen and E. J. Kramer, VCH Publishers Inc, New York (1996)

59. A. S. Darling, Platinum Metals Review, **5** 58-65 (1961)

60. A. S. Darling, Platinum Metals Review, **4** 18-26 (1960)

61. A. S. Darling, G. L. Selman and A. A. Bourne, Platinum Metals Review, **12** 7-13 (1968)

62. B. Fischer, A. Behrends, D. Freund, D. F. Lupton and J. Merker, Platinum Metals Review **43** 18-28 (1999)

63. Q. Zhang, D. Zhang, S. Jia and W. Shong, Platinum Metals Review **39** 167-171 (1995)

64. C. Capdevilla, Y. L. Chen, N. C. K. Lassen, A. R. Jones and H. K. D. H. Bhadeshia, Mat. Sci. Tech. **17** 693 – 699 (2001)

65. Y. Yamabe, Y. Koizumi, H. Murakami, Y. Ro, T. Maruko and H. Harada, Scripta Materialia, **35** 211-215 (1996)

66. Y. Yamabe-Mitarai, Y. Koizumi, H. Murakami, Y. Ro, T. Maruko and H. Harada, Scripta Materialia, **365** 393-398 (1997)

67. Y. Yamabe-Mitarai, Y. Ro, T. Maruko, T. Yokokawa and H. Harada, Proc. Structural Intermetallics 1997, The Minerals, Metals and Materials Society, Warrendale (1997) pp. 805 - 814

68. Y. Yamabe-Mitarai, Y. Ro, T. Maruko and H. Harada, Scripta Materialia, **40** 109-115 (1999)

69. Y. Yamabe-Mitarai, M.-H. Hong, Y. Ro and H. Harada, Philosophical Magazine Letters **79** 673-682 (1999)

70. Y. Yamabe-Mitarai, S. Nakazawa and H. Harada, Scripta Materialia **43** 1059-1064 (2000)

71. X. H. Yu, Y. Yamabe-Mitarai, T. Yokokawa, M. Osawa, Y. Ro and H. Harada, Proceedings of the International Conference on Iridium, Ed. E. K. Ohriner, R. D. Lanam, P. Panfilov and H. Harada, The Minerals, Metals and Materials Society, Warrendale (2000) pp. 41-48

72. Y. Yamabe-Mitarai, Y. Ro, S. Nakazawa, T. Maruko and H. Harada, Defect and Diffusion Forums, **188-190** 171-184 (2001)

73. Y. Yamabe-Mitarai, Y. Ro and S. Nakazawa, Intermetallics **9** 423-429 (2001)

74. I. M. Wolff and P. J. Hill, Platinum Metals Review, **44** 158-166 (2000)

75. P. J. Hill, Y. Yamabe-Mitarai and I. M. Wolff, Scripta Materialia, **44** 43-48 (2001)

76. P. J. Hill, T. Biggs, P. Ellis, J. Hohls, S. Taylor and I. M. Wolff, Materials Science and Engineering A, **A301** 167-179 (2001)

77. P. J. Hill, PhD Thesis, University of the Witswatersrand (2001)

78. P. J. Hill, G. B Fairbank and L. A. Cornish, JOM **53** No 10 19-20 (2001)

79. Binary Alloy Phase Diagrams, 2nd Edition, Ed. T. B. Massalski, ASM, Materials Park, Ohio (1990)

80. M. Nanki, M. Ozawa and T. Maruyama, Symposium on High-Temperature Corrosion and Materials Chemistry, San Diego, USA, Published by Electrochemical Society Inc. USA 500-511 (1998)

81. J. Felten and F. S. Pettit, Oxidation of Metals, **10** 189-223 (1976)

82. Johnson Matthey plc, Platinum 2000 (2001)

83. D. Coupland, Johnson Matthey plc, Pers. Comm.

84. D.-M. Wee and T. Suzuki, Transactions of the Japan Institute of Metals, **20** 634-646 (1979)

85. D.-M. Wee, O. Noguchi, Y. Oya and T. Suzuki, Transactions of the Japan Institute of Metals, **21** 237-247 (1980)

86. T. Suzuki and Y. Oya, Journal of Materials Science, **16** 2737-2744 (1981)

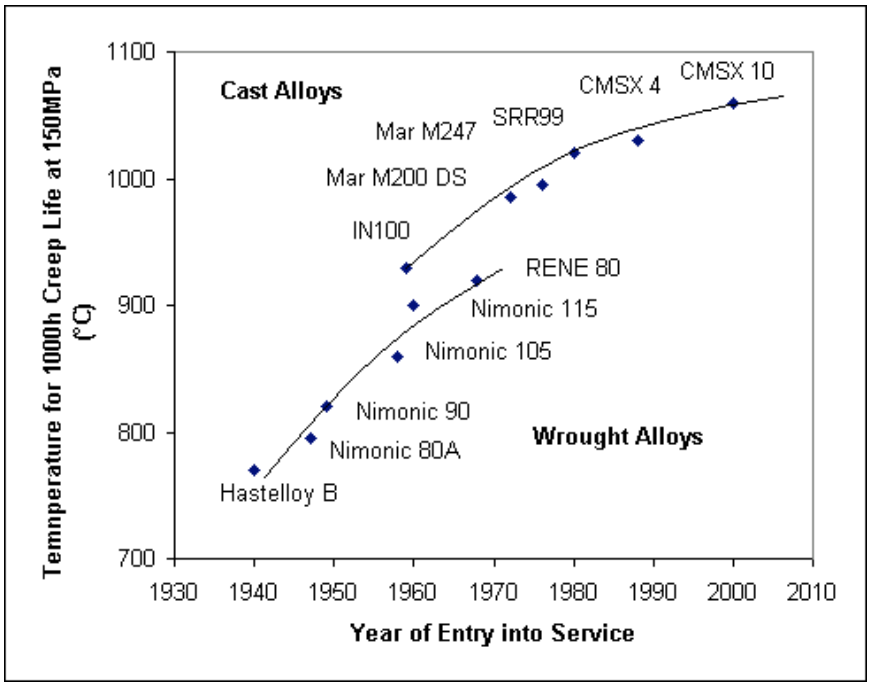

Figure 1.1 The historical increase in Turbine Entry Temperature (TET). The effects of directional solidification and single-crystal casting are evident in the large, sudden jump in the 1960s, and more recently the influence of Re has produced continuing rises. (after Friedrichs [2])

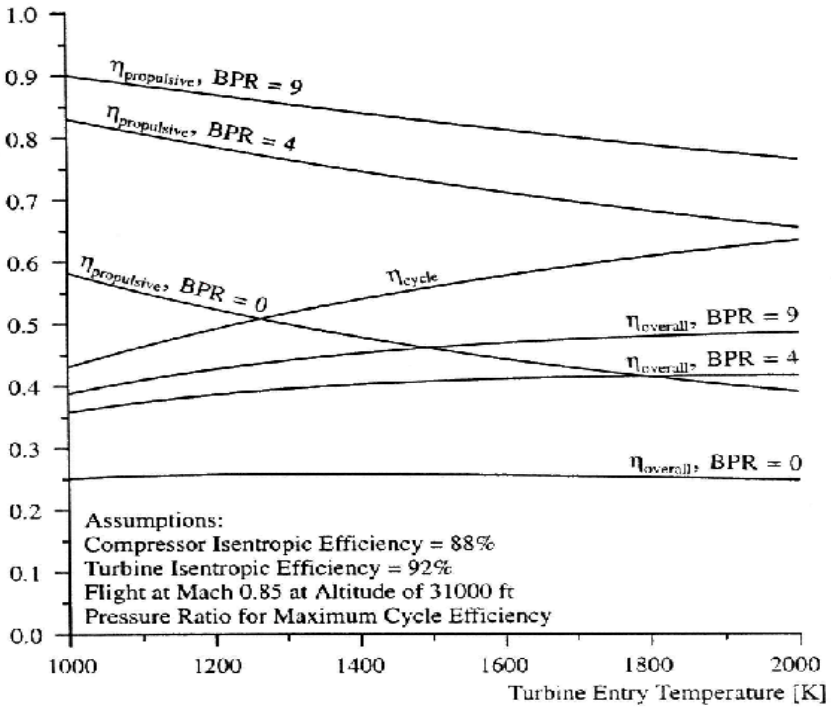

Figure 1.2 The thermodynamic efficiency versus TET. As TET increases above 1600 K, the overall efficiency is essentially constant, which shows that the driving force behind the increase in TET is not for greater efficiency [2].

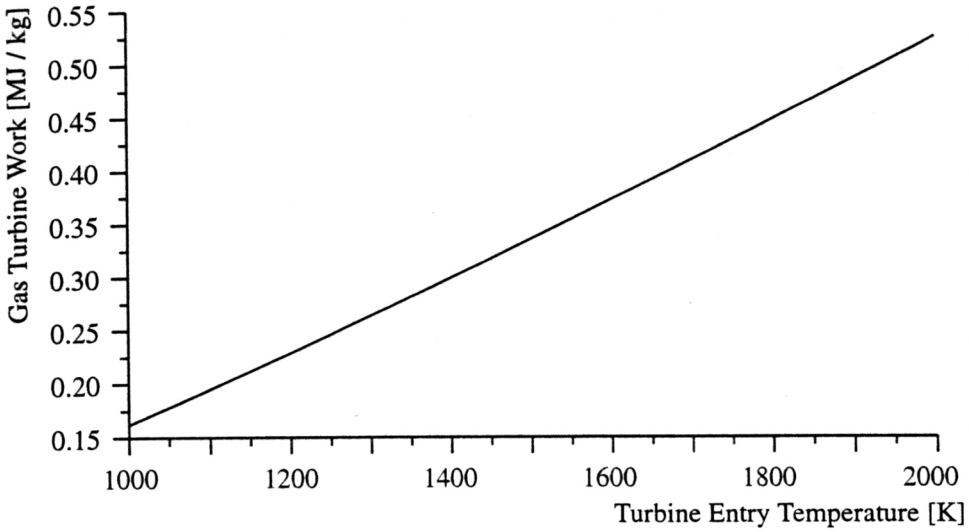

Figure 1.3 The thrust output of the engine plotted as a function of TET. The amount of thrust obtained for a given set of conditions is greatly increased by a rise in TET [2].

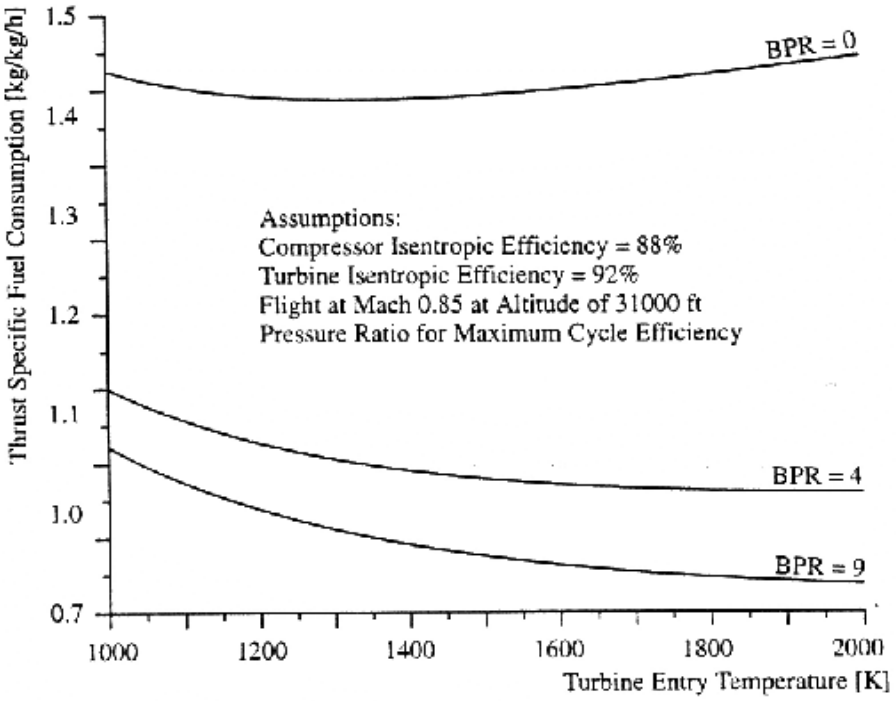

Figure 1.4 The thrust-specific fuel consumption (i.e. the amount of fuel consumed to produce a given level of thrust) is decreased by increasing the TET. This is the reason for the high level of activity in high-temperature material development for gas turbines [2].

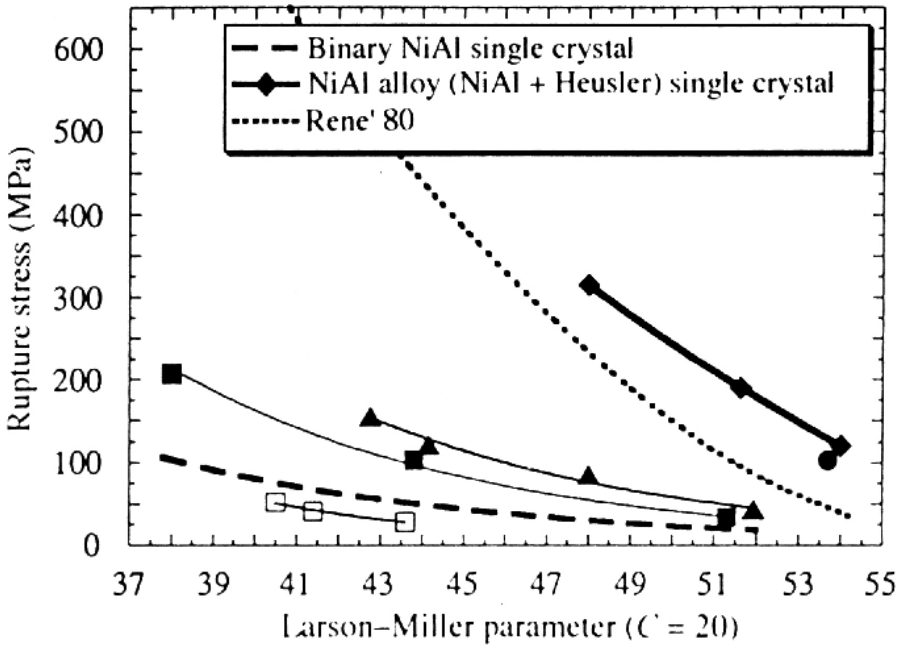

Figure 1.5 The creep behaviour of single-crystal and precipitation-strengthened NiAl compared to Rene 80, a wrought superalloy [16].

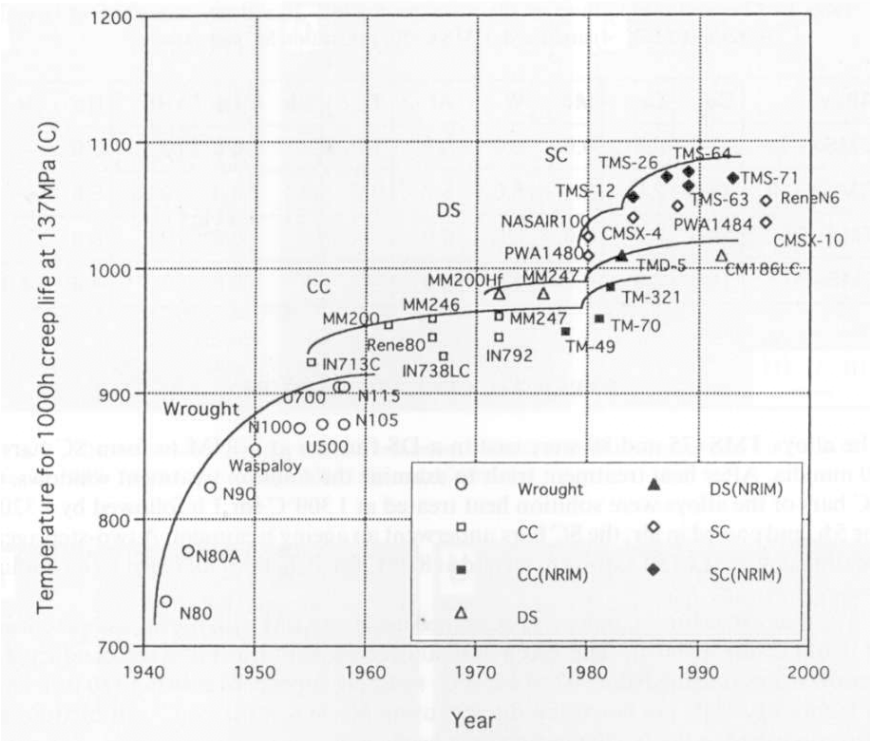

Figure 1.6 The temperature capability history of alloys developed at NRIM / NIMS in Tsukuba, Japan. Their recent alloys appear to offer large temperature benefits over third-generation alloys, and are being termed "fourth-generation" alloys [37].

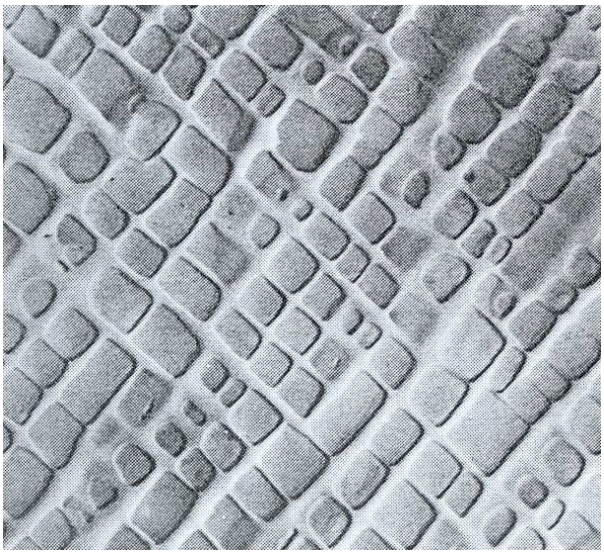

Figure 1.7 A typical microstructure obtained in IN-100, viewed along a {001} zone axis. The cuboidal γ' precipitates occupy approximately 60 % of the volume, and are aligned with cube faces on {001} planes. This is a similar microstructure to more modern alloys, although in (e.g.) CMSX-4 the γ' volume fraction is slightly higher, and due to the two-step heat-treatment used, hyperfine γ' precipitates exist in the γ channels between the coarse γ' precipitates [35].

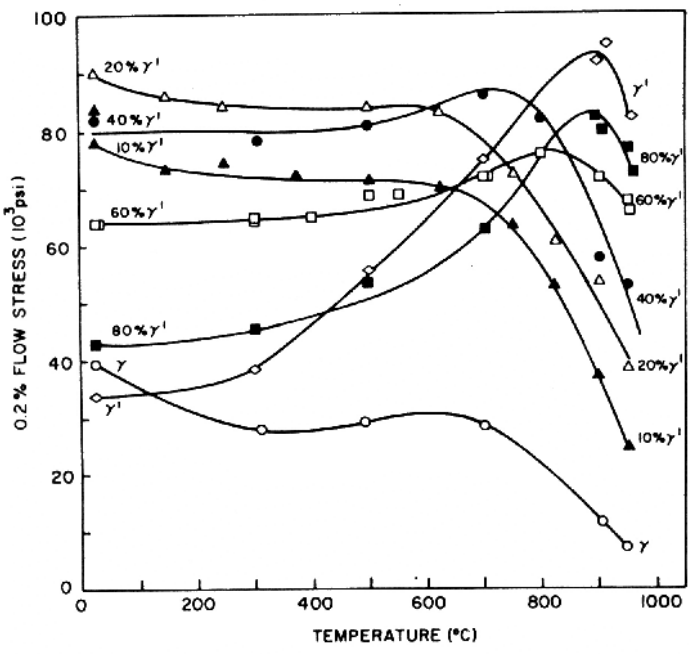

Figure 1.8 The effect of γ' volume fraction and test temperature on the proof stress of a Ni – Al - Cr superalloy. Maximum peak proof stress is obtained at 900 °C, and for a precipitate volume fraction of 1. Increasing volume fractions of γ' give progressively higher peak strength temperatures but, up to 60 % γ' volume, the peak strength falls [35].

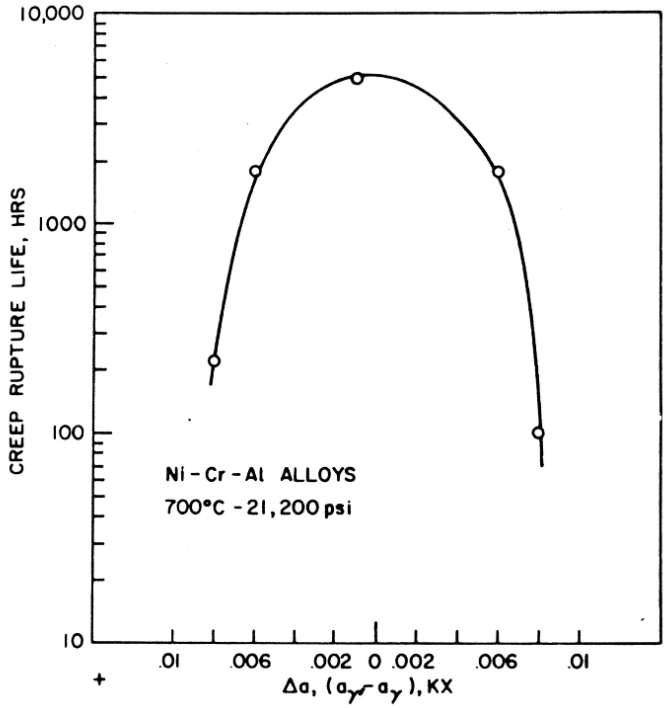

Figure 1.9 The creep life of a simple Ni – Al - Cr superalloy plotted as a function of the misfit. The maximum creep life is obtained at zero misfit (at test temperature, rather than room temperature), since there is no driving force for precipitate coarsening at this misfit [35].

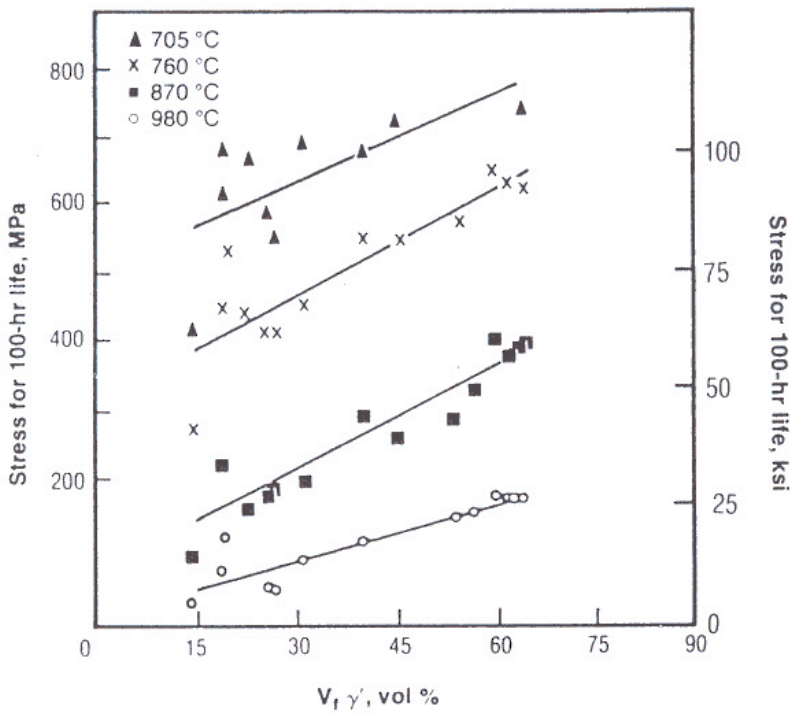

Figure 1.10 The effect of the volume fraction of γ' on the creep life [35].

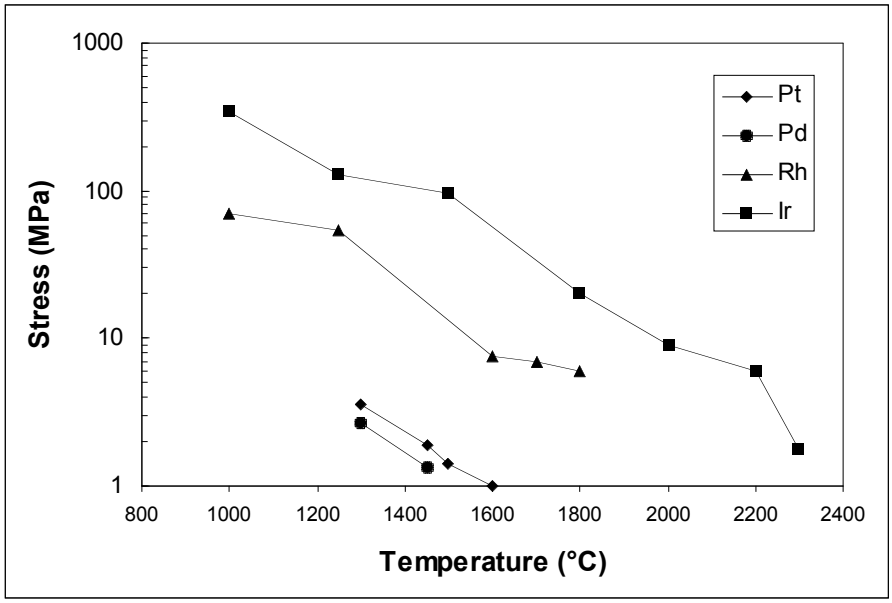

Figure 1.11 The stress required to produce failure in 10 hours for the f.c.c. PGMs in vacuum. The creep life at a given temperature scales with the melting temperature. (After Darling [53])

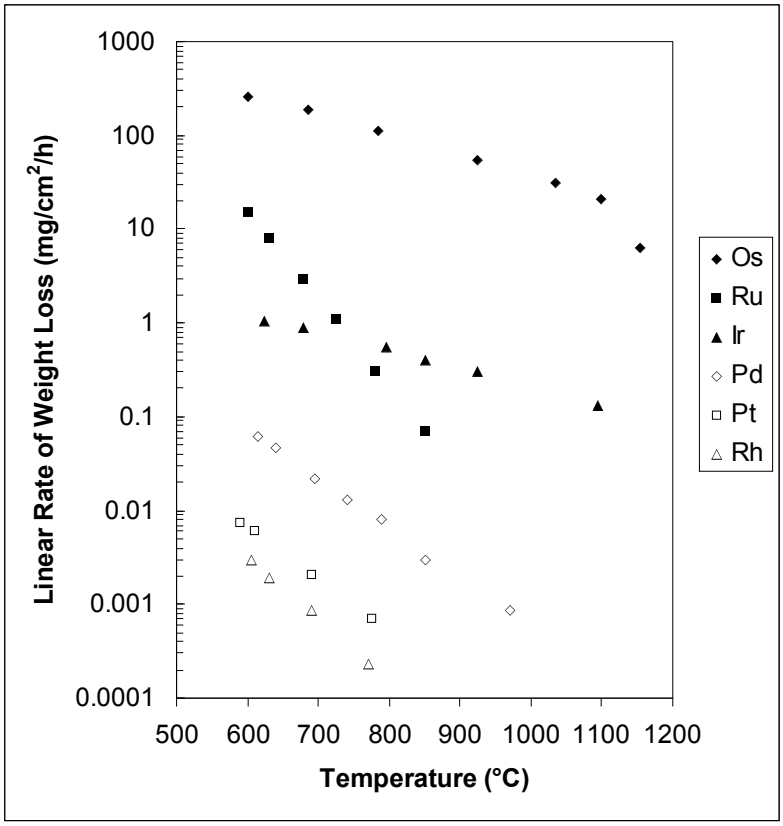

Figure 1.12 The oxidation behaviour of the PGMs in still air, plotted as mass loss rates versus temperature. (After Krier and Jaffee [57])

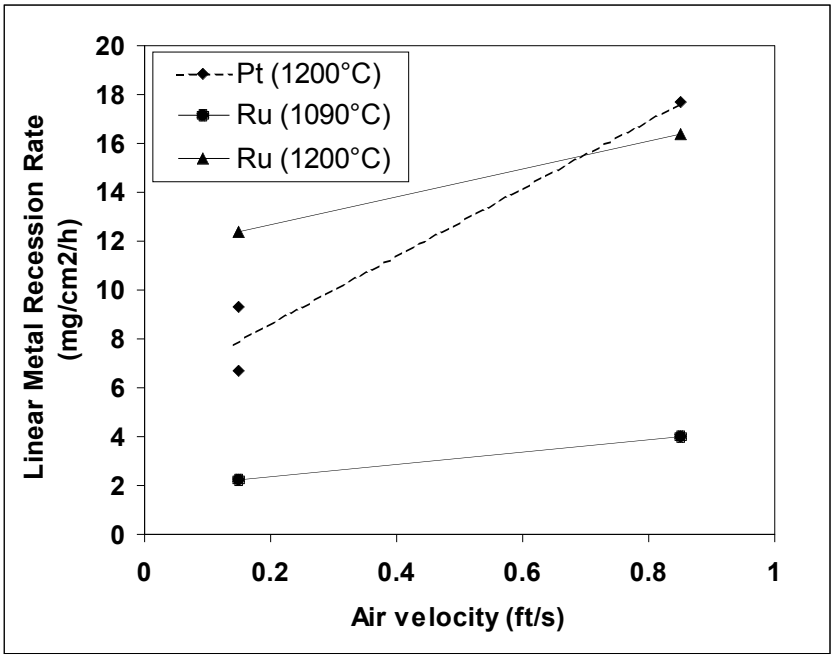

Figure 1.13 The effect of flowing air on the mass loss rates of the PGMs. The flowing air will remove the volatile oxides from the test chamber, leading to a lower-than-equilibrium partial pressure of the oxide, and hence further oxidation and evaporation to attempt to regain equilibrium. (After Krier and Jaffee [57])

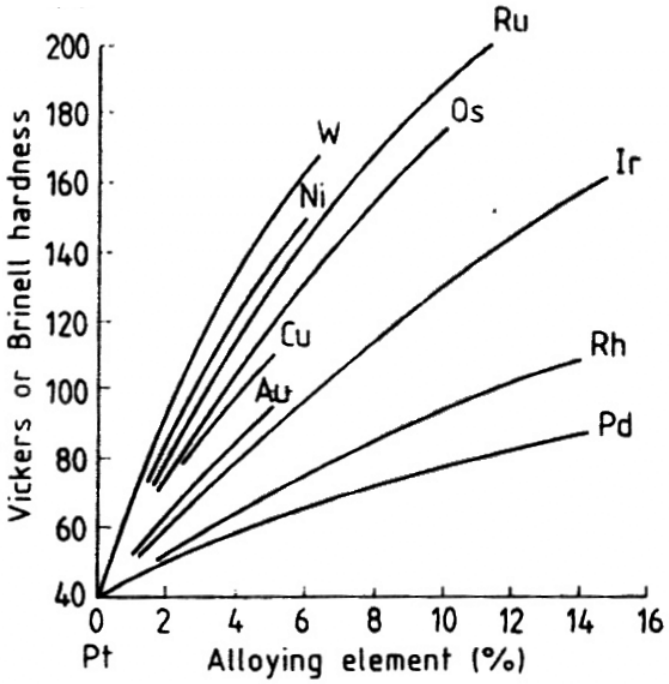

Figure 1.14 The effect of small levels of solute elements on the proof stress of platinum The most potent strengtheners are Ni, W and the hexagonal PGMs [58].

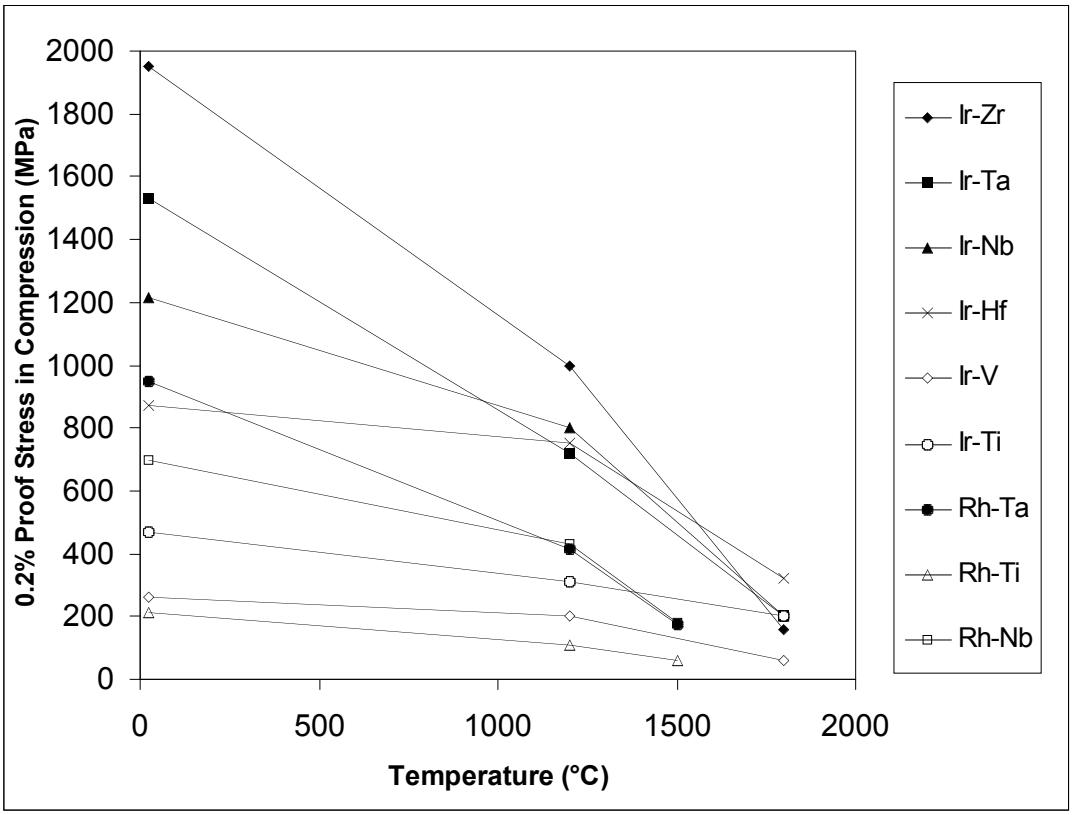

Figure 1.15 The proof stress in compression versus temperature for some of the PGM alloys developed at NRIM/NIMS in Tsukuba, Japan. The Ir - Nb alloy is the strongest known at 1200 °C and 1500 °C. (After Yamabe-Mitarai et al [62])

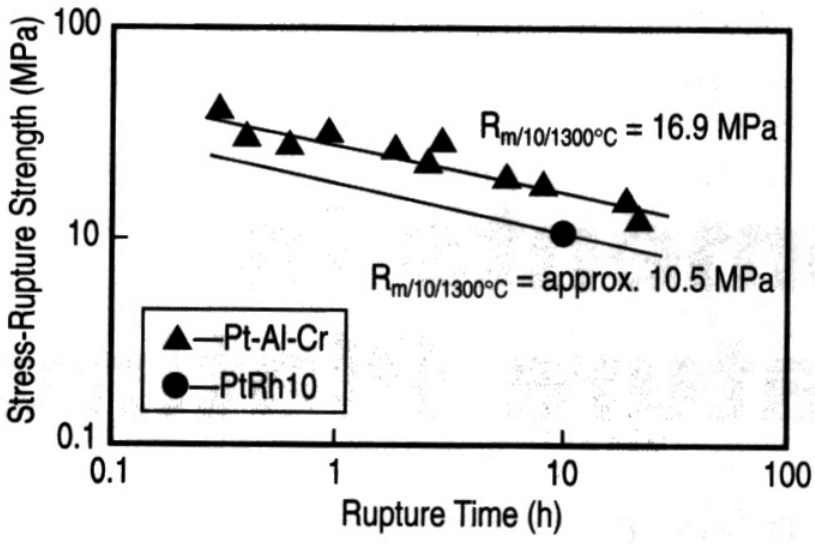

Figure 1.16 The stress-rupture behaviour of the Pt - Ti - Cr alloy developed by Hill and co-workers. The creep life is several times better than pure Pt and single-phase alloys such as Pt – 10 wt%Rh [73].

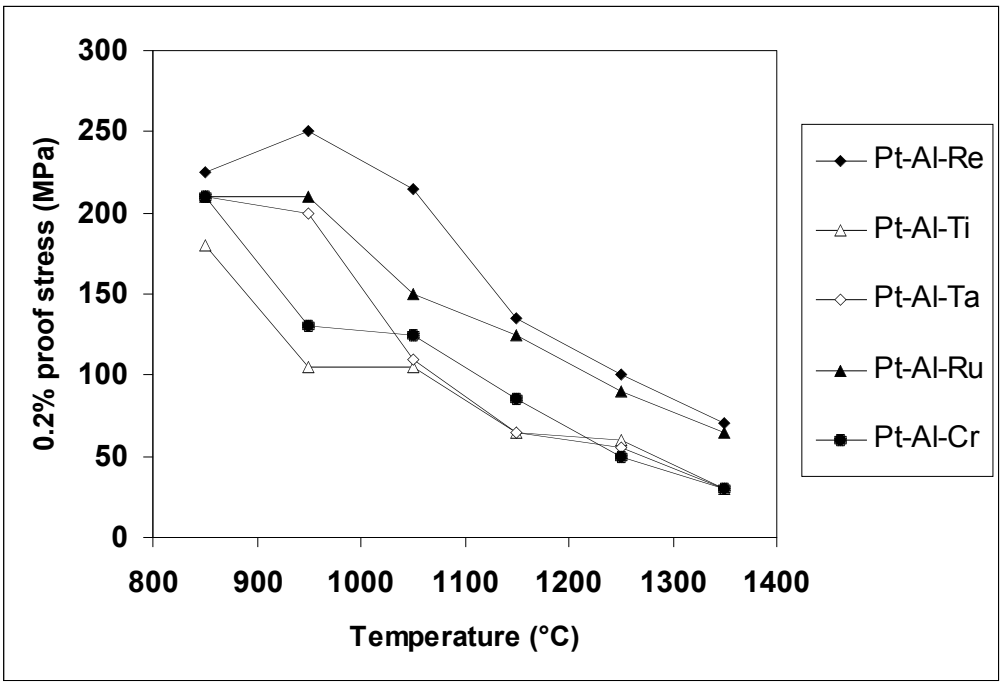

Figure 1.17 The proof stress versus temperature of some of the alloys developed by Hill and co-workers. (After Hill et al [70])

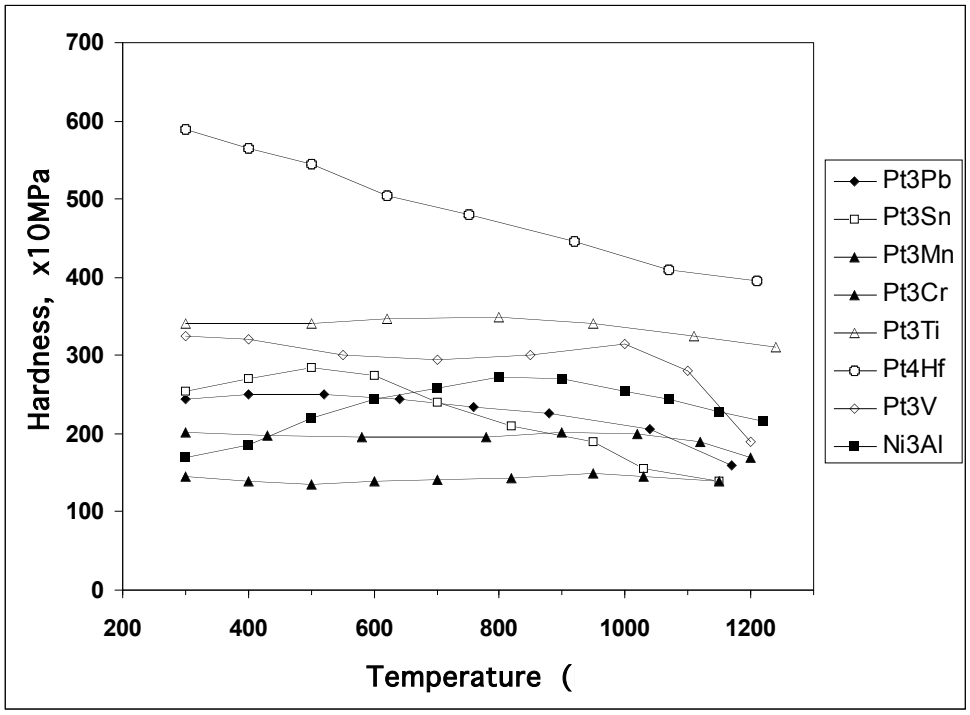

(a)

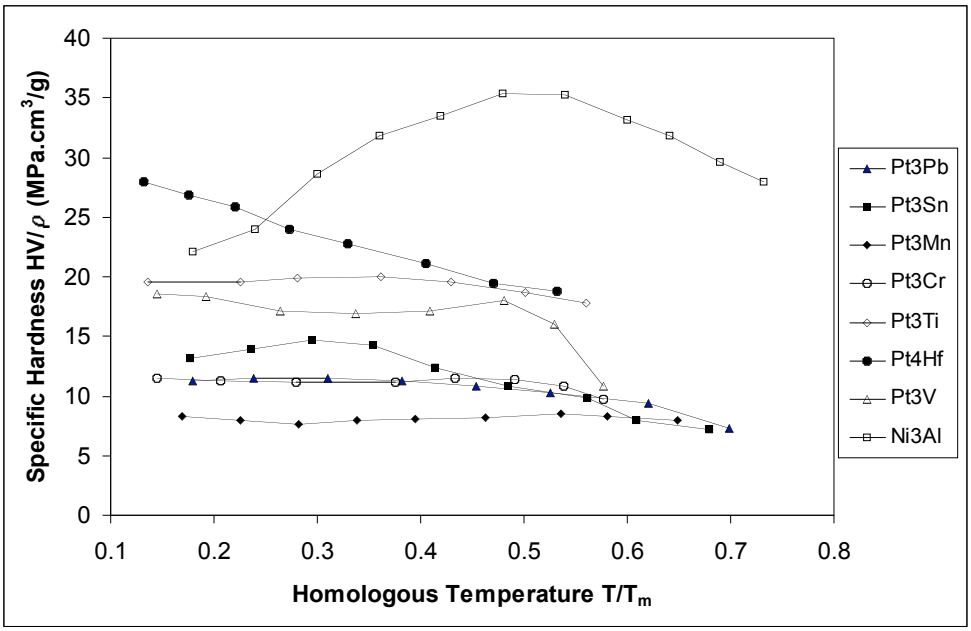

(b)

Figure 1.18 a) The hot hardness of some Pt-based $L1_2$ intermetallics and Ni_3Al plotted as a function of temperature. From this plot, Ni_3Al does not appear to be superior to the other phases. (After Wee and Suzuki [79])
b) The data in (a) plotted as specific stress versus homologous temperature. The peak specific stress of Ni_3Al is far superior to that of the Pt-based phases, whilst the position of this peak is not much different to those Pt-based phases which exhibit a peak stress.

Chapter 2 Phase Equilibria in the Pt - Hf and Pt - Zr Systems

In this chapter, investigations into the phase equilibria of the Pt - Hf and Pt - Zr binary alloy systems are described. Uncertainty surrounds the number and nature of the phases present in many Pt-based alloy systems. Before an alloy with a suitable microstructure can be identified for development, the phase equilibria must be understood to an extent that a target composition range and heat-treatment window can be established. Without this knowledge a coherent two-phase alloy with the optimum volume fraction of second phase over a temperature range cannot be produced.

There is a distinct lack of published work on most Platinum Group Metal (PGM) - based binary and ternary systems, including the Pt - Hf and Pt - Zr systems. There is no existing Pt - Hf binary phase equilibrium diagram, and the few papers that have been published on the subject (reviewed below) have reported conflicting results on the number and nature of phases in Pt-rich compositions in both systems. In this chapter the focus will be the Pt-rich end of the Pt - Hf and Pt - Zr binary phase equilibrium diagrams, up to a maximum of 25 at%Pt.

At present the only commercial application of a Pt-Hf alloy is in glassmaking, as with Pt - Zr alloys, where Oxide Dispersion Strengthened (ODS) Pt is used in the production of optical grade glass. Platinum strengthened by a fine dispersion of HfO_2 has been shown to possess at least equivalent properties to that using ZrO_2 as the dispersoid [1,2].

2.1 The Pt-Hf Binary System

2.1.1 Previous Phase Equilibria Work on Binary Pt-Hf Alloys

There are several papers in the literature (reviewed below) that deal with the phases present or the thermodynamics of Pt - Hf alloys, but none that have attempted to draw together all these data to produce a binary equilibrium diagram. Several phases have been reported in

the region from pure Pt to 25 %Hf: the hexagonal compound Pt_3Hf, a cubic compound of unknown stoichiometry, and the Pt-based f.c.c. solid solution.

All previous investigations into the Pt-Hf binary system [3-7] agree that the compound Pt_3Hf has the Ni_3Ti structure, a hexagonal superlattice designated DO_{24} (see figure 2.1 for structural diagrams of all superlattices referred to in this chapter). In addition to this compound, some investigators have observed another phase with uncertain stoichiometry, which possesses the $AuCu_3$-type superlattice.

Erdmann and Keller [3] produced "Pt_3Hf" with both the Ni_3Ti and $AuCu_3$ structures by reducing HfO_2 with H_2 in the presence of Pt at 1200 °C - 1600 °C for 40 hours. They determined the oxygen content of this alloy to be 520 ppm, and did not detect any loss of either component after reaction. Their analysis was by X-ray diffraction using the Debye-Scherrer method.

Meschter and Worrell [4] produced $L1_2$ "Pt_4Hf" in addition to Pt_3Hf, in a sample that was "oxygen-saturated". The solubility range of their "Pt_4Hf" was 15 – 23 at%Hf and its existence appeared to be confirmed by their lattice parameter measurements. They determined the solubility of Hf in Pt at 1000 °C to be approximately 10.5 at%, based on X-ray diffraction measurements, and did not detect the presence of any Pt_8Hf in their alloys. Their sample preparation was unusual as they used pellets for EMF experiments containing a mixture of alloy and HfO_2, which was pressed into a button and sintered under Ar. On the basis of existing data plus their new measurements they produced a diagram (see figure 2.2) describing the phase relationships at 1000 °C, with lattice parameter results used to determine the phase boundaries.

Holcombe [5] produced a composition that would produce the Pt_5Hf intermetallic (if such a phase existed). After vacuum annealing at 1800 °C, Pt_3Hf (DO_{24}) and (Pt) were the only phases they detected. During subsequent heating to determine the melting point a reaction was recorded at approximately 1820 °C to form a single tetragonal phase (a = 8.0 Å, c = 11.69 Å), which remained after cooling to room temperature and was stable during further heating and cooling cycles. This sample was contained in a W crucible during the

heating, and it is possible that upon heating a reaction occurred, although no ternary information is available in the literature for the Pt-Hf-W system to confirm this.

Raman and Schubert [6] published information regarding a range of alloys in the centre of the Pt - Hf diagram, but did not investigate the Pt-rich end. Four years later, Krautwasser, Bhan and Schubert [7] published another paper in which they produced an alloy at the $Pt_{89}Hf_{11}$ composition by arc-melting. This was subsequently powdered by filing, sealed under Ar in quartz ampoules and subjected to one of two heat treatments: for 120 h at 520 °C or 12 h at 750 °C. There was no evidence found of the existence of Pt_8Hf. The detection method used was X-ray diffraction in this case.

2.1.2 Previous Phase Equilibrium Work on Ternary Systems Containing Pt and Hf

There has been only one paper published on a ternary or higher system containing both Pt and Hf. During a determination by Kuznetsov and co-workers [8] of the Pt – Pd - Hf ternary phase diagram at 1000 °C (figure 2.3(a)) no phases other than Pt-based solid solution and Pt_3Hf were observed in Pt-rich alloys. Experiments using microprobe analysis, microhardness and XRD showed the solubility of Hf in Pt to be approximately 8.5 at%. They also calculated the likely form of the diagram (figure 2.3(b)), but did not present any thermodynamic properties for the phases Pt_4Hf and Pt_8Hf.

2.1.3 Experimental

Four binary compositions were chosen for clarification of the phase equilibria, based on gaps or uncertainties in existing data. These compositions were (in at%) 8, 13, 18 and 23 %Hf. Starting materials were Pt sponge (99.96%) and Hf sponge (99.8%, main impurity Zr). These alloys were pressed into pellets using a hydraulic press and arc-melted a number of times under Ar at a pressure of 0.8 - 0.9 atm. on a water-cooled copper hearth using a Ti getter prior to melting. Samples were then sealed in Ar-filled quartz ampoules and heat-treated in a chamber furnace at 1000 °C or 1100 °C for approximately 250 h. An attempt was made to equilibrate alloys at a higher temperature (1600 °C) in a vacuum

furnace, but a reaction between the sample and the furnace interior destroyed the alloy, so no results were gained at temperatures higher than 1300 °C.

Phase structure determination was conducted in a Philips XRD with CuK_α radiation, using a θ-2θ scan with a step size of 0.05 °2θ, anode conditions of 40 kV and 40 mA and a step dwell time of approximately 10 s. Samples for XRD were cut from the heat-treated arc-melted ingot, plane ground on SiC paper to 1200 grade and mounted on a rotating stage to improve sample strength as the samples were polycrystalline rather than powdered.

Accurate room-temperature lattice parameters were determined using Philips X'Pert profile fitting analysis software, which was capable of determining lattice parameters accurate to four decimal places in some cases. A threshold for least squares averaging was set at 0.2 °2θ from calculated peak position, above which peak positions were discounted for the lattice parameter measurement.

Imaging (in compositional backscattered mode) and compositional analysis (EDS) was conducted in a JEOL 5800LV SEM operating at 30 kV, after metallographic preparation to a colloidal silica final polish. As the average atomic number of the phases in the alloys was quite similar the signal contrast was low, so image contrast was artificially increased and the final image was averaged over, typically, four frames. Some additional images were obtained using a CamScan S2 SEM typically operated at 20 - 30 kV in backscattered electron imaging mode.

Samples for TEM examination were prepared from most alloys. A 3mm disk or smaller slice was sectioned or punched from the bulk alloy and was thinned by mechanical grinding on SiC paper to a thickness of 100 μm before polishing on 6 μm and 1 μm diamond pads. A spherical dimple was ground into one surface of the foil using a Gatan model 656 Dimple Grinder to give a thickness of 20 μm in the centre of the foil. Final thinning was achieved by ion thinning in a Gatan PIPS (Precision Ion Polishing System), with a typical schedule being 45 minutes at 5 kV gun voltage to achieve foil perforation followed by a 30 minute polish at 2 kV to remove the damage from the previous ion

polishing operation. Analysis of samples was carried out in a Philips CM30 TEM operating at 300 kV and a JEOL 200CX TEM operating at 200 kV.

2.1.4 Results and Discussion

The four phases observed in this investigation, as discussed below, had the following crystal structures and stoichiometries/compositions – f.c.c. (< 7 %Hf), Pt_8Ti (Pt_8Hf), $L1_2$ (close to 20 %Hf) and DO_{24} (Pt_3Hf). These phases will here after be referred to as (Pt), Pt_8Hf, γ' and Pt_3Hf respectively. All compositions discussed below, unless otherwise noted, are in at%.

2.1.4.1 Nominal Pt – 8 %Hf Samples

The as-cast material consisted of very large grains of a single phase. The composition was examined in the SEM and was found to be closer to 7 %Hf than the nominal composition (see table 1). Experiments using XRD showed that this single phase exhibited only f.c.c. reflections from (Pt), although as noted above this is not necessarily an indicator of the f.c.c. crystal structure.

After heat-treatment at 1100 °C the sample was single-phase (Pt) (see figure 2.4(a)). Analysis using XRD and electron diffraction in the TEM indicated that no second phase or superlattice lines/spots were present. In one electron diffraction pattern down <111> from what appeared to be a single-phase region some faint diffuse scattering was observed that was centred on the positions of Pt_8Hf superlattice spots, but no sharp superlattice spots were observed.

2.1.4.2 Nominal Pt – 13 %Hf Samples

The as-cast material (figure 2.4(b)) was two-phase, with dendrites of γ' in a matrix of Pt_8Hf. Analysis using XRD did not show separate peaks for the two phases, indicating the similarity in the lattice parameter of the γ' and the (330) planar spacing in the Pt_8Hf. These

crystal structures are illustrated in figure 2.1. Lattice transitions between the f.c.c. and Pt_8Hf structures are:

$$(h,k,l) = (3/2(h+k), 3/2(-h+k), l)$$

f.c.c. **Pt_8Hf**

After annealing at 1000 °C, there was obvious Hf diffusion out of the dendrites and development of a fine two-phase structure (see figure 2.4(c)), with extremely fine precipitation in the matrix phase. These two phases contained 11 and 20 %Hf, and while XRD only showed f.c.c. - like reflections (see figure 2.5(a)), TEM electron diffraction patterns revealed that the two phases were Pt_8Hf and γ' (see figure 2.5(b)). The weakness of the superlattice reflections is due to the similarity in atomic number of Hf (72) and Pt (78), resulting in a low difference in the atomic scattering factors. Erdmann and Keller [3] and Meschter and Worrell [4] have observed the γ' phase, but the Pt_8Hf phase has not previously been identified. The Pt_8M (M = another metal) phase is present in the Pt-Zr (see section 2.2.3 and references [4] and [7]), Pt-Ti [9] and Pt-V [10] binary systems. Given the similarity in alloying behaviour of Hf and Zr (they lie in the same group of the periodic table, with similar electronic configurations - Zr: 4d2 5s2; Hf: 5d2 6s2) it seems plausible that Pt_8Hf should form.

The stability of these phases cannot be explained by simple laws for compound formation, such as the Hume-Rothery rules [11]. These rules predict the stability of one crystal system over another (e.g. face-centred cubic versus hexagonal), but cannot account for long-range ordering within a given system, such as that found in the phases γ' and Pt_8Hf. Brewer developed a theory [12], based on the work of Engel [13], for predicting the stable crystal system of transition metal compounds based on "valence electron" concentration. This method was found to be most accurate for compounds consisting of two elements, one from each end of the transition metals, and Pt_3Zr was cited as a strong case. Again, however, this theory can only predict the stable crystal system and not the ordering tendency within a particular system [14]. Recent approaches to phase stability have used

ab-initio total energy calculations to determine the lowest-energy structure [15]. Such an undertaking requires many months of work, and is beyond the scope of the present study.

The estimation of the γ' phase boundary by Meschter and Worrell [4] at 15 %Hf is not in agreement with the XRD results presented above. The work of Meschter and Worrell was based on XRD measurements of the lattice parameter in a two-phase field. They only produced one alloy that lay in the two-phase field, and so their estimates of phase boundaries may be inaccurate, as they did not conduct any EDX microanalysis. Holcombe [5] did not observe either phase after vacuum annealing for 2 hours at 1800 °C, but as the analysis was also conducted using XRD then it is possible the existence of the superlattice reflections was missed. Krautwasser, Schubert and Bhan [13] did not observe either γ' or Pt_8Hf, potentially because their annealing times and temperatures were not sufficient to allow large amounts of diffusion to occur to reach equilibrium (120 h at 520 °C and 12 h at 750 °C), and because they did not employ electron diffraction in their analysis.

The morphology of the two phases was not regular. The γ' adopted a morphology best described as ribbon-like, with varying thickness along the precipitate (see figure 2.6). Precipitate shape in a coherent system has been shown to be strongly related to the misfit, from spherical at zero misfit through cuboidal at low misfit to rod-like at higher misfit and finally plate-like (semi-coherent) at very high misfit, above which coherency of the precipitate is lost. The misfit at which these morphologies are present is dependent on the particular system, since other factors which vary from system to system such as surface energy and stress influence the precipitate shape [16].

The sample heat-treated at 1300 °C underwent a reaction with the silica tube, probably as the quartz had softened and collapsed under the stress created by the pressure difference between the exterior and interior of the tube. A second phase was noted in regions near to the surface, which had nucleated on the surface of γ' dendrites. The inter-dendritic regions were found to contain approximately 20 at%Si. No further analysis was conducted on this sample due to this contamination.

2.1.4.3 Nominal Pt – 18 %Hf Samples

The as-cast microstructure (figure 2.4(d)) consisted of three phases (as determined by EDX and SEM observation in backscattered electron mode): cellular dendrites of Pt_3Hf, coated with γ', in a matrix of Pt_8Hf or (Pt). X-ray diffraction analysis showed reflections from two cubic phases and one hexagonal phase, which is in agreement with the above composition results (the lattice reflections for the Pt_8Hf phase appear to be produced by a cubic phase, even though the phase is tetragonal).

Analysis of the as-cast alloy using electron diffraction revealed the presence of three distinct phases – a hexagonal superlattice, cubic γ', and a f.c.c. lattice with diffuse scattering between the main reflections. The location of the diffuse scattering in the latter phase was close to some of the locations where superlattice spots from the Pt_8Hf phase would be present. In a diffraction pattern taken from the two cubic phases down the <001> zone axis (figure 2.7(b)) this scattering was along the directions of the reciprocal axes a* and b*, located between the main {002} reflections at a relative spacing of close to 0.4 and 0.6 {002}. In addition to the above observations γ' superlattice reflections were observed.

The regions giving rise to the diffuse spots discussed above exhibited a "tweed" structure in bright-field imaging mode, as can be seen in figure 2.7(a). The tweed structure is found in intermetallics where a martensitic transformation occurs, such as NiAl and FePd, as well as high-temperature superconductors, some ceramics, and alloys undergoing phase separation (such as steel during tempering) [17]. It is generated in some cases by compositional inhomogeneity resulting from, for instance, solidification. This inhomogeneity causes local differences in transition temperature, such that pre-transitional effects (sometimes several hundred degrees above the bulk transition temperature) lead to local variations in strain, giving rise to the observed contrast [17].

After annealing at 1100 °C the sample was two-phase, although a large fraction of the sample was composed of lamellae, twins or possibly martensite (see figure 2.4(f)). Several

Pt-based alloy systems exhibit a martensitic transformation [18], so it is possible that this could be observed in this system. Analysis using XRD indicated a small volume fraction (< 10 %) of Pt_3Hf (possibly residual from the as-cast structure due to insufficient annealing time leading to inhomogeneity) and a majority of γ'. Superlattice peaks for the (100), (110) and (210) reflections from γ' were just visible in the XRD trace.

The electron diffraction results suggest that the heat-treated alloy was almost wholly γ', whilst the back-scattered electron images obtained in the SEM suggest a large proportion of a phase with the appearance of martensite which did not discernibly affect the diffraction pattern. Bright field images obtained in the TEM show two main features in the alloy – the presence of aligned precipitates within the γ' phase with a lenticular morphology (possibly f.c.c. precipitated during heat-treatment) and a plate-like phase (see figure 2.8). No electron diffraction patterns were obtained from this phase, although combined with the higher-temperature tweed effects noted in the 13 %Hf alloy it appears likely this is a martensitic phase.

2.1.4.4 Nominal Pt – 23 %Hf Samples

The as-cast microstructure (figure 2.4(f)) was mostly dendritic Pt_3Hf with a small amount of inter-dendritic γ' and Pt_8Hf or (Pt). After annealing at 1100 °C the microstructure was two-phase, similar to the as-cast microstructure, although most of the γ' had disappeared. Some curious regions that appear white in the BSE photomicrographs had the same composition as the bulk composition of the rest of the sample (see figure 2.4(g)). The XRD trace showed two phases (the γ' intermetallic and Pt_3Hf) confirming the EDX results. TEM analysis was not performed on this alloy.

2.1.5 Tentative Binary Diagram Construction

Using existing data as well as that gained in this investigation, a tentative diagram may be drawn for the Pt end of the Pt-Hf binary system. The main feature is the existence of a series of "cascading" peritectic reactions, as indicated by the as-cast microstructures and compositions. It is clear that the as-cast alloys contain (Pt) as the matrix rather than Pt_8Hf,

and that the Pt_8Hf phase dissociates before melting, most likely at a temperature of between 1100 °C and 1300 °C. The melting point determination of Holcombe [5] for a sample containing 16.7 %Hf has been discounted, since it appears this sample may have reacted with the W crucible on heating to produce a ternary compound.

The nature of the solid-state dissociation reaction of Pt_8Hf is uncertain from the data presented above. That it occurs as a solid-state reaction below the peritectic melting temperature at that composition is certain, though whether it takes the form of a peritectoid or eutectoid reaction is not clear. If it was to take the form of an eutectoid reaction, then there would have to be significant curvature of the solvus boundary between single-phase (Pt) and two-phase (Pt) + γ' connecting the lowest peritectic reaction temperature and the eutectoid temperature. This significant curvature requirement is due to the measurements of the (Pt) phase boundary at 1800 °C by Holcombe, who found the boundary must lie between 5 and 11 %Hf at that temperature. For this result to be consistent with the presence of an eutectic reaction, the solvus boundary must both pass through this composition range at this temperature and meet the eutectoid point at somewhat greater than 11 %Hf. This situation is illustrated in figure 2.9.

An alternative proposal provides a better fit to the existing data. Consider the situation where the Pt_8Hf phase decomposes in a peritectoid reaction, and the (Pt) solvus rises approximately vertically from the end of the peritectoid reaction horizontal to the lowermost peritectic reaction horizontal, passing through the range of composition determined by Holcome for the (Pt) solvus at 1800 °C. This is the author's preferred form of the diagram, and is given in figure 2.10.

2.2 The Pt - Zr System

2.2.1 Previous Phase Equilibria Work on Binary Pt - Zr Alloys

Several investigators have investigated the phase equilibria of the Pt - Zr system, and have published contradictory results about the presence of an $L1_2$ intermetallic phase. A phase

diagram exists in the literature based on the results of just three investigators. In the Pt - Zr system, most investigators agree that Pt_3Zr has the DO_{24} Ni_3Ti hexagonal structure [3,4,6,8,12,13,19-24]. Several other phases have been observed between the Pt-rich f.c.c. solid solution and the Pt_3Zr intermetallic, though the composition of these phases is often not certain.

The existing Pt - Zr binary equilibrium diagram [30] is based on three papers [19,21,24], and only acknowledges the presence of (Pt) and Pt_3Zr at the Pt end of the diagram. This diagram is essentially that of Darling, Selman and Rushforth [21], who were the first to produce a diagram for this region based on compositions containing less than 25 at%Zr. An earlier diagram [20] only has dotted lines for this region, despite several compositions having been investigated at below 25 at%Zr.

The first report of a phase with the Cu_3Au-type, cubic $L1_2$ structure was by Schubert [24], though no experimental details were given. The lattice parameter was given as 3.99 Å, and the phase was termed "$Pt_{3+}Zr$" as the stoichiometry was not known. It is unusual to suggest that the $L1_2$ structure will exist in an alloy which does not have 3:1 stoichiometry, though it has been observed in Au_4Zn at low temperature [25,26] with the so-called $L1_2(M_1M_2)$ structure, which has long-range ordering in two dimensions (the repeat length in terms of number of unit cells in the x- and y- directions is indicated by M_1 and M_2) as well as short-range ordering. It was also observed above in the Pt - Hf system. Schubert revised the composition of the $L1_2$ phase to Pt_4Zr in 1973 [27] as well as observing the Pt_8Zr phase (Pt_8Ti structure), but again experimental details were not reported.

During a determination of thermodynamic data of the Pt - Zr system, Meschter and Worrell [4] found "Pt_5Zr" (a line compound with the Cu_3Au structure) and also found Pt_8Zr (with a wide solubility range but no quoted structure). Their preparation technique involved mixing the powdered arc-melted alloy with ZrO_2 powder, pressing this into buttons and then sintering for several hundred hours at temperature near 1000 °C. Phase identification was carried out using X-ray diffraction. It is likely these alloys would have a high oxygen

content, and during the same authors' research into the Pt - Hf system they used the same preparation technique and found the alloys were "oxygen-saturated".

A recent paper [28] has used a similar preparation technique, though pieces of Pt (rather than the arc-melted alloy) were mixed with ZrO_2. These researchers detected the formation of Pt_8Zr on the outside of the Pt, confirming the results of Meschter and Worrell, and Schubert.

It is worth mentioning that, where reported, alloy preparation techniques most likely to lead to a higher oxygen level produced the Cu_3Au-type phase. The same does not appear to be true for carbon. Brewer [13] mixed powders of ZrC and Pt to yield Pt_3Zr (Ni_3Ti type) plus graphite, and despite the likelihood of some carbon in his alloy, a Cu_3Au-type phase was not observed.

2.2.2 Previous Phase Equilibria Work on Ternary Systems Containing Pt and Zr

At least two ternary phase diagrams have been produced (see figure 2.11) for systems containing both Pt and Zr (Pt - Zr - Y [29] and Pt - Pd - Zr [8]), and in both no intermediate phases were found between the Pt-rich solid solution and Pt_3Zr. This is in contradiction to the results of Schubert [27], Meschter and Worrell [4] and Xue and Dieckmann [28].

2.2.3 Experimental

Compositions and heat-treatments for the Pt-Zr system were chosen to fill in gaps in the existing data or to determine the phases present at a certain temperature. All compositions are in atomic percent unless otherwise stated.

In the Pt - Zr system, nominal compositions chosen were 8, 15, 19, 20 and 23 %Zr. These alloys were arc-melted in batches of 10 - 15 g on a water-cooled copper hearth, using Pt sponge (99.96 %) and Zr sponge or wire (99.5 %+). As some mass loss (0.1 - 0.5 g) was observed in most cases, actual compositions were determined using EDS in a JEOL SEM,

operating at 30 kV. Heat treatments were either 1000 °C for 250 h, 1100 °C for 168 h or 1300 °C for 50 h, which were carried out in a chamber furnace with the samples sealed in Ar-filled quartz ampoules. At the higher temperature some reaction occurred between the sample and the quartz; the surface was removed by wet grinding before x-ray diffraction (XRD) analysis. Phase determination was conducted in a Philips XRD with CuK_{α} radiation, using a step size of 0.05 ° and dwell time of 6 - 7 seconds. Composition analysis was conducted using energy-dispersive X-ray spectroscopy (EDS) in the above SEM, operating at 30 kV.

Photographs of the microstructures were obtained using a Camscan S2 SEM and the above JEOL SEM operating in compositional backscattered mode after metallographic preparation to a final polish using 0.05 μm colloidal silica.

Preparation of samples for TEM analysis was as described above in section 2.1.2 for the Pt - Hf system. Analysis was conducted using a Philips CM30 TEM and a JEOL 200CX TEM.

2.2.4 Results and Discussion

Measurements of the bulk composition of the alloys using EDS in the SEM were averaged over a number of different areas within the specimen. Due to the unfortunate overlap of the Pt-M and Zr-L peaks (at about 2.04 keV in the intensity versus electron energy spectrum) the Zr-K and Pt-L peaks were used for compositional analysis in all cases and standard ZAF corrections were made. These compositions are given in table 1. As the liquidus temperature of these alloys is quite high (> 1800 °C [21]) samples were also tested for W content (coming from the tip during arc melting), and in all cases it was found to be less than 0.5 at%.

Phase determination using XRD revealed the presence of phases with the Pt_8Ti, $L1_2$ ($AuCu_3$) and DO_{24} (Ni_3Ti) structures (hereafter denoted Pt_8Zr, γ' and Pt_3Zr respectively),

as well as the f.c.c. Pt-based solid solution (hereafter denoted (Pt)). The crystal structures and lattice parameters of the phases observed in all alloys are presented in table 2.

In all cases the Pt - Zr binary alloys had lower Zr then intended (see table 1), possibly through melt surface oxidation or combination of Zr with any oxygen remaining in the sponge Pt. A violent reaction occurred upon heating, which has been noticed before when melting Pt - Zr alloys [21]. As the primary phase is the Engel-Brewer intermetallic Pt_3Zr, a large amount of heat is evolved upon formation from the melt due to the thermodynamic stability of the phase. No oxides were observed within the bulk alloy, though there was a high degree of porosity, which seemed to be a combination of gas porosity and shrinkage cavities.

2.2.4.1 Nominal Pt – 8 %Zr alloy

The as-cast and heat-treated alloys appeared to both consist of large grains of a single phase. A backscattered SEM image of the heat-treated alloy is shown in figure 2.12(a); it can be seen that the structure appears to be single phase. Contrast between grains is due to electron channelling rather than compositional variation.

Analysis using XRD revealed the presence of two phases in the as-cast alloy, suggesting the alloy was mostly f.c.c. with a small amount of γ'. After heat-treatment all the peaks of the $L1_2$ phase were more prominent than in the as-cast pattern. No Pt_8Zr superlattice peaks were observed in the XRD pattern, despite the structure factor being large enough to allow detection in the XRD.

The Pt_8Zr phase was found to be present in the alloy using electron diffraction (figure 2.12(b)), despite the appearance of the alloy being large single grains of (Pt). The superlattice spots in the electron diffraction pattern taken down {001} were quite faint, and no splitting of the main peaks into two separate peaks at higher diffraction angles was observed. It is hence likely that the volume fraction of Pt_8Zr was very low in this alloy.

2.2.4.2 Nominal Pt – 15 %Zr Alloy

The as-cast alloy (figure 2.12(c)) had very low porosity, and was mostly (Pt) with a small volume fraction of primary γ' dendrites. This suggests that the bulk composition of the alloy is quite close to the (Pt) composition at the peritectic temperature (T_p).

The sample heat-treated at 1000 °C (figure 2.12(d)) exhibited precipitation of γ' throughout the alloy. The location of former dendrites is evident at low magnification. At high magnification the precipitates can be seen to be not aligned along a certain direction, but rather seem to have formed as "colonies", much like pearlite in plain-carbon steels but with a more lath-like morphology at the corners of polygonal "cells". The composition of the γ' precipitates is approximately 17 %Zr, which suggests that there is a solubility range of a few percent in the γ' phase field. In the XRD trace for this alloy (see figure 2.13), γ' superlattice peaks were present. The f.c.c. peaks split at high 2θ into two peaks with a mismatch of approximately 1 % (not α_1/α_2 peaks, which have a mismatch of 0.25 %), and as the minor phase (which appears dark in figure 2.12(d)) contains approximately 19.3 %Zr this suggests it is most likely γ', since it is nearest the correct stoichiometry. The lattice parameters of these phases (see table 2.2) agree well with the published values of Schubert et al. [24,27] and Meschter & Worrell [4]. The XRD trace (see figure 2.13) for this alloy showed reflections from both the Pt_8Zr and γ' ($L1_2$) phases. The low-order lattice reflections from the Pt_8Zr and γ' phases coincide due to the small lattice mismatch. The superlattice reflections demonstrate that both phases are largely ordered.

After heat treatment at 1300 °C for 50 h, precipitation of (Pt) occurred within the γ' dendrites and γ' precipitated in the (Pt) region immediately surrounding the dendrites (see figure 2.12(e)), suggesting there was some Pt diffusion into the dendrites and Zr diffusion out of them. These precipitates were relatively large (approximately 1μm in size), were of a different morphology and size than those at 1000 °C and were aligned along definite crystallographic directions (the growth axes of the dendrite). Analysis using EDS showed that the composition of the γ' precipitates was close to Pt_4Zr. As noted earlier, this is highly unusual for an $L1_2$ crystal structure. There was definitely more precipitation within

the dendrites than in the region around them, though this cannot be taken as an indicator that the solubility of Zr in Pt is higher at 1300 °C than at T_p as the cooling from the melt was not under equilibrium conditions. In addition, the diffusion rates of Zr and Pt in γ' may also be different.

Electron diffraction patterns confirmed the results from the BE images and XRD pattern that two cubic (or cubic derivative) phases were present. The electron diffraction pattern shown in figure 2.12(b) was taken from a two-phase region down {001}, and very clearly shows two superimposed diffraction patterns, those of γ' and Pt_8Zr. It can be seen that this is a two-phase diffraction pattern by examining the relative position of the superlattice reflections halfway between the main reflections and those at 1/3 and 2/3 {200}. The reflections at, for instance, $\{3\bar{1}0\}_{\gamma'}$ and $\{\bar{3}10\}_{\gamma'}$ can quite clearly be seen to be off-centre relative to the surrounding Pt_8Zr superlattice reflections.

2.2.4.3 Nominal Pt - 19.0 %Zr alloy

The as-cast alloy (figure 2.12(f)) consisted of primary cellular dendrites [11] (see figure 2.14) containing 21 %Zr with a thin coating of the lower-temperature γ' phase (containing 17 %Zr), and the remainder of the alloy (about 0.9 volume fraction) being (Pt) containing 12 %Zr. The lattice parameters of these phases are different from that of stoichiometric Pt_3Zr due to the excess of Pt in the structure. The presence of cellular dendrites suggests a much higher cooling rate from the melt compared to the 15 at%Zr alloy. Some cracking within the plate-like dendrites was evident after casting, indicating that the phase is relatively brittle, and porosity was noted at the α grain boundaries, possibly from shrinkage on cooling.

After heat treatment at 1000 °C the alloy contained three phases. The soak time was insufficient to allow complete dissolution of the plates, and so the micrograph and XRD trace show evidence of as-cast Pt_3Zr as well as (Pt) and γ'. The peaks in the XRD trace corresponding to the Pt_3Zr decrease in height accordingly. The appearance of the bulk of

the alloy is identical to that of the nominal 15 %Zr alloy at 1000 °C (figure 2.12(g)), namely a two-phase mix ((Pt) and γ') that seems to have formed in "colonies".

After heat treatment this alloy exhibited similar behaviour to the 15 at%Zr alloy in terms of the morphology of the phases formed. After 50 hours at 1300 °C the alloy had transformed into two phases, (Pt) and γ', with some precipitation occurring near (what were formerly) the plates of the primary as-cast phase, as can be seen in figure 2.12(h). The XRD trace is consistent with reflections from two phases, with the misfit between the two phases being very small (see figure 2.15).

The cracks evident in the as-cast and heat-treated alloys in figure 2.12(f) meant that TEM samples were unable to be prepared from this alloy.

2.2.4.4 Nominal Pt – 20 %Zr alloy

The as-cast alloy was the only condition able to be investigated due to the alloy being destroyed during a high-temperature homogenisation treatment. The microstructure of the as-cast alloy consisted of a large proportion of blocky dendrites of Pt_3Zr, with a thin coating of γ' and a small amount of a (Pt) or Pt_8Hf matrix (figure 2.12(i)).

Electron diffraction analysis in the TEM revealed the presence of diffuse spots around the γ' superlattice spots, similar to those discussed in the Pt-Hf system arising from the tweed structure. The tweed structure was quite evident in bright-field images produced from this alloy (figure 2.12(j)). The diffuse spots observed in the diffraction pattern from this alloy (see figure 2.12(j)) were observed to extend in two orthogonal directions when observed down {011}: <002> and <110>. This would seem to indicate that this alloy may be prone to martensite formation, although none was observed in the sample examined.

The above discussion indicates that in this sample the matrix is (Pt) rather than Pt_8Zr, and that Pt_8Zr dissociation is a solid-phase reaction occurring several hundred degrees below the melting temperature of the 11 %Zr composition. This is because the tweed structure is

associated with the f.c.c. (austenite) – martensite transition [17], indicating that the matrix of the as-cast alloy was (Pt), and that the satellite spots are not produced by any superlattice.

2.2.4.5 Nominal Pt – 23 %Zr alloy

The as-cast alloy (figure 2.12(k)) had primary dendritic hexagonal Pt_3Zr with a coating of another phase and a third phase in the intergranular regions. The coated dendrites again indicate a peritectic reaction, though the presence of three phases indicates two peritectic reactions. This three-phase mixture was evident in the XRD trace, which exhibited three overlapping peaks at higher 2θ, such as the (220) and (331) peaks.

After heat treatment at 1000 °C the alloy exhibited some persisting (Pt) as well as Pt_3Zr and γ', which was evident in both the microstructure (figure 2.12(l)) and the XRD trace. This suggests that the alloy may have attained local equilibrium though the time spent at 1000 °C was insufficient for the alloy to attain a state approaching overall equilibrium, so the composition results for the phases are likely to be slightly inaccurate. The γ' superlattice peaks were much stronger relative to the main (111) peak, indicating a higher degree of ordering at 1000 °C than upon solidification. Precipitation of γ' can be seen within the former Pt_3Zr dendrites, along what appear to be fixed crystallographic directions.

After heat treatment at 1300 °C the alloy appeared quite different from that at 1000 °C, suggesting the heat treatment was sufficient to attain an equilibrium state. A bright grain-boundary phase can be seen between some grains (in figure 2.12(m)), which was found (using EDX) to contain a substantial amount of silicon (approximately 20 %Si) and is thought to be due to reaction between the sample and the quartz ampoule during the heat treatment. The results for composition and crystal structure from this sample will not be reported, due to the unknown effect of the Si on the phase equilibria. As a result of this contamination, these results will be discounted below when producing the Pt - Zr partial phase diagram.

2.2.4.6 Modification of the Pt - Zr binary phase diagram

From the above information the nature of the Pt end of the Pt - Zr phase diagram can be deciphered. We now know there are two peritectic reactions in the composition range studied (from the as-cast microstructures in the alloys containing 15 %Zr and 19 %Zr) and that the primary phase in the as-cast 15 %Zr alloy (γ') is different to that of the 19 %Zr and 23 %Zr alloys (Pt_3Zr). The microstructures and EDX microanalysis results also suggest this, along with the vastly differing heat-treated microstructures in the 15 %Zr and 23 %Zr alloys. As in the Pt-Hf system discussed above, the main feature is again the cascading peritectic reactions and the peritectoid decomposition of the phase Pt_8Zr.

Using the measured compositions, and combining this data with data previously reported in the literature, the phase diagram can be modified to take the form shown in figure 2.16. The Pt_8Zr phase may be a line compound at 11.1 %Zr, and decomposes somewhere between 1000 °C and 1300 °C. The γ' phase exhibits a narrow range of composition, between 19.5 %Zr and 20.5 %Zr at 1000 °C and between 16.5 %Zr and 20.5 %Zr at 1300 °C, suggesting that its Pt solubility increases at high temperature. The tieline for the higher temperature peritectic reaction must end between 12.8 %Zr and 15.0 %Zr, due to the different primary phases formed in these alloys. It is understandable that Darling, Selman and Rushforth [21] missed the presence of the γ' phase when their compositions are taken into account – there is a large gap between their samples falling in the (Pt) region (up to 10 %Zr) and the next composition (at 18.5 %Zr). It is likely their "heavily twinned f.c.c." phase at 18.5 at%Zr (12.00 wt%Zr) and 1650 °C was γ' and not (Pt) as they believed, as the composition falls within the likely composition range of the γ' phase determined during this investigation. This diagram is very different to that published previously [30], which was based on just three papers for the Pt-rich phases.

2.3 Conclusions

The Pt-rich ends of the Pt - Hf and Pt - Zr binary systems have been investigated, and a tentative partial phase diagram for each has been drawn up to 25 at% Hf/Zr. A new phase (Pt_8Hf) with the Pt_8Ti structure has been observed. Due to the presence of this Pt_8Hf phase, a two-phase microstructure mimicking that of the Ni-base superalloys appears unobtainable in a binary Pt - Hf or Pt - Zr alloy.

2.4 References

1. E. P. Daneliya, M. I. Doperchuk and G. I. Kandyba, Metal Science and Heat Transfer, **30** 311 (1998).
2. E. P. Daneliya, M. I. Doperchuk and G. I. Kandyba, Russian Metallurgy, **4** 176 (1989).
3. B. Erdmann and C. Keller, Inorg. Nucl. Chem. Letters **7** 675 (1971).
4. P. J. Meschter and W. L. Worrell, Met. Trans. **8A** 503 (1977).
5. C. E. Holcombe Jr., J. Less-Common Met. **44** 331 (1976).
6. A. Raman and K. Z. Schubert, Metallkde., **55** 704 (1964).
7. P. Krautwasser, S. Bhan, and K. Schubert, Z. Metallkde. **59** 724 (1968).
8. V. N. Kuznetsov, G. P. Zhmurko and E. M. Sokolovskaya, J. Less-Common Met. 163 (1990).
9. P. Pietrokowsky, Nature **April 17** 291 (1965).
10. D. Schryvers, J. Van Landuyt and S. Amelincx, Mat. Res. Bull. **18** 1369 (1983).
11. A. Cottrell, *An Introduction to Metallurgy, Second Edition*, The Institute of Materials, London, 1975, p. 177.
12. L Brewer, in "Electronic Structure and Alloy Chemistry of the Transition Elements", Ed. P. A. Beck, Interscience Publishers, New York (1963).
13. L. Brewer, Acta Met., **15** 553 (1967).
14. L. Brewer and P. Wengert, Met. Trans., **4** 83 (1973).
15. Z. W. Lu and B. M .Kleinr, Phys. Rev. B, **50** 5962 (1994)
16. M. E. Thompson, C. S. Su and P. W. Voorhees, Acta Metall. Mater., **42** 2107 (1994).
17. S. Kartha, J. A. Krumhansl, F. P. Sethna and L. K. Wickham, Phys. Rev. B, **52** 803 (1995)
18. T. Biggs, M. J. Witcomb and L. A. Cornish, Mat. Sci. and Eng., **A273-275** 204 (1999)
19. H. J. Wallbaum, Die Naturwissenschaften, **7/8** 91 (1943).
20. E. G. Kendall, C. Hays, and R. E. Swift, Trans. Met. Soc. AIME, **221** 445 (1961).
21. A. S. Darling, G. L. Selman, and R. Rushforth, Platinum Metals Rev., **14** 124 (1970).

22. E. M. Savitskii, V. P. Polyakova, N. B. Gorina, and N. R. Roshan, *Physical Metallurgy of Platinum Metals.* Mir Publishers, Moscow (1978).
23. J. N. Prieskorn, H. Chen, W. Chen, and W. J. Tornquist, J. Phys. Chem. **96** 810 (1992).
24. K. Schubert, S. Bahn, T. K. Biswas, K. Frank, and P. K. Pandy, Die Naturwissenschaften **55** 704 (1968).
25. D. Schryvers, G. Van Tendeloo and J. Van Landuyt, Phys. Stat. Sol. A **75** 607 (1983).
26. N. M. Mateeva and E. V. Kozlov, *Ordered Phases in Metallic Systems*, Nova Science Publishers, New York (1996).
27. K. J. Schubert, Less-Common Met., **33** 1 (1973).
28. J. Xue and R. Dieckmann, Solid State Ionics, **53-56** 209 (1992).
29. Yu. J. Konobas, M. V. Raevskaya and I. G. Sokolova, J. Less-Common Met., **115** L5 (1986).
30. Binary Alloy Phase Diagrams, 2nd Edition, Volume 3, Ed.-in-Chief T.B. Massalski, ASM International, Materials Park (1990).

Table 2.1 Nominal and actual compositions of the alloys mentioned in this chapter.

Pt-Zr alloys		**Pt-Hf alloys**	
Nominal Composition (at%Zr)	Actual Composition (at%Zr)	Nominal Composition (at%Hf)	Actual Composition (at%Hf)
8.0	7.7	8.0	7.4
15.0	12.8	13.0	14.12
19.0	15.0	18.0	17.9
20.0	*	23.0	23.9
23.0	20.9		

** Not measured – sample contained significantly more Pt_3Zr than the 15.0 at%Zr sample.*

Table 2.2 Crystal structures and lattice parameters of all phases observed in heat-treated alloys in this chapter. Note that the lattice parameters will be for samples on the edge of the single-phase regions, since most samples were two-phase. For this reason the terms "lower" and "upper" have been used in relation to the two boundaries – "lower" and "upper" indicate the lower and upper limit of solubility (of Hf or Zr) respectively. The bracketed figure after the lattice parameter value relates to the error in the final significant figure.

Phase	Temperature	Sample (nominal composition and heat treatment temperature)	Lattice Parameter	
			a (Å)	c (Å)
Pt -Zr Alloys				
(Pt)	1100 – upper	8Zr1100	3.959 (2)	
	1300 – upper	15Zr1300	3.964 (2)	
Pt_8Zr	1000 – upper	19Zr1000	8.413 (3)	3.955 (4)
	1100 – upper	15Zr1000	8.411 (2)	3.960 (2)
γ'	1000 – lower	15Zr1000	3.997 (2)	
	1000 – lower	19Zr1000	3.9945 (8)	
	1000 – upper	23Zr1000	3.997 (1)	
	1300 – lower	15Zr1300	3.981 (2)	
Pt_3Zr	1000 – lower	23Zr1000	5.673 (7)	9.338 (9)
Pt - Hf Alloys				
(Pt)	1100	8Hf1100	3.954 (2)	
Pt_8Hf	1000	13Hf1000	8.400 (4)	3.955 (3)
	1100	18Hf1100	8.495 (4)	3.986 (2)
γ'	1000 – lower	13Hf1000	3.987 (3)	
	1100 – lower	18Hf1100	3.994 (1)	
Pt_3Hf	As-cast	23Hf as-cast	5.645 (3)	9.189 (8)

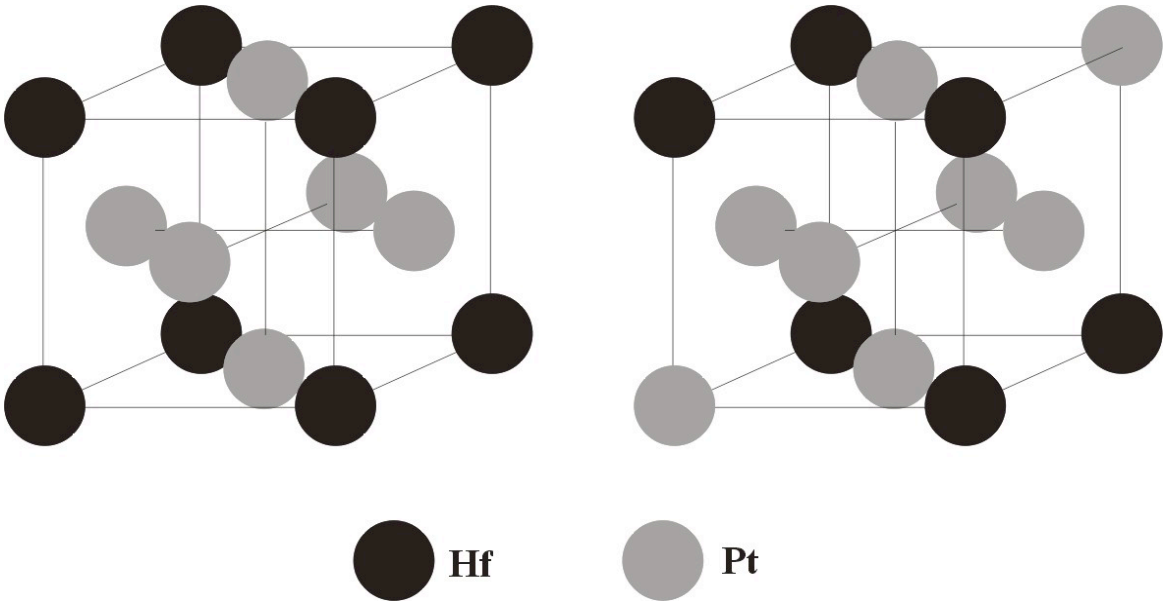

(a) (b)

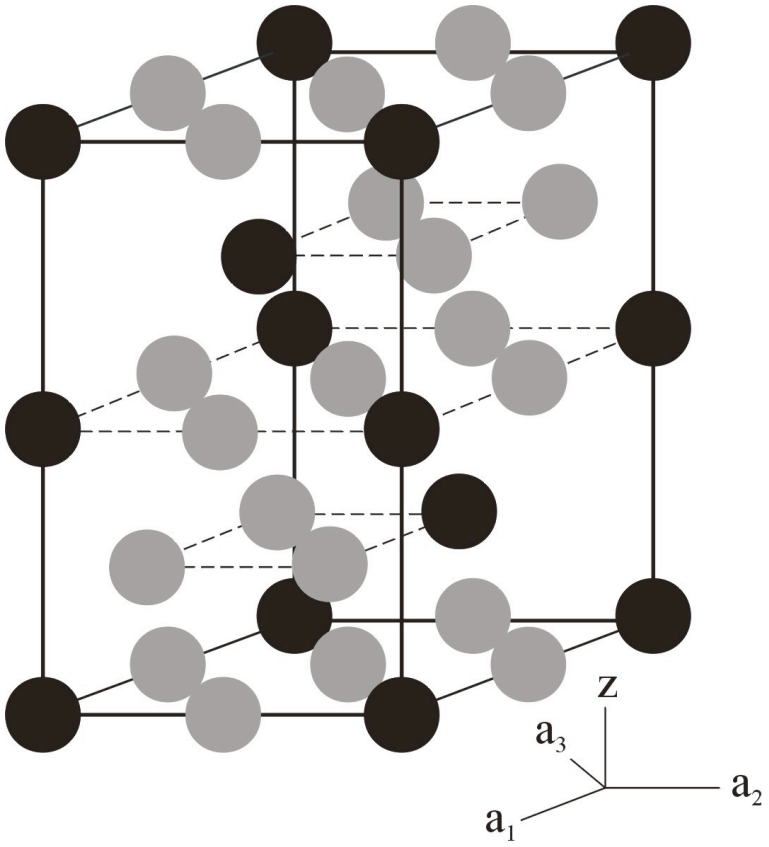

(c)

Figure 2.1 – caption on page 72

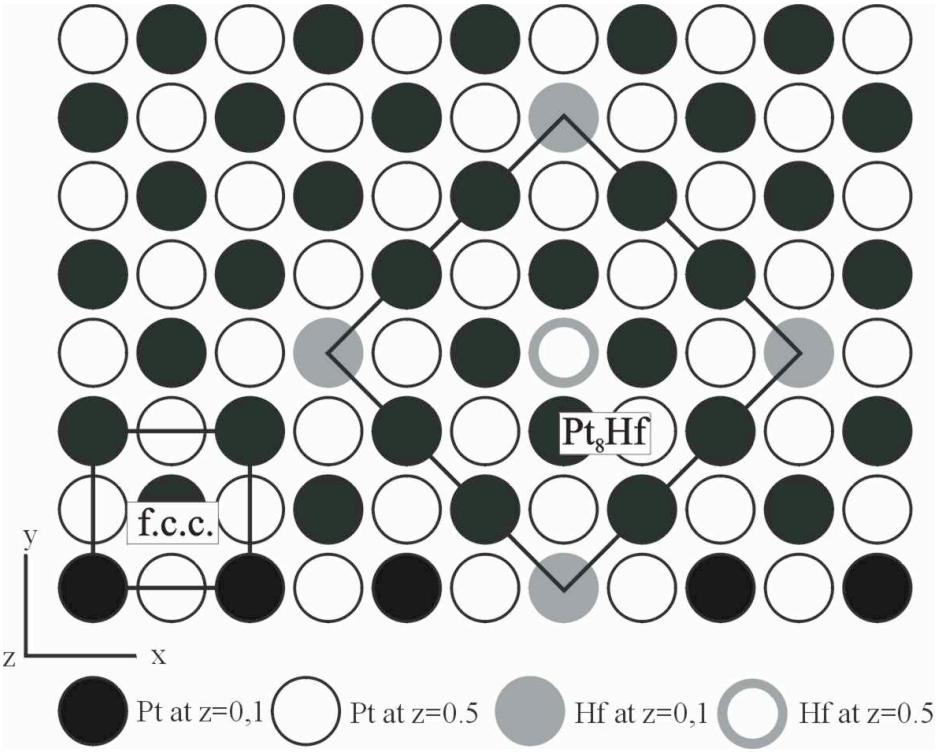

(d)

Figure 2.1 Superlattices in the Pt – Hf and Pt – Zr systems:
(a) ordered $L1_2$ structure (model: $AuCu_3$) with stoichiometry of 3:1,
(b) Daltonide $L1_2$ structure – random substitution of some Pt for Hf leading to a phase richer in Pt than that in (a),
(c) hexagonal $D0_{24}$ structure (model: Ni_3Ti) with stoichiometry of 3:1, and
(d) b.c.t. Pt_8Hf structure (model: Pt_8Ti) - atoms are in f.c.c. positions but ordering dictates a tetragonal unit cell.

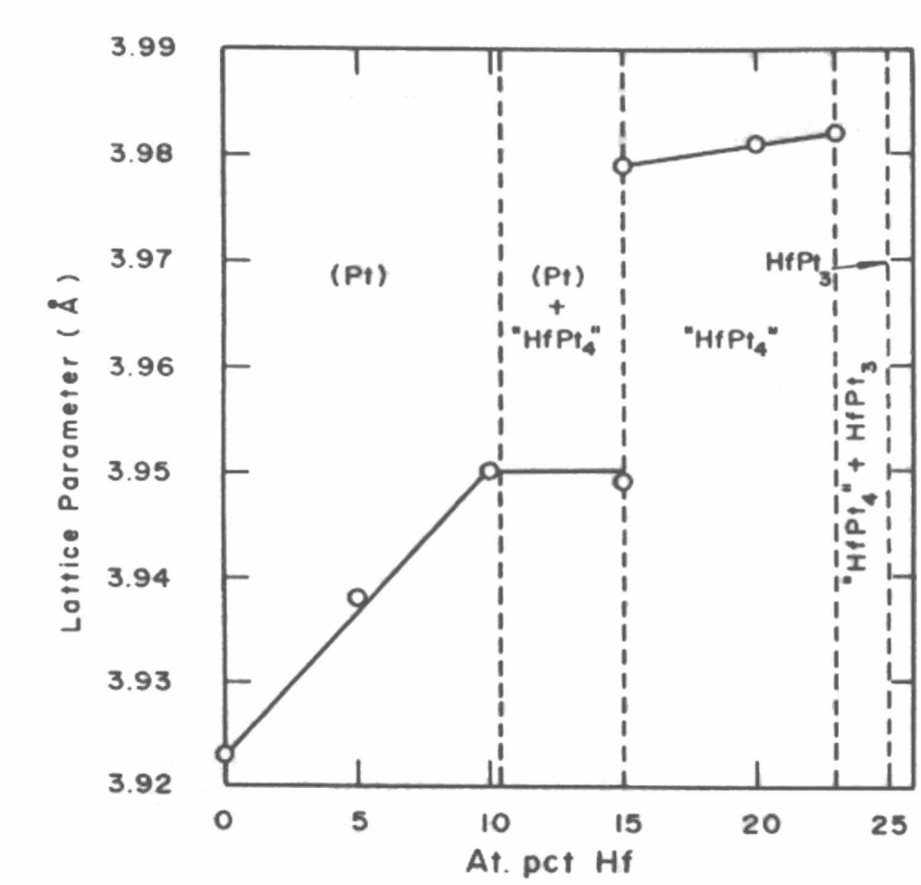

Figure 2.2 Meschter and Worrell's lattice parameter diagram for the Pt - Hf system [4]

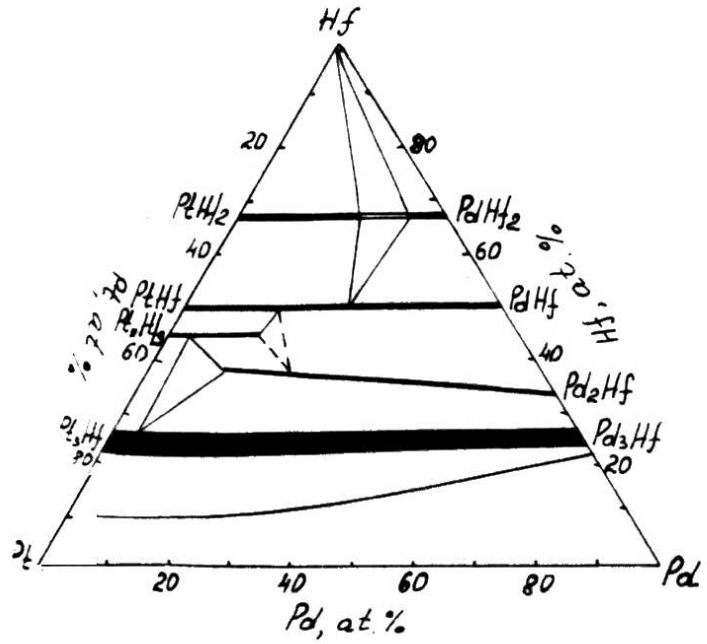

(a)

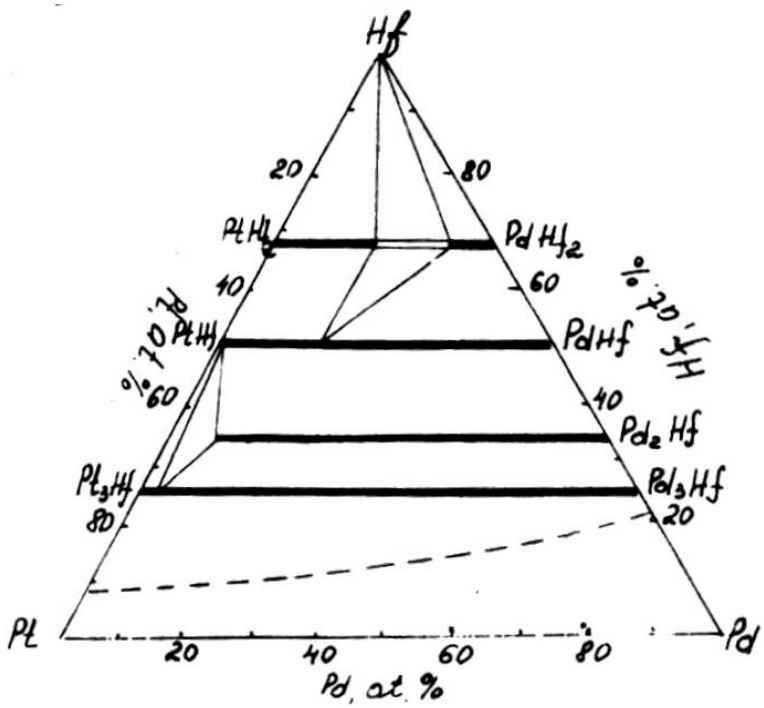

(b)

Figure 2.3 (a) the experimentally determined 1000 °C isothermal section of the Pt - Pd - Hf ternary phase diagram, and
(b) the predicted form of (a) using contemporary thermodynamic data [8]

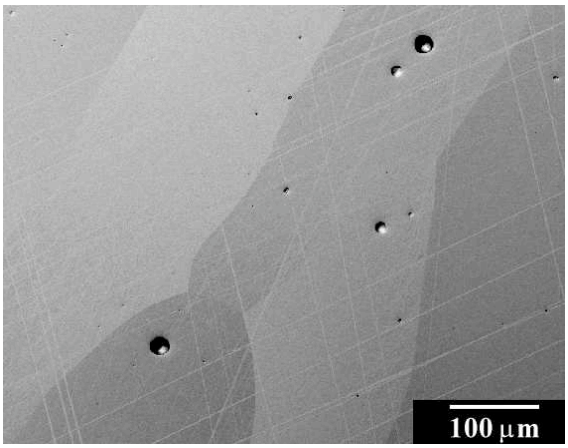

(a)

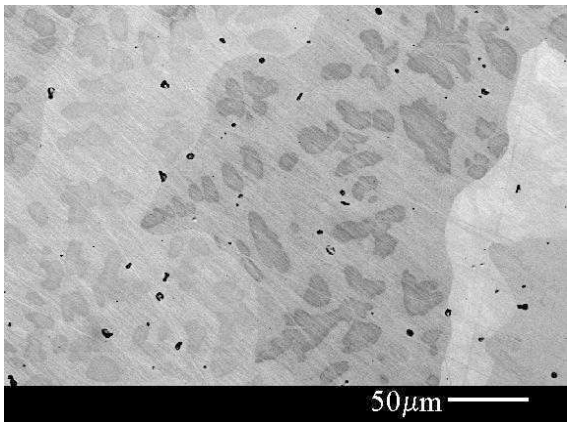

(b)

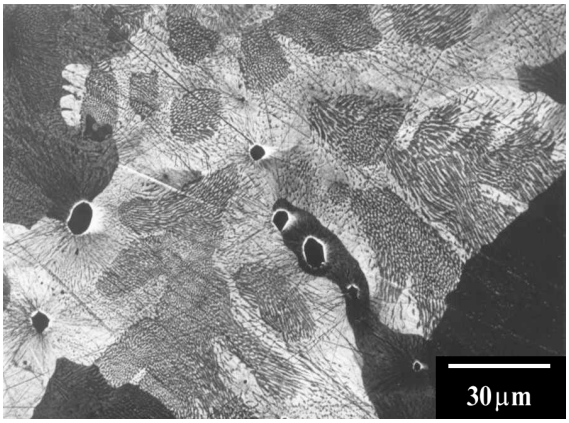

(c)

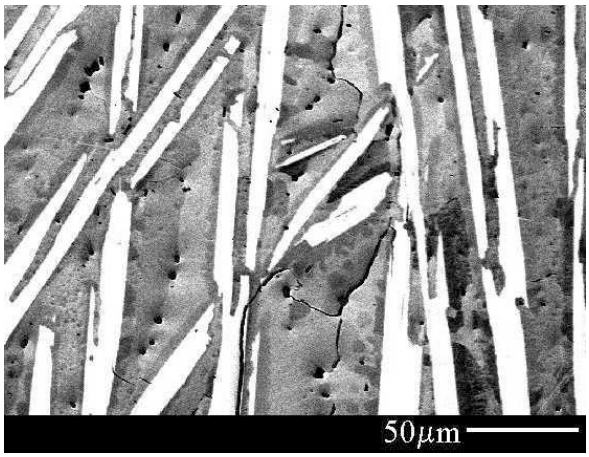

(d)

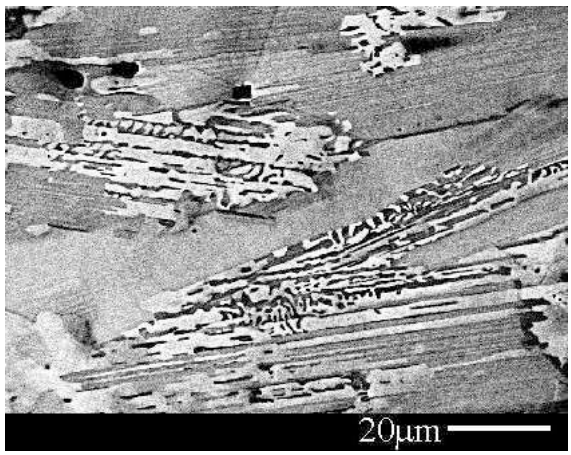

(e)

Figure 2.4 – for captions see page 76

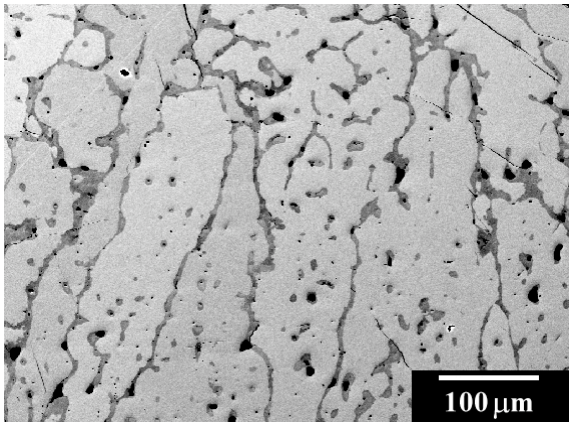

(f)

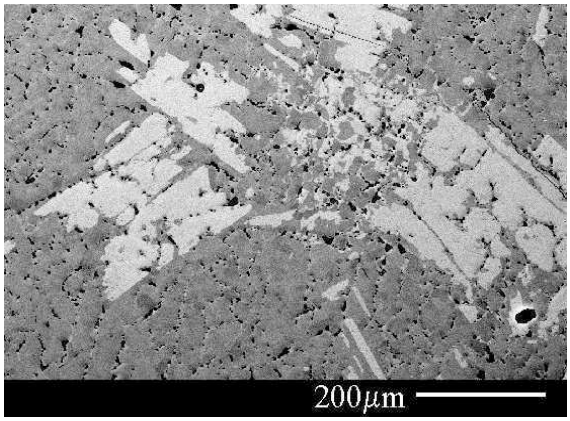

(g)

Figure 2.4 **A**s-cast and heat-treated Pt - Hf microstructures for all compositions. The as-cast 8 at%Hf alloy was single-phase.
As-cast alloys:
(b) nominal 13 at%Hf,
(e) nominal 18 at%Hf,
(f) nominal 23 at%Hf.
Heat-treated alloys:
(a) nominal 8 at%Hf, 1100 °C,
(c) nominal 13 at%Hf, 1000 °C,
(e) nominal 18 at%Hf, 1100 °C,
(g) nominal 23 at%Hf , 1100 °C.

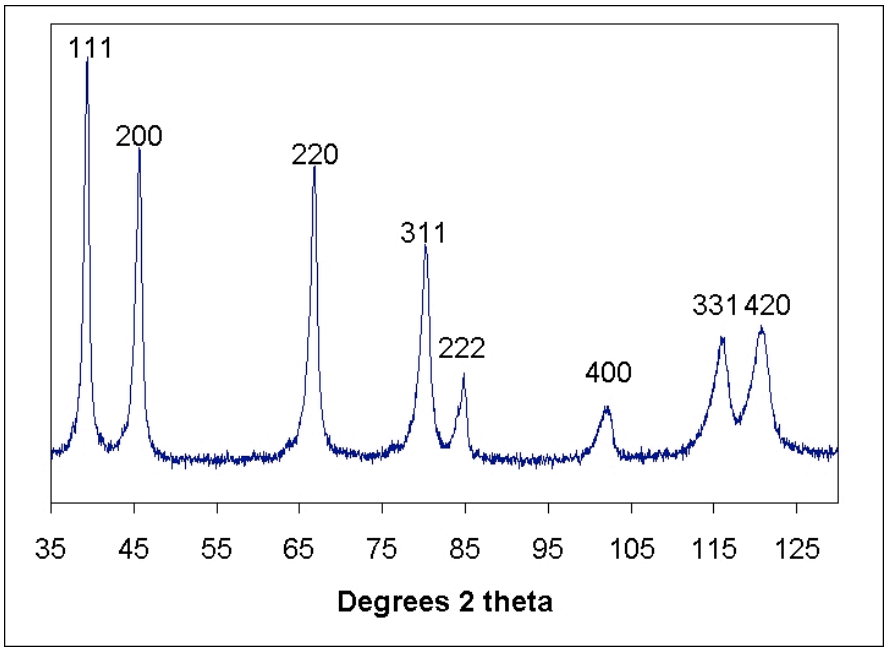

(a)

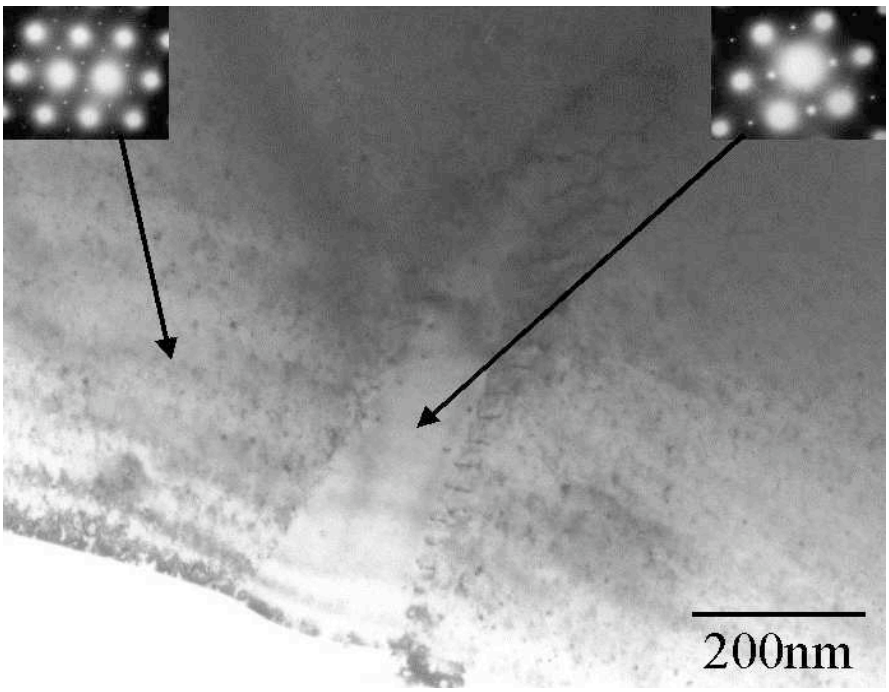

(b)

Figure 2.5 (a) XRD pattern for the 13 at%Hf sample after annealing at 1000 °C, and (b) a bright-field electron micrograph with the corresponding electron diffraction patterns of the two phases, taken down {110}. There is little evidence of the two-phase nature of the sample in (a), apart from slight peak asymmetry at high 2θ (caused by two phases of low misfit), whereas the electron micrograph and diffraction patterns quite clearly show the presence of the two distinct phases.

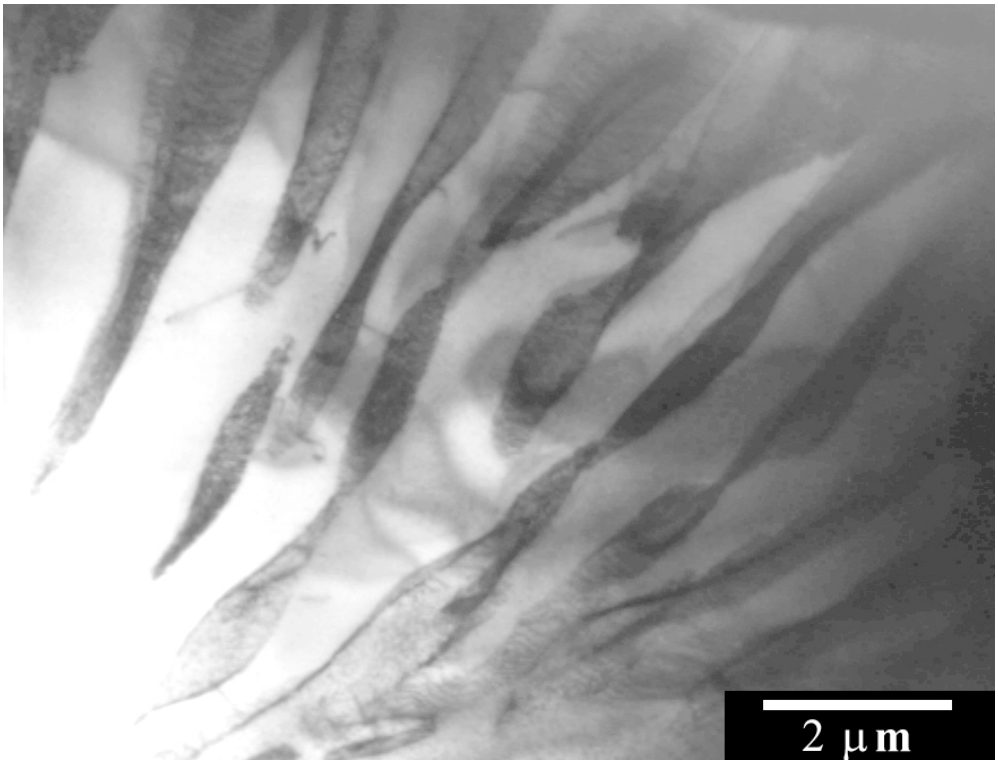

Figure 2.6 Bright-field TEM micrograph taken from the nominal 13 at%Hf sample, showing the ribbon-like morphology of the γ' (darker phase) in a matrix of Pt_8Hf.

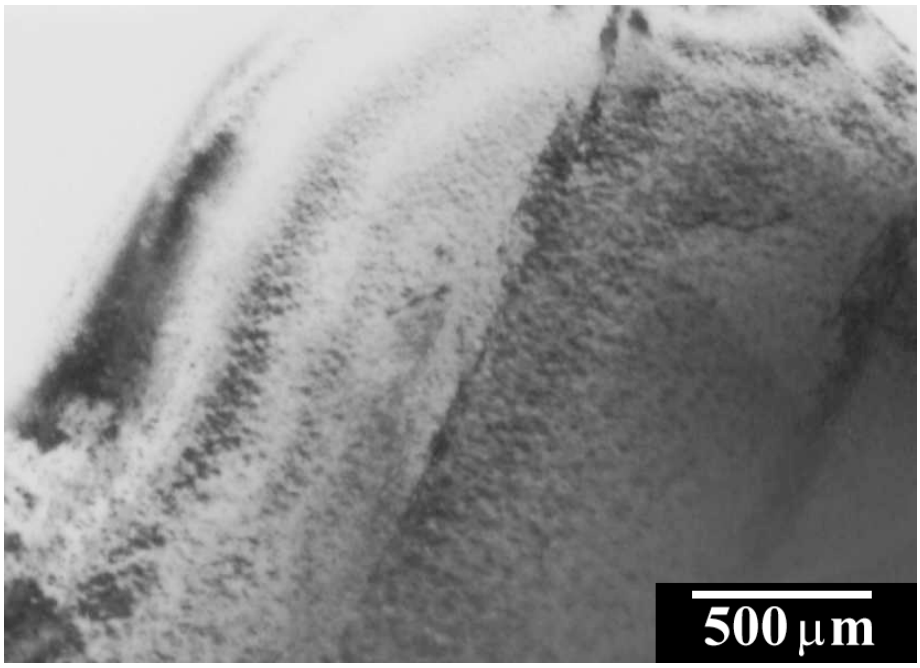

(a)

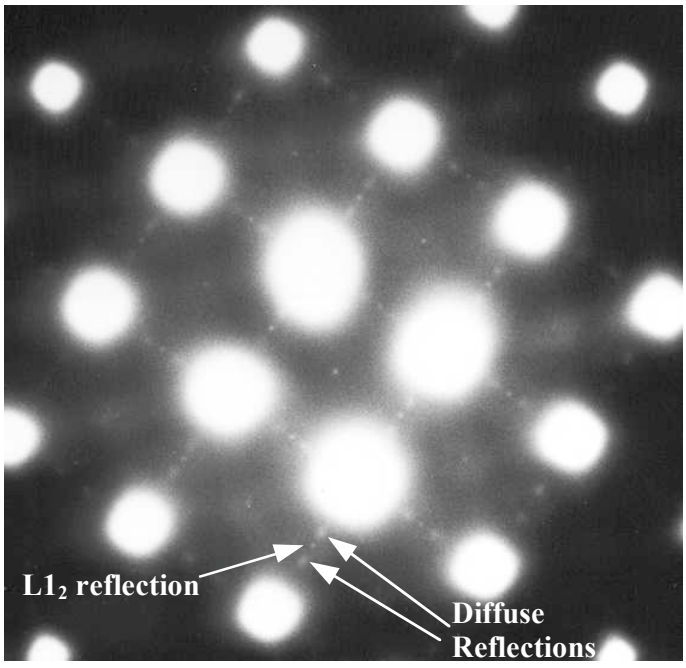

(b)

Figure 2.7 (a) Tweed microstructure in as-cast 18 %Hf, and
(b) the diffraction pattern from regions containing tweed taken down {100}.

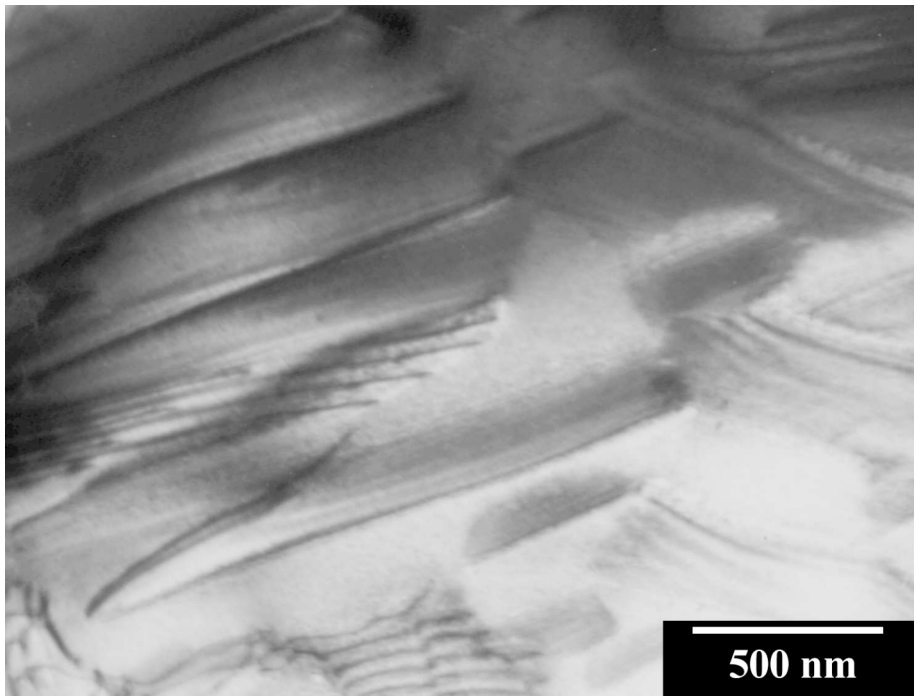

Figure 2.8 Possible martensite observed in the nominal 18 %Hf alloy after heat-treatment for 168 h at 1100 °C followed by water quenching.

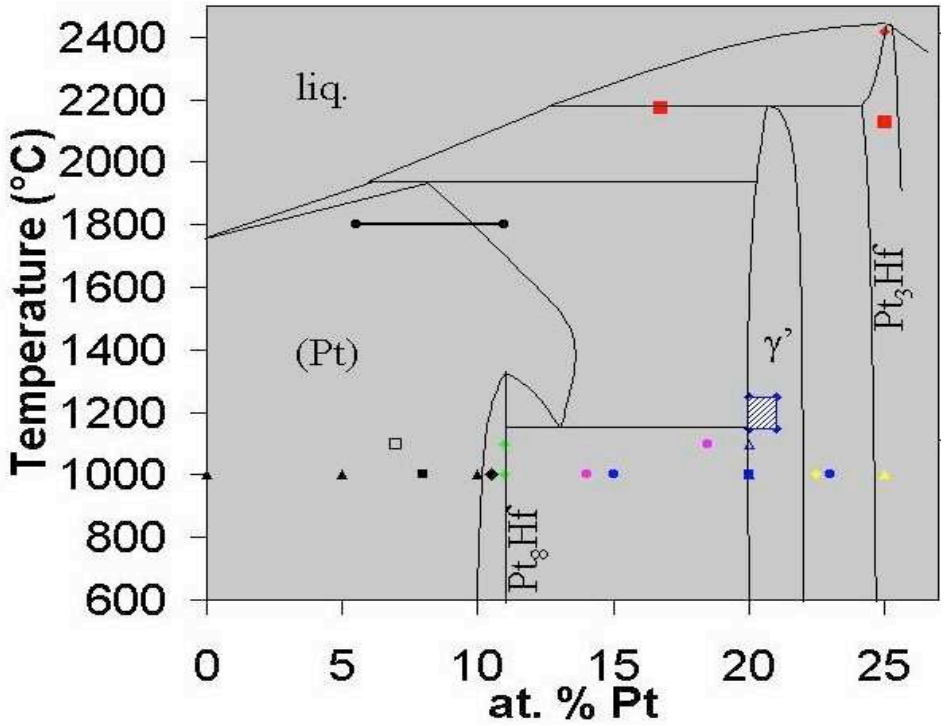

Figure 2.9 The form of the Pt-rich end of the Pt-Hf diagram required for the eutectoidal decomposition of Pt_8Hf. The (Pt) solvus above the eutectoid temperature must bend greatly to conform to the existing compositional data for the (Pt) solvus.

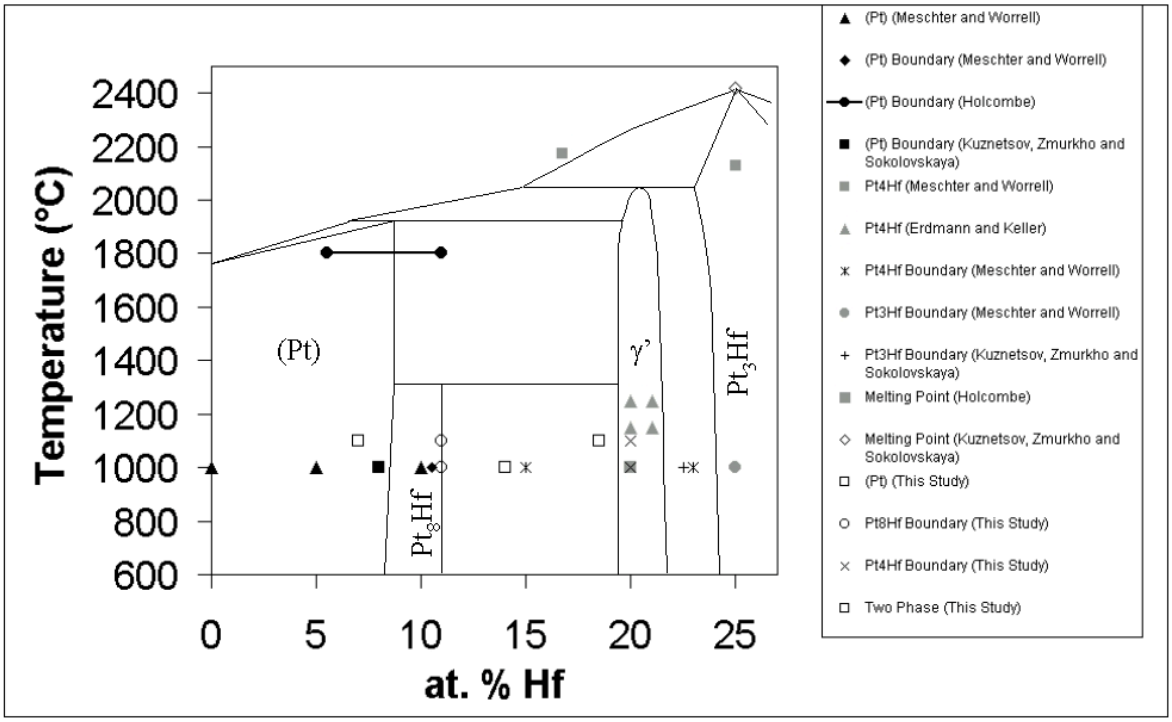

Figure 2.10 Tentative construction of the Pt-rich end of the Pt-Hf binary diagram.

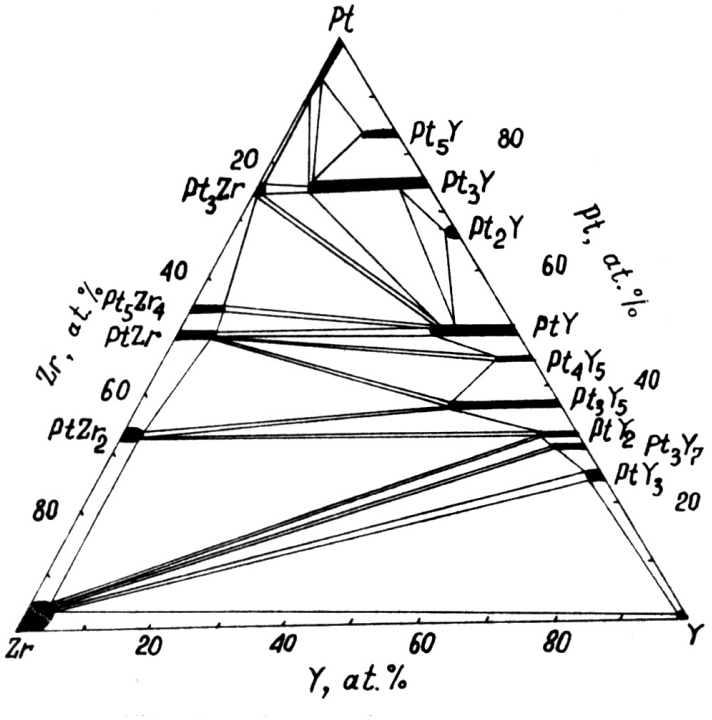

(a)

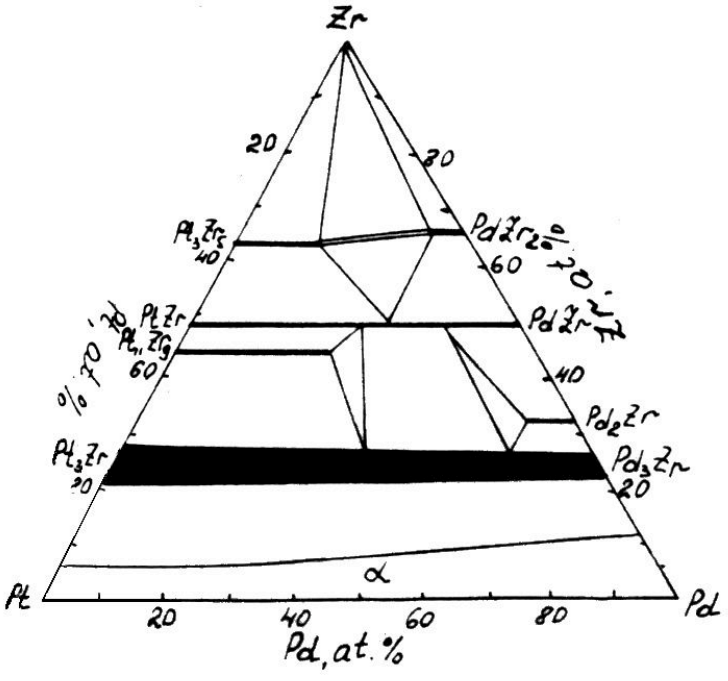

(b)

Figure 2.11 (a) The 1000°C isothermal section of the Pt - Zr - Y ternary phase diagram [29], and
(b) the 1000°C isothermal section of the Pt - Pd - Zr ternary phase diagram [8]

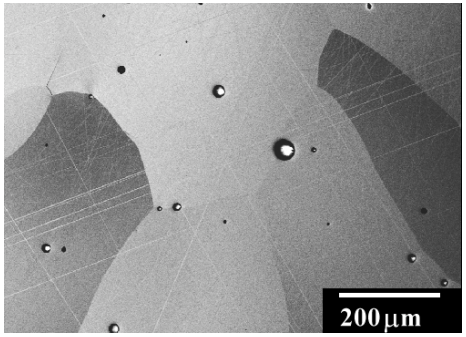

(a)

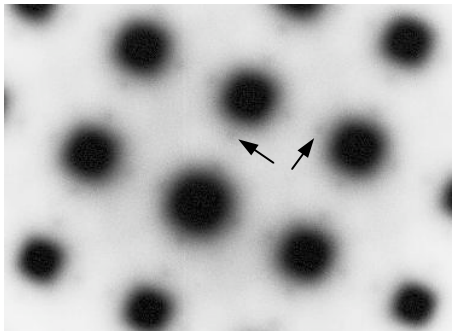

(b)

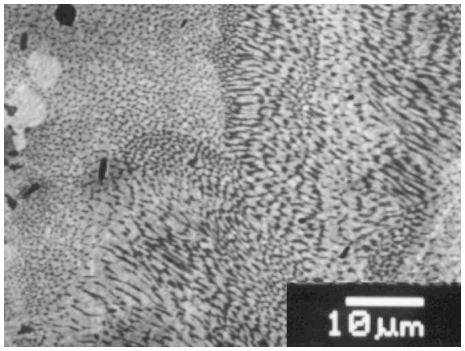

(c)

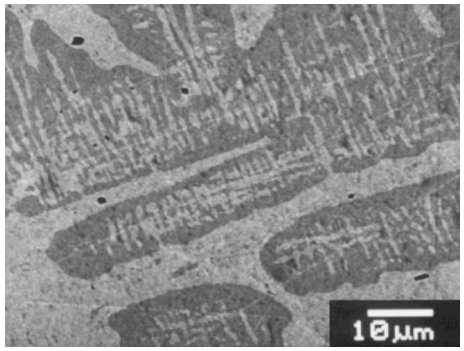

(d)

Figure 2.12 – for captions see page 85

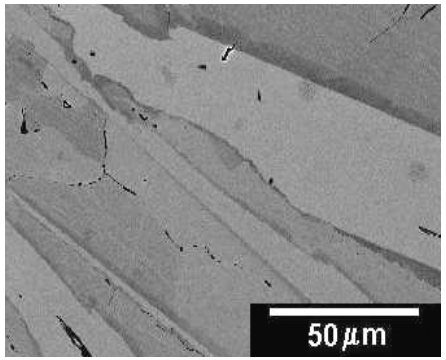

(e)

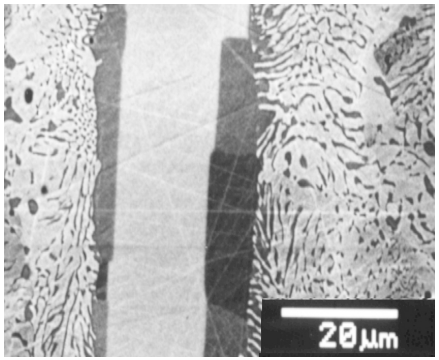

(f)

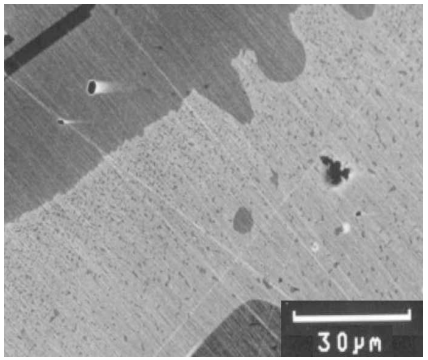

(g)

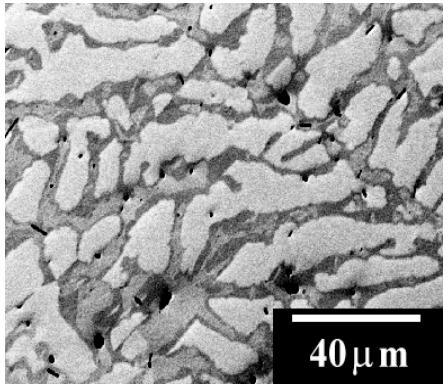

(h)

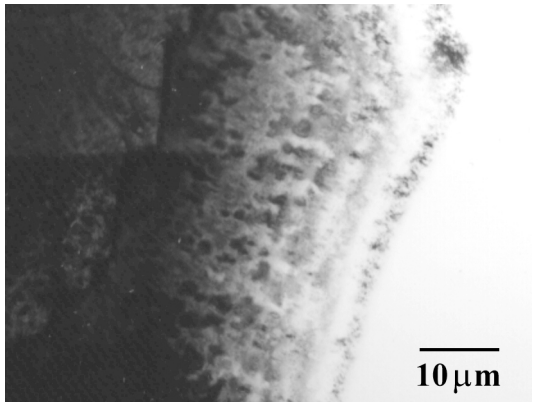

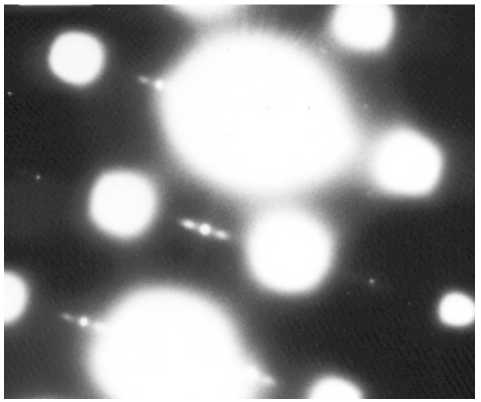

(i)

Figure 2.12 – for captions see page 85

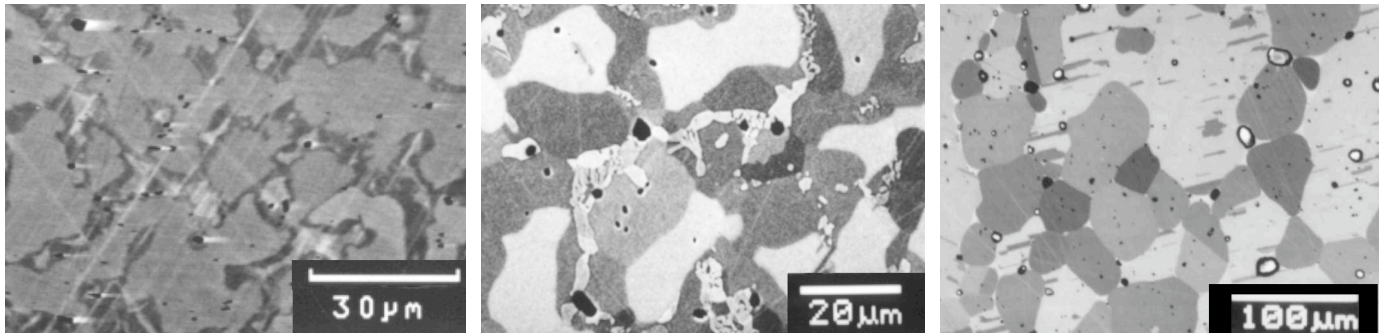

(j) (k) (l)

Figure 2.12 Microstructures of all as-cast and heat-treated Pt-Zr alloys and selected diffraction patterns:
(e), (h) and (j) as-cast nominal 19, 20 and 23 %Zr respectively;
(a) nominal 8 %Zr heat-treated at 1100 °C for 168 h, apparently showing large grains of a single phase and (b) two-phase diffraction pattern from the "single-phase" sample in (a) showing faint Pt_8Zr superlattice reflections;
(c), (f) and (k) samples of nominal 15, 19 and 23 %Zr respectively heat-treated at 1000 °C for 250 h;
(d), (g) and (l) samples of nominal 15, 19 and 23 %Zr respectively heat-treated at 1300 °C for 50 h;
(i) two-phase diffraction pattern from the inter-dendritic region of as-cast nominal 20 %Zr, illustrating the presence of $L1_2$ and lack of Pt_8Zr superlattice reflections

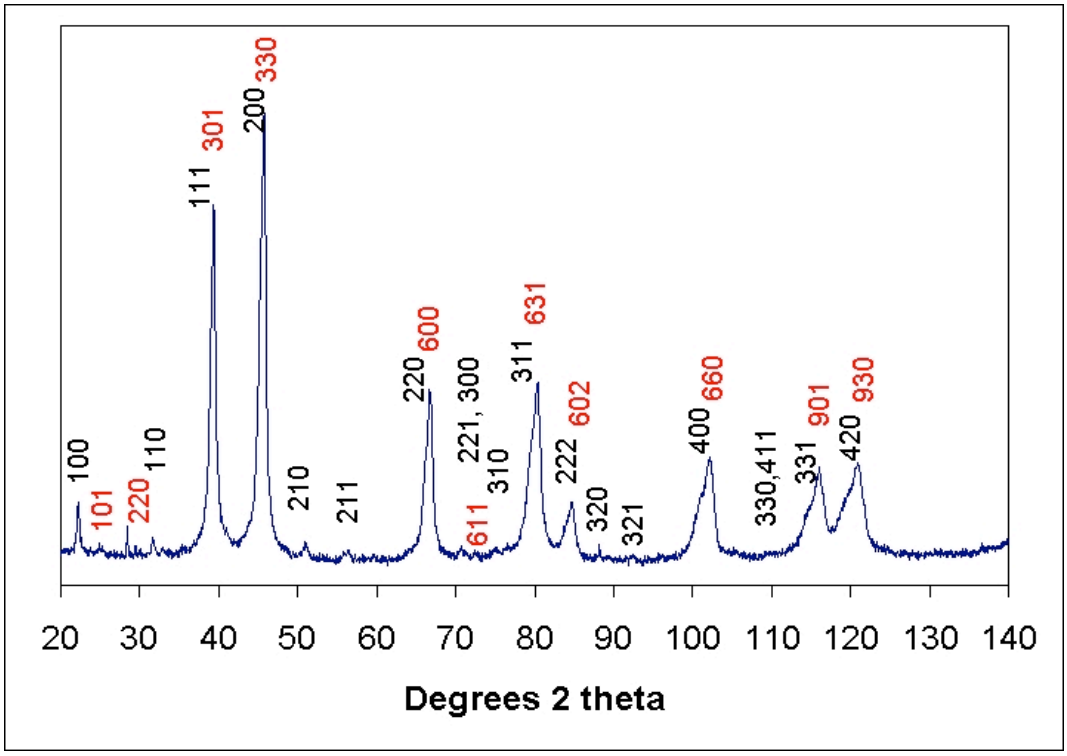

Figure 2.13 XRD pattern from nominal 15 %Zr heat-treated at 1000 °C, illustrating the presence of (Pt) and γ'. Red peak labels refer to the Pt_8Zr, and black to the γ'. The sharp peak at approximately 2θ = 28 ° is an artefact, resulting from the plasticine used to mount the sample on the stage.

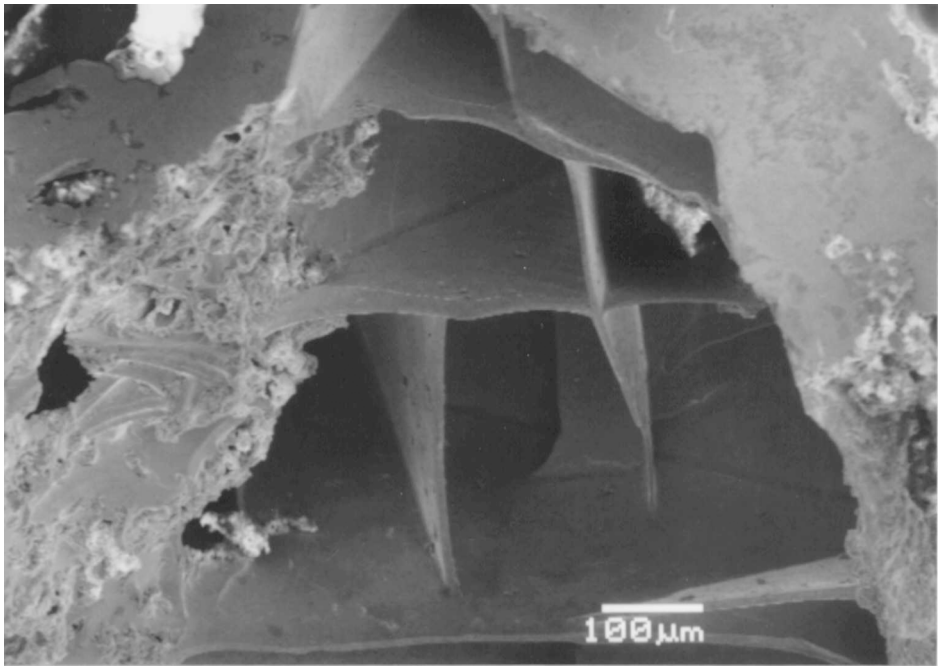

Figure 2.14 Cellular dendrites (11) observed growing into a pore of the as-cast nominal 19 %Zr alloy (SEM secondary electron image)

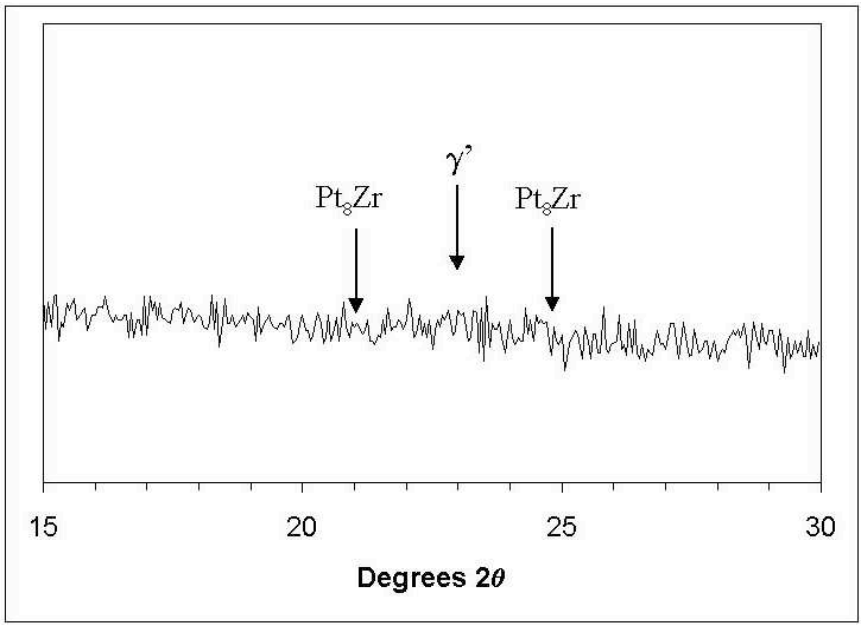

Figure 2.15 Low-2θ XRD pattern from nominal 15 %Zr heat-treated at 1300 °C. Any superlattice peaks from the Pt_8Zr would be present at the positions indicated by the arrows. The low volume fraction of γ' leads to the barely discernible peak at the position indicated.

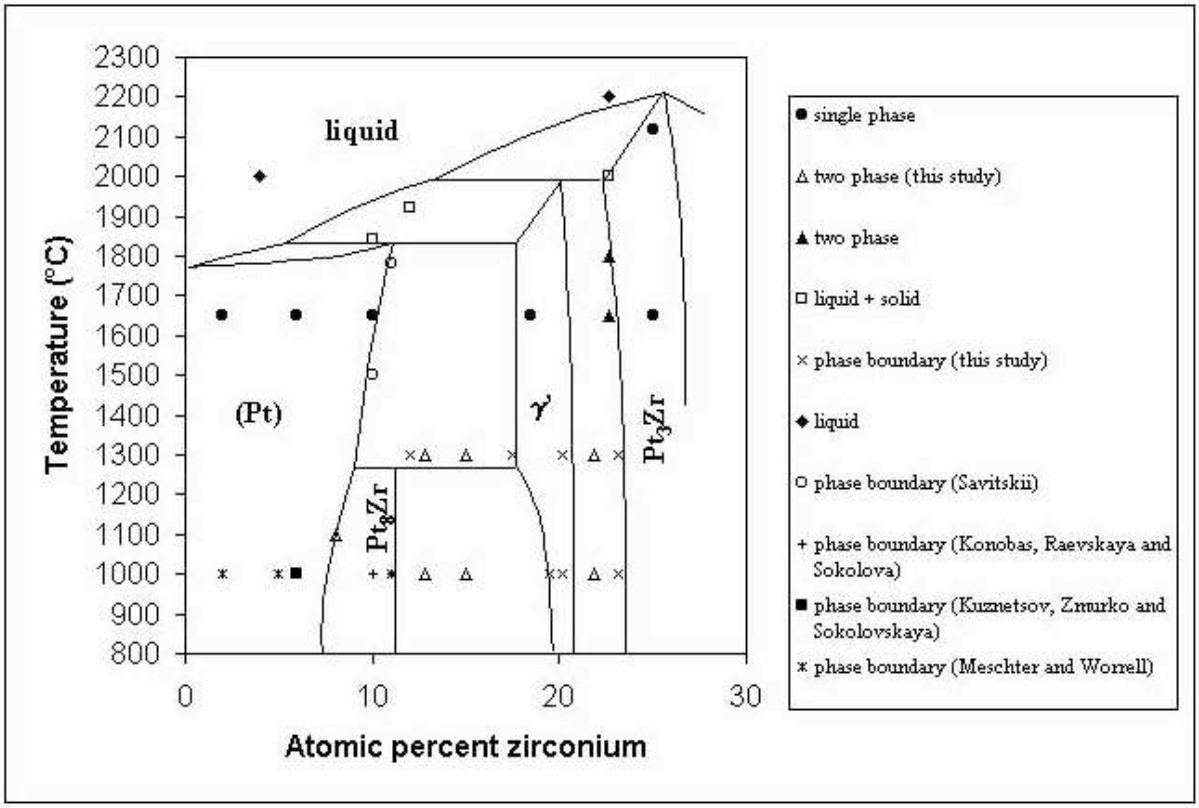

Figure 2.16 Modified construction of the Pt end of the Pt-Zr binary phase diagram, combining existing and new data.

Chapter 3 Phase Equilibria of Ternary Systems

In this chapter investigations into the phase equilibria of the three systems Pt - Rh - Hf, Pt - Rh - Zr and Pt - Ti - Cr will be described. These three systems were chosen for investigation based on the results for the Pt - Zr and Pt - Hf systems presented in chapter two, as well as on the basis of examination of the phase equilibrium literature.

The results presented in chapter two showed that stable two-phase γ - γ' cannot be produced within the Pt - Hf and Pt - Zr systems at room temperature, due to the existence of the low-temperature phases Pt_8Hf and Pt_8Zr respectively. The work described in this chapter aims to find an alloying addition which is able to suppress the formation of low temperature phases such that a two-phase microstructure of γ' dispersed in a γ matrix may be stabilised at room temperature. As a result, some heat treatment temperatures are slightly different, due to time constraints on equipment and the wish for equilibrium microstructures.

In addition to the above, another objective of this chapter is to describe the phase equilibria of the Pt - Ti - Cr system. This system was chosen on the basis of the above ideas, in that the Pt - Ti system exhibits a $L1_2$-structured phase at 25 %Ti, and a low-temperature phase Pt_8Ti, whereas the Pt - Cr system exhibits only a low-temperature $L1_2$-structured phase. If the Pt_3Ti and Pt_3Cr phase fields are connected, then addition of Cr to suitable Pt - Ti alloys should suppress formation of the low-temperature Pt_8Ti phase to yield a stable f.c.c. - $L1_2$ two-phase field.

All compositions quoted in this chapter are in atomic percent, unless otherwise stated.

3.1 Review of Previous Work

For the three ternary systems listed above, no ternary phase diagrams are in existence, and very little is known about alloys with more than a small amount of a third constituent. The only ternary systems where published data are available are the Pt - Rh - Zr and

Pt - Rh - Hf systems. For these systems the only known work is limited to oxide dispersion-strengthened (ODS) alloys, where small amounts of Zr or Hf are added to Pt and Pt - Rh alloys to allow internal oxidation, yielding a finely-dispersed oxide within the single-phase matrix. The amount of the Zr or Hf added is of the order of 1 wt%, and this alloy is still single-phase before internal oxidation [1,2].

The component binary systems, which form the sides of the ternary equilibrium diagrams, are reviewed below and are presented in figures 3.1 - 3.7. In the case of the Pt - Ti - Cr system, only two diagrams are reviewed (Pt - Ti and Pt - Cr) as the total additions are quite small (less than 25 % combined) and the phase equilibria in the Ti - Cr system will not affect the equilibria close to the Pt corner.

In the Pt - Rh binary system, the two elements form a continuous series of f.c.c. solid solutions across the entire composition range upon solidification. At lower temperatures a miscibility gap appears, existing between 10 %Rh and 95 %Rh at room temperature with a maximum temperature of approximately 760 °C at 50 %Rh, forming two f.c.c solid solutions at either end. These two f.c.c. phases probably result from the difference in lattice parameter between Rh and Pt [3].

The Pt - Zr binary equilibrium was examined in chapter 2. The phases observed below 25 %Zr are (Pt) (the Pt f.c.c. solid solution), Pt_8Zr (which dissociates below 1300 °C), γ' (which has the $L1_2$ crystal structure and exists over a small composition range between 16 %Zr and 21 %Zr), and Pt_3Zr (which has the hexagonal DO_{24} structure, and exists from 23 %Zr to above 25 %Zr). This is a modification from the published diagram (as in [3]).

The Pt - Hf binary equilibrium was also examined in chapter 2, and is very similar to that of the Pt - Zr system. The phases observed below 25 %Hf are (Pt) (the Pt f.c.c. solid solution), Pt_8Hf (which dissociates below 1300 °C), γ' ($L1_2$ crystal structure, existing over a small composition range between 17 and 20 %Hf) and Pt_3Hf (which has the hexagonal DO_{24} structure, and exists from 24 %Hf to above 25 %Hf). Partial phase diagrams of both the Pt-Hf and Pt-Zr systems can be found in chapter 2. The Pt-Hf diagram has not

previously been plotted, although, as discussed in chapter 2, Meschter and Worrell have published information regarding the phases present at 1000 °C up to 25 at%Hf [4].

In both the Rh - Zr and Rh - Hf systems, there are no intermediate phases between the f.c.c. phase (Rh) and the stoichiometric $L1_2$ phases Rh_3Zr and Rh_3Hf. As a result, it is possible to produce alloys with stable f.c.c. - $L1_2$ microstructures in both of these systems [5,6].

For the Pt - Ti - Cr system, no ternary phase diagram exists, and no previous work on the system has been found. The phase equilibria of both binary systems Pt - Ti and Pt - Cr have been characterised [7,8].

The Pt - Ti system exhibits two phases at low Ti concentration in addition to the Pt-based terminal solid solution. The tetragonal phase Pt_8Ti (which has a tetragonal structure based on the model system Au_4Zn_5) exists over the composition range 2 - 11 %Ti and dissociates in the region of 1080 °C. The cubic $L1_2$-structured phase Pt_3Ti exists between 19 %Ti and 25 % Ti at high temperature with solubility of Pt falling off slightly at lower temperature to 20 %Ti. This phase melts congruently at 1950 °C [7].

The Pt-rich end of the Pt - Cr system is not as well characterised as it is in the Pt - Ti system. Two phases are known to exist at or below 25 %Cr, which are the terminal f.c.c. solid solution based on Pt and the $L1_2$ phase Pt_3Cr. The $L1_2$ phase dissociates at approximately 1130 °C and as a result the f.c.c. phase (Pt) extends a long way across the diagram to approximately 30 %Cr, being the phase formed upon solidification for this whole composition range. An additional phase, CrPt, has been reported but also dissociates at low temperature. At low temperature the solubility limit of Cr in (Pt) is approximately 15 %Cr. The solidus temperature of the range of alloys between 0 %Cr and 25 %Cr is relatively constant, at between 1769 °C and 1785 °C [8].

The phases formed between Ti and Cr are unimportant for the purposes of this study, since the combined concentrations of these two elements in the alloys investigated are 25 % or less.

3.2 Experimental

As the purpose of this investigation was to identify two-phase f.c.c. - $L1_2$ fields and not to fully characterise the systems, only a few compositions were examined which were chosen to identify the extent of the two-phase field (if it was found to exist). In the Pt - Ti - Cr system, compositions were chosen to determine whether the Pt_3Cr and Pt_3Ti phase fields were connected. The compositions of the alloys prepared for the work in this chapter are given in table 3.1.

Table 3.1 Nominal compositions of ternary alloys (all figures in at%)

Pt	Rh	Zr	Hf	Ti	Cr
77	8	15			
62	15	23			
47	30	23			
77	10		13		
57	30		13		
82.5				5	12.5
80				7	13
82.5				10	7.5
80				10	10
80				15	5

The alloys were made by arc-melting from pure elements. Starting materials were Pt sponge (99.97 wt%), Rh sponge (99.95 wt%), Hf sponge (99.5 wt%, main impurity 0.3 %Zr), Zr wire (99.5+ wt%), Ti sponge (99.9 wt%) and Cr (99.99 wt%). These elements were weighed on an electronic balance, mixed together in appropriate proportions, pressed into pellets, and were arc-melted a number of times under Ar at a pressure of 0.8 - 0.9 atm. on a water-cooled copper hearth using a Ti getter prior to melting.

Samples for heat-treating were sealed in fused silica ampoules that had been evacuated and back-filled with Ar to remove most of the oxygen from the ampoule. The samples were then heat-treated in a chamber furnace. The times and temperatures selected were chosen to examine the temperature range within which current turbine materials operate, and are given in table 3.2. Due to the low diffusion rates exhibited by many elements in Pt, long heat treatments were required to approach an equilibrium microstructure.

Table 3.2 Heat treatments used in this chapter

Composition (in at%)	Temperatures and times
Pt - 8 Rh - 15Zr	1100 °C for 250 h
Pt - 15Rh - 23Zr	1000 °C for 250 h, 1300 °C for 50 h
Pt - 30Rh - 23Zr	1000 °C for 250 h, 1300 °C for 50 h
Pt - 10Rh - 13Hf	1100 °C for 165 h
Pt - 30Rh - 13Hf	1000 °C for 250 h, 1300 °C for 50 h
Pt - 5Ti - 12.5Cr	1000 °C for 250 h, 1300 °C for 50 h
Pt - 7Ti - 13Cr	1200 °C for 145 h
Pt - 10Ti - 7.5Cr	1000 °C for 250 h, 1300 °C for 50 h
Pt - 10Ti - 10Cr	1200 °C for 145 h
Pt - 15Ti - 5Cr	1200 °C for 145 h

After heat-treatment, samples were sectioned with a diamond cut-off wheel, mounted in conductive bakelite resin, and were prepared metallographically, with a final polish of 0.25 μm colloidal SiO_2. No etchants for optical microscopy are known for these alloys, so imaging was carried out in a scanning electron microscope (SEM).

Imaging (in compositional backscattered mode) and compositional analysis (standardless energy-dispersive spectroscopy) was conducted in a JEOL 5800LV SEM operating at 30 kV, after metallographic preparation to a colloidal silica final polish. As the average

atomic number of the phases in the alloys was quite similar the signal contrast was low, so image contrast was artificially increased and the final image was averaged over, typically, four frames. Some additional images were obtained using a CamScan S2 SEM typically operated at 20 – 30 kV in using compositional backscattered imaging mode.

Samples for TEM examination were prepared from some alloys. A 3 mm disk or smaller diameter slice was sectioned or punched from the bulk alloy and was thinned by mechanical grinding on SiC paper to a thickness of 100 μm before polishing on 6 μm and 1μm diamond pads. A spherical dimple was ground into one surface of the foil using a Gatan model 656 Dimple Grinder to give a thickness of 20 μm in the centre of the foil. Final thinning was achieved by ion thinning in a Gatan PIPS (Precision Ion Polishing System), with a typical schedule being 45 minutes at 5 kV gun voltage to achieve foil perforation followed by 30 minute polish at 2 kV to remove the damage from the previous ion polishing operation. Analysis of samples was carried out in a Philips CM30 TEM operating at 300 kV and a JEOL 200CX TEM operating at 200 kV.

Phase structure determination was conducted in a Philips XRD with CuK_{α} radiation, using a θ-2θ scan with a step size of 0.05 °, anode conditions of 40 kV and 40 mA and a step dwell time of approximately 10 s. Samples for XRD were cut from the heat-treated arc-melted ingot, plane ground on 1200 grade SiC paper and mounted on a rotating stage to improve counting statistics as the samples were polycrystalline rather than powdered.

Accurate lattice parameters were determined using Philips X'Pert profile fitting analysis software, which was capable of calculating lattice parameters accurate to four decimal places in some cases. A threshold for least squares averaging was set at 0.2 °2θ from calculated peak position, above which peak positions were discounted for the lattice parameter measurement. Automated corrections were performed for sample displacement and zero shift, and the measurement with the lowest χ^2 value (indicating the lowest error in the measurement) is the value quoted. All lattice parameter results are in the format *a=x.xxx (y)*, where the measurement *x.xxx* is in Å and *y* is the uncertainty in the final significant figure quoted by the analysis program.

3.3 Pt - Rh - Zr Results and Discussion

All composition and lattice parameter results are given in tables 3.3 - 3.6. The following discussion describes observations relating to the morphology and identification of the phases. Many as-cast phase compositions were not taken as solidification conditions were far from equilibrium and compositions were hence unlikely to be representative of those that would be obtained at or near equilibrium.

Table 3.3 Nominal versus actual compositions – Pt - Rh - Zr alloys

Nominal			**Actual**		
Pt	Rh	Zr	Pt	Rh	Zr
77	8	15	78.60	7.32	14.08
62	15	23	73.30	14.83	21.87
47	30	23	47.27	32.51	20.22

3.3.1 Nominal Pt – 8 %Rh – 15 %Zr samples

The as-cast material consisted of a small volume fraction (approximately 0.2) of irregular dendrites of a $L1_2$ phase (thought to be the Pt - Zr phase γ' identified in chapter 2) with a matrix of (Pt, Rh) f.c.c. solid solution. The latter phase was found to contain a reasonably high amount of Zr (12 %) whilst the γ' phase contained approximately 6 %Rh in addition to 19 %Zr. It is thought the dendrites are γ' and not Rh_3Zr due to the Zr and Rh content of the phase, the Zr level being within the region over which the γ' phase exists in the binary system. The prior dendrites can be seen in the heat-treated alloy in figure 3.8(b).

The heat treatment produced fine precipitation of γ' in the (Pt, Rh) matrix, as well as (Pt, Rh) precipitation in the former γ' dendrites (see figure 3.8(b)). These precipitates were quite small, on the order of 200 nm in diameter in both phases, and were aligned along particular crystallographic directions. Due possibly to overaging, some precipitates had

coalesced along these directions. The presence of precipitation in both the γ' and f.c.c. phases indicates that the solubility of Rh (and possibly Zr) in γ' reduces between the solidification temperature and 1100 °C, and that the Zr solubility in the f.c.c. (Pt, Rh) phase also falls over the same temperature range.

Table 3.4 Phase compositions and lattice parameters for nominal Pt - 8 %Rh - 15 %Zr samples

Temperature	Phase	Composition			Lattice Parameter (Å)
		Pt	Rh	Zr	
As-cast	f.c.c.	Bal.	7.37	11.83	3.960(3)
	γ'	Bal.	5.58	18.96	†
1100 °C	f.c.c.	Bal.	8.31	9.32	3.952 (2)
	γ'	Bal.	3.06	21.43	3.989 (3)

† Not enough peaks were present for accurate calculation of a lattice parameter

3.3.2 Nominal Pt - 15 %Rh - 23 %Zr Samples

The as-cast alloy (figure 3.8(a)) consisted of primary Rh_3Zr dendrites (approximately 90 % by volume) in a matrix of (Pt, Rh). Though the γ' and Rh_3Zr phases both have the $L1_2$ structure, the composition results show that the dendritic phase in this sample has a Zr content of close to 24 %, whereas in the previous alloy the Zr content was close to 19 %. Considering Rh_3Zr is approximately stoichiometric with only a few percent solubility either side of 25 %Zr, it is fair to assume that the observed dendritic phase is Rh_3Zr rather than γ' which exists up to 21 %Zr. These Rh_3Zr dendrites had very little side-branching and appeared to be heavily twinned (see figure 3.8(a)). The alternative situation is where the two phases Rh_3Zr and γ' are miscible, and the phase field bends considerably from being centred at approximately 20 %Zr in the binary Pt-Zr system to being centred at approximately 25 %Zr for a 10 %Rh addition. This latter situation would be rather unusual in a ternary alloy. The two phases Rh_3Zr and γ' have not been observed existing

separate from one another, though this no samples containing lower than 10 %Rh being investigated such that this may be clarified.

When heat-treated at 1000 °C (figure 3.8 (c)) the most obvious changes were in the inter-dendritic regions, which became two-phase mixtures of (Pt, Rh) and Rh_3Zr in most areas. In some of the inter-dendritic regions no precipitation was observed, which is presumably due to inhomogeneity in the alloy resulting from solidification.

After heat-treatment at 1300 °C, the microstructure was quite different to that at 1000 °C (see figure 3.8 (e)). Very little precipitation was evident in former inter-dendritic regions, and these regions had generally grown into the prior dendrites to yield a very irregular structure. The twinning observed in the dendrites was still evident after the heat treatment. The phase boundaries are not very distinct, as the BEI image is based on composition, though it appears the volume fraction of the (Pt, Rh) phase was greater than in the as-cast alloy.

Table 3.5 Phase compositions and lattice parameters for nominal Pt - 15 %Rh - 23 %Zr samples

Temperature	Phase	Composition			Lattice Parameter (Å)
		Pt	Rh	Zr	
As-cast	f.c.c.	No composition taken			-
1000 °C	f.c.c.	46.10	45.62	8.28	3.952 (2)
	γ'	64.55	11.60	23.85	3.989 (3)

3.3.3 Nominal Pt - 30 %Rh - 23 %Zr Samples

The as-cast alloy consisted of primary Rh_3Zr dendrites (approximately 90 % by volume) in a matrix of (Pt, Rh). A large amount of porosity is evident in the dendrites. The dendrites were thought to be Rh_3Zr rather than γ' due to the Zr content being almost 25 %, as discussed above in section 3.3.2.

After heat-treatment at 1000 °C (see figure 3.8 (d)) much of the porosity remained in the Rh_3Zr, and in the inter-dendritic regions fine Rh_3Zr precipitates had formed in the (Pt, Rh). The Rh_3Zr dendrites had developed a mottled appearance, which may be due to Rh or Zr diffusion to the regions where precipitation of Rh_3Zr had taken place.

After heat-treatment at 1300 °C (see figure 3.8 (f)) the microstructure was essentially similar to that at 1000 °C, with Rh_3Zr precipitates forming in the inter-dendritic regions. The main differences between the microstructure at 1300 °C and at 1000 °C were coalescence of the porosity into larger pores and coarser Rh_3Zr regions in the sample heat-treated at 1300 °C.

Table 3.6 Phase compositions and lattice parameters for nominal Pt - 30 %Rh - 23 %Zr samples

Temperature	Phase	Composition			Lattice Parameter (Å)
		Pt	Rh	Zr	
1000°C	f.c.c.	Bal.	74.11	3.69	3.831 (2)
	Rh_3Zr	Bal.	24.71	23.05	3.985 (3)
1300°C	f.c.c.	Bal.	67.67	3.78	3.875 (2)
	Rh_3Zr	Bal.	23.57	23.34	3.989 (2)

3.3.4 Pt - Rh - Zr Partial Ternary Phase Diagram

Using the above results some understanding of the Pt-rich corner of the Pt - Rh- Zr ternary phase equilibrium diagram can be gained. The alloys containing 15 %Rh and 30 %Rh both formed primary Rh_3Zr dendrites upon solidification, whereas the 8 %Rh alloy formed primary γ'. This shows that, if γ' and Rh_3Zr are not miscible and are separate phases, a three-phase field must lie between the tie-lines upon which these compositions sit. It also shows that the Rh_3Zr and γ' phase fields as not being joined, as the alternative situation requires a large deviation in the phase field around the Pt_3Zr phase

field to match the composition results. These results are plotted onto a ternary diagram as tie lines in figure 3.9 (a), and the likely configuration of phase fields is indicated on the same diagram re-plotted in figure 3.9 (b). This shows that extensive two-phase fields do exist in the Pt-rich corner of the Pt - Rh - Zr ternary system.

3.4 Pt - Rh - Hf Results and Discussion

All composition and lattice parameter results are given in tables 3.7 - 3.9. The following discussion describes observations relating to the morphology and identification of the phases.

Table 3.7 Nominal versus actual compositions for Pt - Rh - Hf alloys (at%)

Nominal			Actual		
Pt	Rh	Hf	Pt	Rh	Hf
77	10	13	78.09	9.24	12.67
57	30	13	59.07	30.60	10.33

3.4.1 Nominal Pt - 10 %Rh - 13 %Hf samples

The as-cast alloy was two-phase, consisting of dendrites of γ' in a matrix of (Pt, Rh). The XRD results showed that the as-cast alloy was two-phase, in contrast to the BEI image. No image is presented for the as-cast alloy as the backscattered electron detector was not sensitive enough to determine the difference between the two phases, and any image obtained appeared to be single-phase. The average atomic number difference between the two phases was very low ($\Delta Z = 0.24$), such that the atomic number difference between the two phases was beyond the limits of the BEI detector in the SEM (despite long collection times to maximise signal-to-noise ratio).

The sample equilibrated at 1100 °C exhibited approximately spherical precipitates of γ' in the f.c.c. matrix, as well as the γ' dendrites (see figure 3.10 (a)). The semi-coherent nature of these precipitates is evident from the dislocation networks present at the interface.

Table 3.8 Phase compositions and lattice parameters for nominal Pt - 10 %Rh - 13 %Hf samples

Temperature	Phase	Composition			Lattice Parameter (Å)
		Pt	Rh	Hf	
As-cast	f.c.c.	Bal.	10.01	11.41	3.955 (3)
	γ'	Bal.	8.21	17.24	3.991 (3)
1100 °C	f.c.c.	Bal.	10.14	10.88	3.958 (5)
	Pt_3Hf	Bal.	3.66	22.76	†

† Lattice parameter unable to be obtained due to weak reflections from Pt_3Hf

3.4.2 Nominal Pt - 30 %Rh - 13 %Hf Samples

The as-cast alloy consisted of an $L1_2$ phase (presumed to be Rh_3Hf) and (Pt, Rh). As for the Pt - 10 %Rh - 13 %Hf alloy above, a satisfactory as-cast image was unobtainable due to low contrast between the phases in the sample. The XRD results indicate that the volume percentage of the $L1_2$ phase was approximately 60 %.

The sample heated at 1000 °C for 250 h exhibited three phases (see figure 3.10 (b)), which is likely to be a result of incomplete precipitation. Two phases (an $L1_2$ phase and the (Pt, Rh) f.c.c. phase) formed a lamellar mixture similar in appearance to pearlite in steels. The volume fraction of the two phases appeared to be approximately equal, as the widths of the lamellae for each phase were approximately equal. The inter-lamellar spacing can only be accurately measured when the section plane is perpendicular to the plane of the lamellae, and so assuming the true lamellar thickness is the smallest measured, then the lamellar width is close to 300 nm. A third phase, which had average atomic number in between those of the two lamellar phases and was representative of the overall alloy

composition, existed as fairly large (50 – 100 μm) regions, into which the two-phase lamellar mixture appeared to be growing (figure 3.10 (b)).

After equilibration at 1300 °C the microstructure was very similar to that formed at 1000 °C, with two main differences (see figure 3.10 (c)). The first difference is that the third phase present above was not observed in this sample, and partly confirms the hypothesis above that the sample had not reached equilibrium. The second difference is the inter-lamellar spacing, which is approximately 1μm. The volume fractions were once again approximately equal, with XRD results indicating the volume fraction of Rh_3Hf as being 55 %. These results are consistent with the diffusion rates of the solute atoms being higher at 1300 °C than at 1000 °C, leading to full growth of the two lamellar phases and subsequent coarsening.

Table 3.9 Phase compositions and lattice parameters of nominal Pt - 30 %Rh - 13 %Hf samples

Temperature	Phase	Composition			Lattice Parameter (Å)
		Pt	Rh	Hf	
As-cast	f.c.c.	No compositions taken			3.915 (2)
	Rh_3Hf				3.968 (1)
1000 °C	f.c.c. †	Bal.	30.36	11.13	3.919(3)
	Rh_3Hf	Bal.	11.96	20.59	3.984(3)
	f.c.c.	Bal.	44.81	2.69	3.885(2)
1300 °C	f.c.c.	Bal.	11.22	24.80	3.977 (2)
	Rh_3Hf	Bal.	37.58	5.09	3.898 (3)

† Decomposing phase

3.4.3 Pt - Rh - Hf Partial Ternary Phase Diagram

The above results, while being few, still give an indication of the likely form of the isothermal sections of the ternary phase diagram at 1000 °C and 1300 °C. The likely form

is similar to that of the Pt - Rh - Zr system, in which the Rh_3Zr intermetallic appeared to exist for most of the way across the isothermal section along the 25 %Zr line. In this instance, the Rh_3Hf intermetallic is present in the as-cast and heat-treated Pt - 30 %Rh - 13%Hf and Pt - 10 %Rh - 13 %Hf alloys. The temperatures at which the Pt - 10%Rh - 13%Hf and Pt - 30%Rh - 13%Hf samples were heat treated are slightly different, but serve to give a useful indication of the likely phase equilibria in the region of 1000 – 1100 °C. The tie-lines based on the measured compositions are plotted on a ternary diagram in figure 3.11 (a), and a possible isothermal section at 1000 – 1100 °C based on the above results is presented in figure 3.11(b).

3.5 Pt - Ti - Cr Results and Discussion

The nominal and actual compositions of the Pt - Ti - Cr alloys produced are given in table 3.10. From this table it is apparent that some loss of Ti has occurred during melting of the two alloys containing 82.5 %Pt, while the other alloys are close to their nominal composition.

Table 3.10 Nominal versus actual compositions table for Pt - Ti - Cr alloys.

Nominal (at%)			Actual (at%)		
Pt	Ti	Cr	Pt	Ti	Cr
82.5	5	12.5	84.98	1.36	13.72
80	7	13	78.78	7.48	13.74
82.5	10	7.5	84.99	6.97	8.04
80	10	10	78.91	10.45	10.64
80	15	5	78.82	15.33	5.85

3.5.1 Nominal Pt - 10%Ti - 7.5%Cr and Pt - 5 %Ti - 12.5 %Cr Samples

All alloys with combined alloy additions of 17.5 % were single-phase f.c.c., both as-cast and after heat treatment at 1200 °C. After heat-treatment, samples consisted of large

polygonal grains with no evidence of a second phase. X-ray diffraction results confirmed that no second phase was present in amounts large enough to produce a detectable series of reflections in the XRD.

Table 3.11 Lattice parameters of the nominal Pt – 10 %Ti - 7.5 %Cr and Pt - 5 %Ti - 12.5 %Cr samples. As they are single-phase alloys the composition is the same at both temperatures, and is that quoted in table 3.10.

Temperature	Sample	Phase	Lattice Parameter (Å)
1000 °C	5Ti-12.5Cr	f.c.c.	3.902 (2)
	10Ti-7.5Cr	f.c.c.	3.911 (3)
1300 °C	5Ti-12.5Cr	f.c.c.	3.901 (1)
	10Ti-7.5Cr	f.c.c.	3.909 (2)

3.5.2 Nominal Pt - 7%Ti - 13%Cr Samples

The microstructure of the as-cast alloy was large polygonal grains of single-phase f.c.c. (Pt). No second phase was evident in the XRD pattern or in SEM-BE images of the alloy.

The sample contained two phases after equilibration at 1200 °C. No superlattice or second phase peaks were present in the XRD trace. Given the very small difference in composition between the two phases (see table 3.12) it is perhaps unsurprising that the lattice parameters are so similar. The two-phase mixture only existed in some regions of the sample, probably due to inhomogeneity, and had a similar appearance to a single-crystal Ni-base superalloy (see figure 3.12(c)). The precipitation of f.c.c had formed what appeared to be a matrix around zones of cuboidal $L1_2$ intermetallic. These $L1_2$ cuboids were approximately 700 nm in diameter. The lattice parameter obtained is thought to be

that of the $L1_2$ phase $Pt_3(Cr,Ti)$ given the large volume fraction of this $L1_2$ phase in the alloy.

Table 3.12 Phase compositions and lattice parameters of nominal Pt – 7 %Ti – 13 %Cr sample

Temperature	Phase	Composition			Lattice Parameter (Å)
		Pt	Ti	Cr	
1200 °C	$L1_2$	79.56	7.28	13.16	3.902 (3)
	f.c.c.	81.02	5.92	13.06	-

3.5.3 Nominal Pt - 10 %Ti - 10 %Cr Samples

The as-cast 10 %Ti - 10 %Cr alloy was single-phase both as-cast and after heat-treatment at 1200 °C. Unlike the previous alloy, no two-phase mixture was evident from either the XRD results or the SEM-BE images.

Table 3.13 Phase composition and lattice parameter of nominal Pt - 10 %Ti - 10 %Cr samples

Temperature	Composition			Lattice Parameter (Å)
	Pt	Ti	Cr	
1200 °C	78.91	10.45	10.64	3.903 (2)

3.5.4 Nominal Pt - 15 %Ti - 5 %Cr Samples

The as-cast alloy contained two phases, as shown in figure 3.12(b). The XRD results from this sample only show a single phase ($L1_2$), with some superlattice reflections present. These reflections were extremely weak, and their low intensity may be due to disorder in the phase, resulting in a low structure factor.

After equilibration at 1200 °C, the sample was single-phase $L1_2$ with no f.c.c. evident in the XRD trace or SEM-BE image.

Table 3.14 Phase composition and lattice parameter of nominal Pt – 15 %Ti – 5 %Cr samples

Temperature	Composition			Lattice Parameter (Å)
	Pt	Ti	Cr	
1200 °C	78.91	15.33	5.85	3.911(5)†

† Data was unreliable above 70 °2θ, leading to the relatively high error

3.5.5 Pt-Ti-Cr Partial Ternary Phase Diagram

The aim of this section of this chapter was to determine whether the Pt_3Cr and Pt_3Ti phase fields were connected, and whether a two-phase γ-γ' field existed within the ternary system. If such a two-phase field existed and the two intermetallics were miscible (i.e. connected), then the temperature range over which the two-phase field exists would be "tuneable" by adjusting the composition.

On the basis of the above results, it appears that the two intermetallics Pt_3Cr and Pt_3Ti are connected. The evidence for this is that the alloy series with 20 at% solute and heat-treated at 1200 °C pass from the f.c.c. + $L1_2$ two-phase field at 7 at%Ti into the Pt_3Ti ($L1_2$) phase field at 10 and 15 at%Ti. These results indicate that addition of Ti to Pt_3Cr increases its dissolution temperature, and that by adjusting the Cr-Ti balance the two-phase field temperature range can be selected. Such tuning is important in, for example, superalloys, in which the heat-treatment window and volume fraction of γ' at service temperature is adjusted via the solute element balance.

The two alloys with slightly lower solute levels were both f.c.c. at the heat-treatment temperature. This indicates the two-phase field is quite narrow, having a composition

range of less than 5 % solute (since this was the difference in composition between the first series of alloys and the second, which contained higher levels of alloying elements).

The Pt_8Ti intermetallic appears to have been suppressed to some extent by the addition of Cr. In the lower-solute series of compositions, the Pt_8Ti intermetallic was not identified after heat treatment at 1000 °C or 1300 °C. This result is unsurprising, given that there is no known analogous phase in the Pt-Cr system.

The presence of primary Pt_3Ti dendrites in the as-cast 15 at%Ti alloy indicates this phase melts congruently at this composition. At lower Ti levels there were no primary Pt_3Ti dendrites present, indicating that only one phase (f.c.c.) formed upon solidification.

The main feature of the Pt-rich corner of the Pt - Ti - Cr 1200 °C ternary equilibrium isothermal section is hence the extension of the Pt_3Ti phase into the diagram along the 25 % solute line, towards the compound Pt_3Cr. This phase field should appears to connect with the Pt_3Cr phase field, and should hence be termed the $Pt_3(Ti,Cr)$ phase field. This phase field is bordered by the f.c.c. (Pt) phase on the Pt-rich side, and is likely to be bordered it on the side furthest from the Pt corner as well. A tentative construction of the 1200 °C isothermal section is presented in figure 3.13(b).

3.6 Conclusions

In this chapter the ternary phase equilibria of three systems were investigated. For each system a tentative partial equilibrium phase diagram was plotted, and composition, phase structure and lattice parameter results were obtained.

Two-phase (f.c.c. - $L1_2$) fields were identified in all systems, which raises the possibility of producing superalloy analogues from each system. Promising microstructures were identified in the Pt - Rh - Hf and Pt - Ti - Cr systems, in which precipitates of the $L1_2$ intermetallic phase were present in the (Pt) f.c.c. phase.

3.7 References

1. E. P. Daneliya, M. I. Doperchuk and G. I. Kandyba, Metal Science and Heat Transfer, **30** 311 (1998).
2. E. P. Daneliya, M. I. Doperchuk and G. I. Kandyba, Russian Metallurgy, **4** 176 (1989).
3. Binary Alloy Phase Diagrams, 2nd Edition, Volume 3, Ed.-in-Chief T.B. Massalski, ASM International, Materials Park (1990), p. 3122
4. P. J. Meschter and W. L. Worrell, Met. Trans. **8A** 503 (1977).
5. Binary Alloy Phase Diagrams, 2nd Edition, Volume 3, Ed.-in-Chief T.B. Massalski, ASM International, Materials Park (1990), p. 3249
6. Ibid., p. 2107
7. Ibid., p. 3142
8. Binary Alloy Phase Diagrams, 2nd Edition, Volume 2, Ed.-in-Chief T.B. Massalski, ASM International, Materials Park (1990), p. 1315

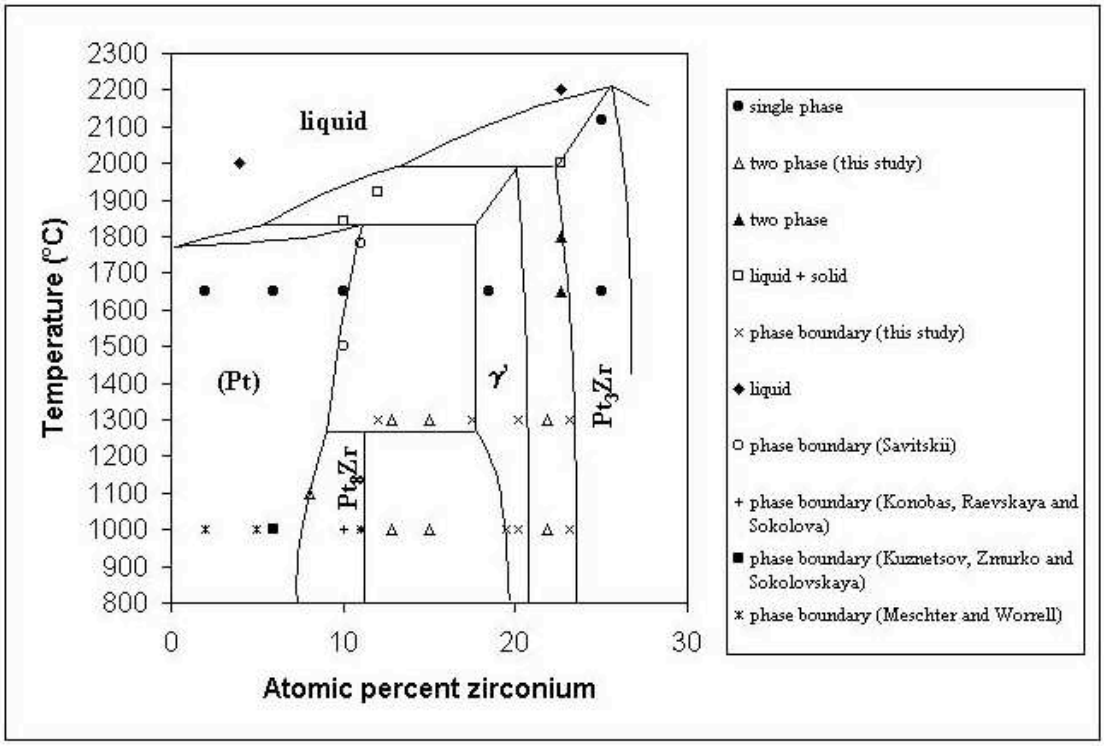

Figure 3.1 The Pt - Zr binary phase diagram, as modified in chapter 2 of this thesis. The main features are the series of intermetallic compounds Pt_8Zr, γ' and Pt_3Zr, and the cascading peritectic reactions.

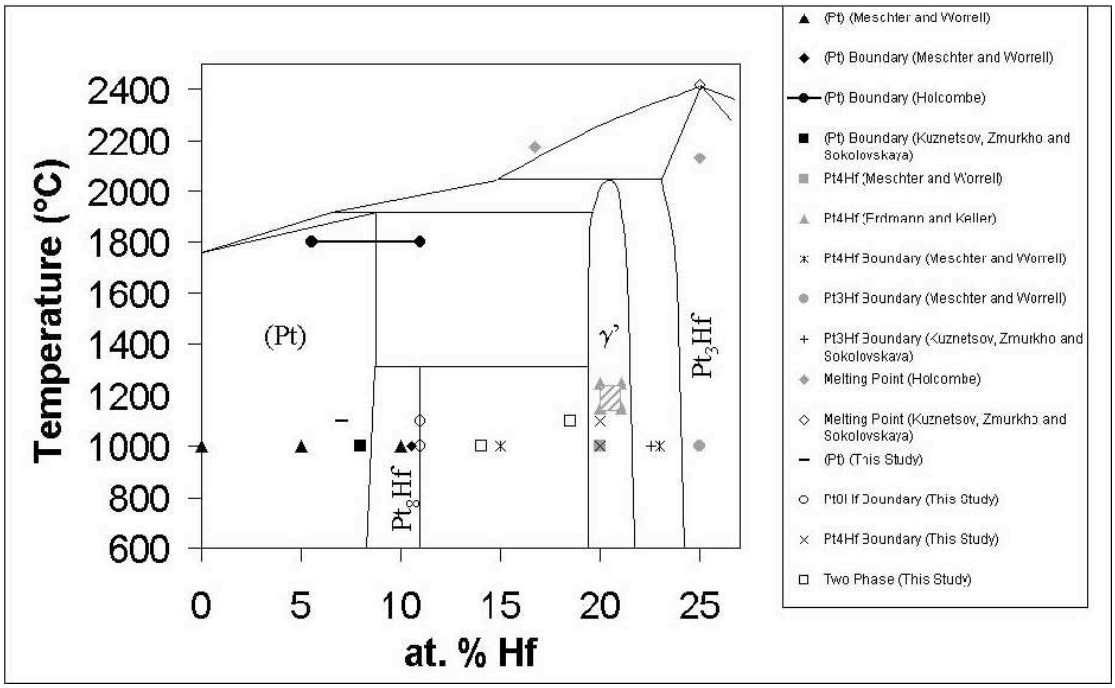

Figure 3.2 The Pt - Hf binary phase diagram, as modified in chapter 2 of this thesis. The main features are the series of intermetallic compounds Pt_8Hf, γ' and Pt_3Hf, and the cascading peritectic reactions.

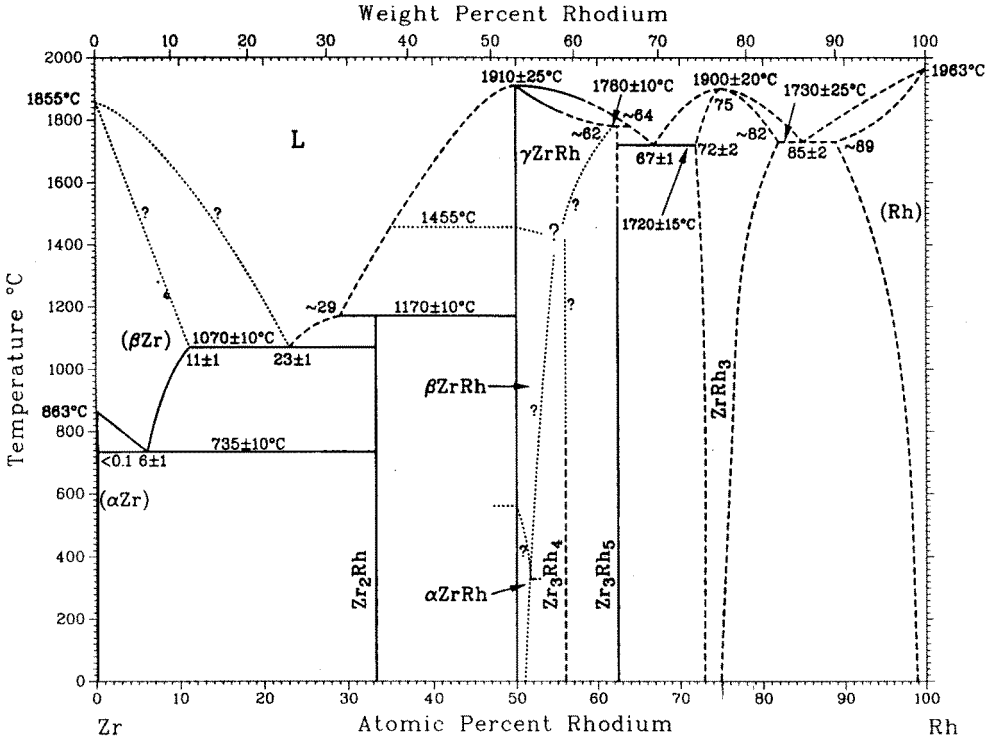

Figure 3.3 The published Rh - Zr binary phase diagram. No compounds occur between (Rh) and Rh_3Zr, and a two-phase (Rh) + Rh_3Zr field exists.

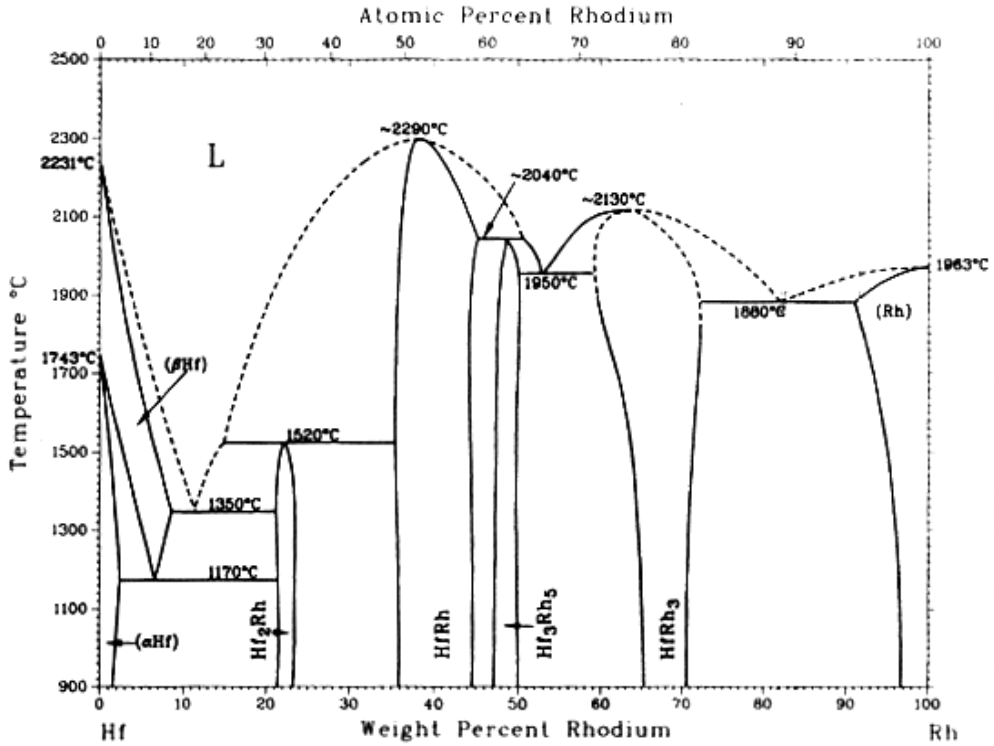

Figure 3.4 The published Rh - Hf binary phase diagram. No intermetallic compounds exist between (Rh) and Rh_3Hf, and a two-phase (Rh) + Rh_3Hf field exists.

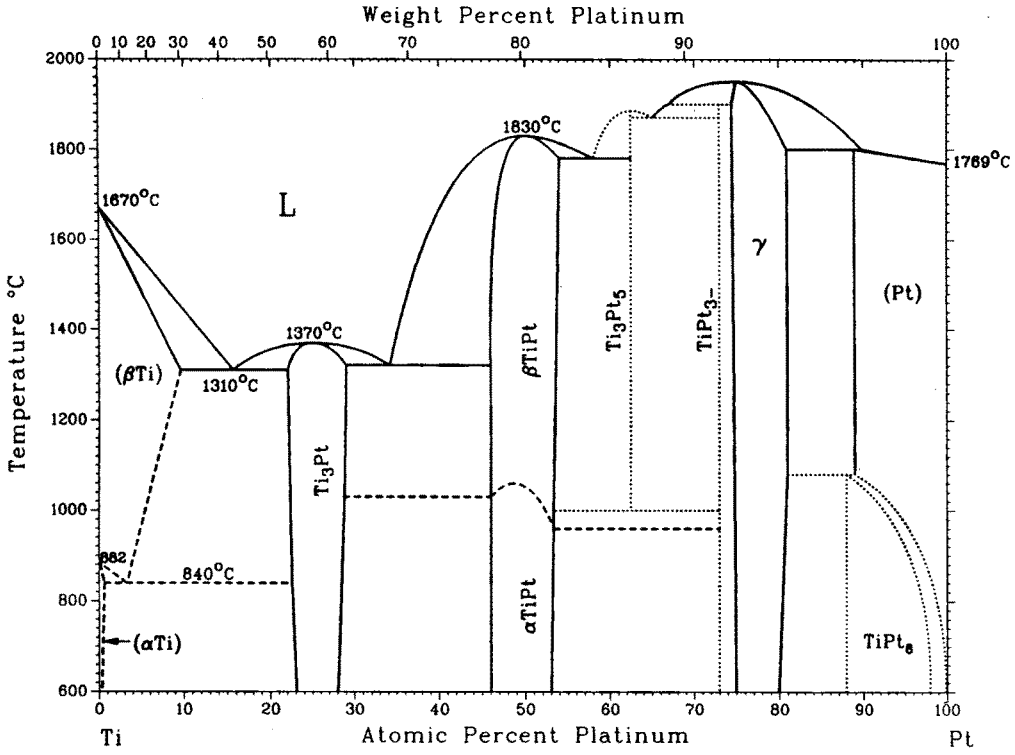

Figure 3.5 The published Pt - Ti binary phase diagram. The low-temperature phase $TiPt_8$ precludes the possibility of producing a viable (Pt) - γ' alloy.

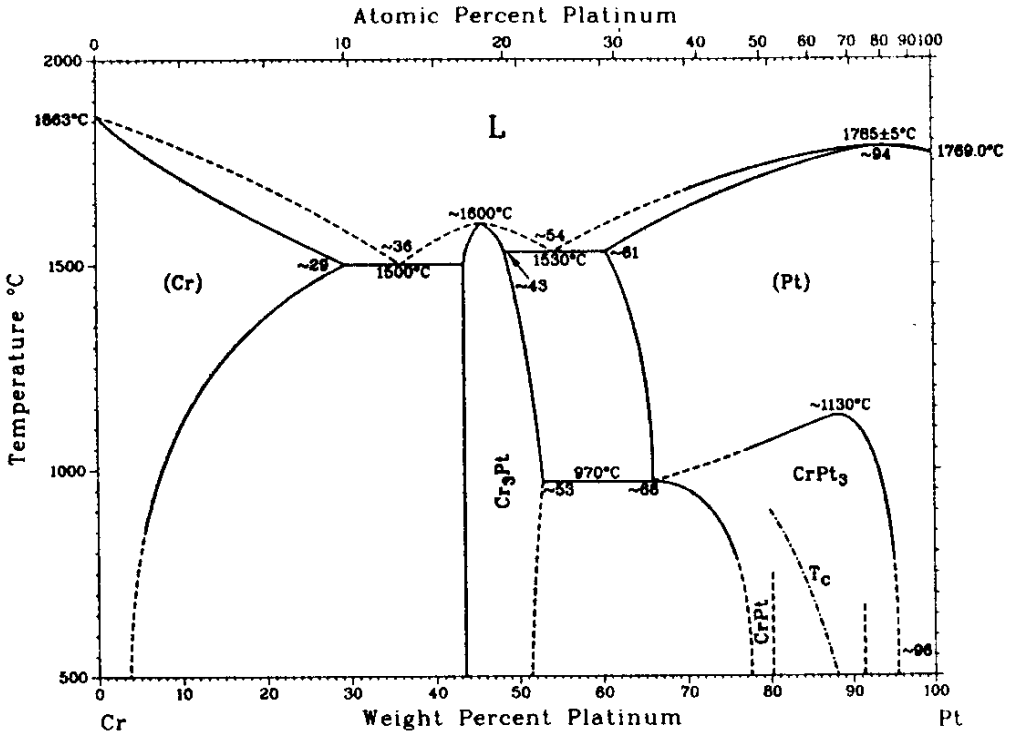

Figure 3.6 The published Pt - Cr binary phase diagram. The phase $CrPt_3$ dissociates well below its melting temperature, leading to an extended (Pt) phase field.

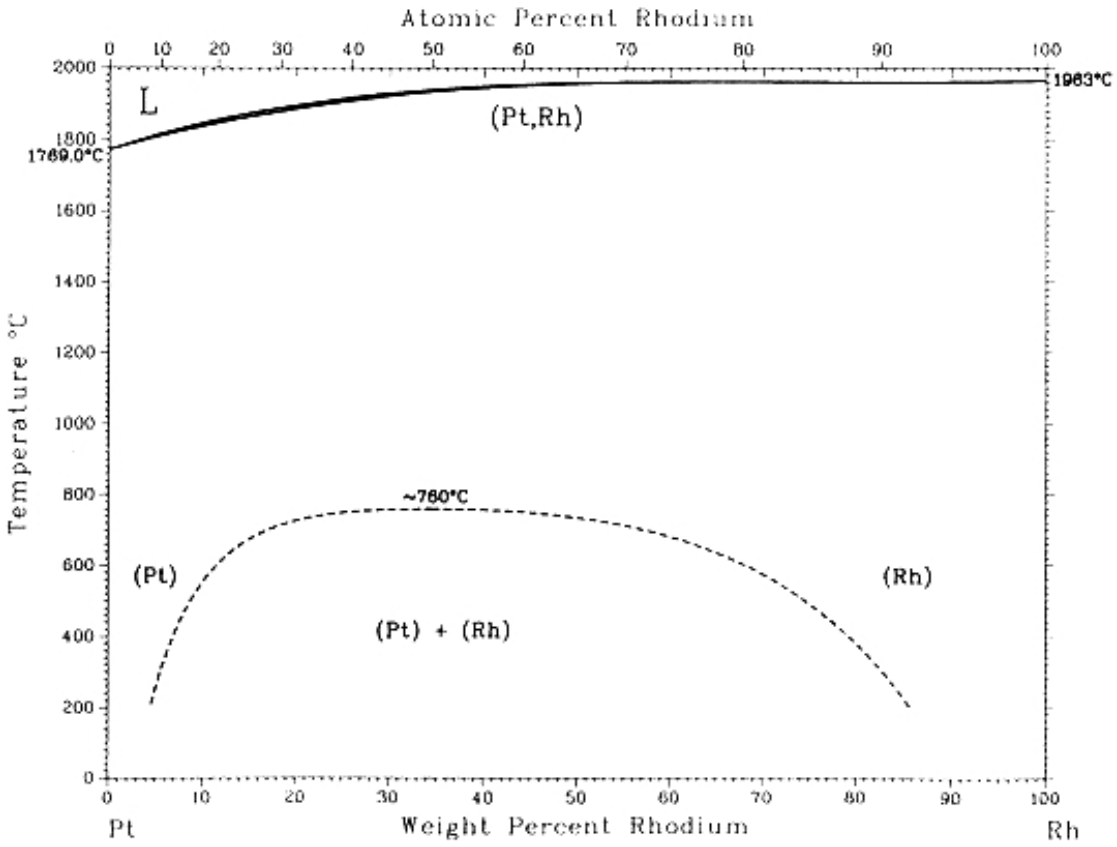

Figure 3.7 The published Pt - Rh binary phase diagram. The two elements form a compete series of solid solutions, apart from below about 760 °C where a miscibility gap exists and two f.c.c. solid solutions are formed.

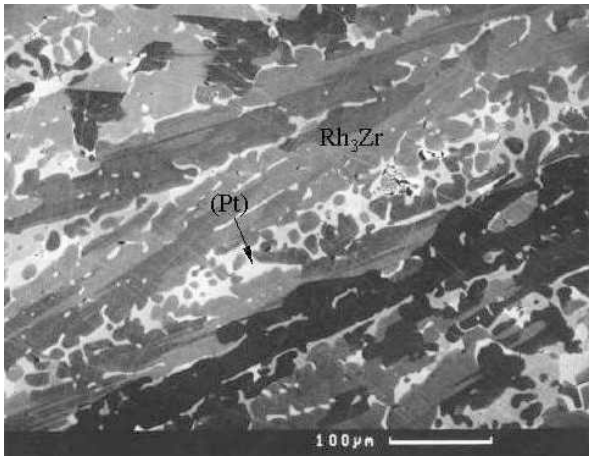

(a)

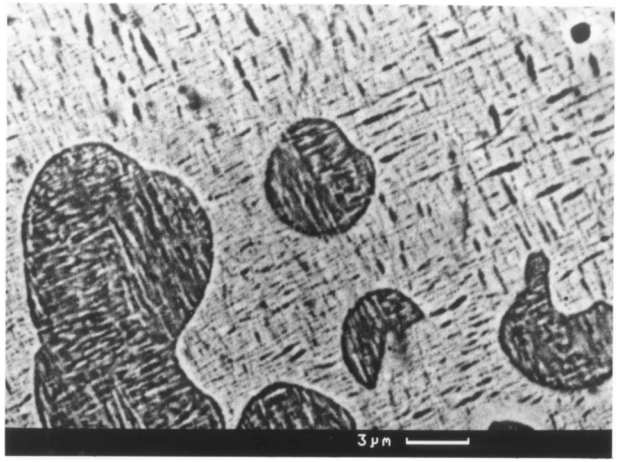

(b)

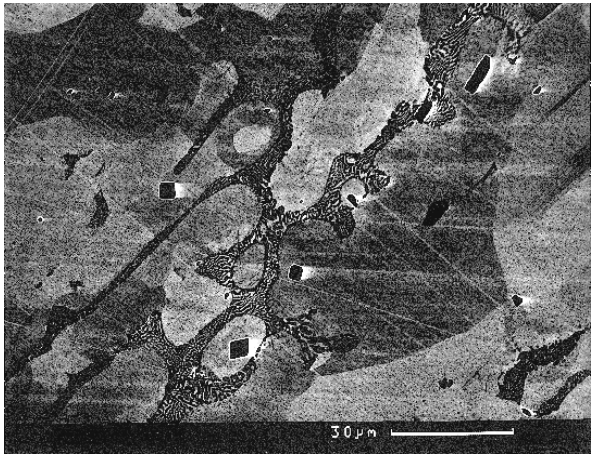

(c)

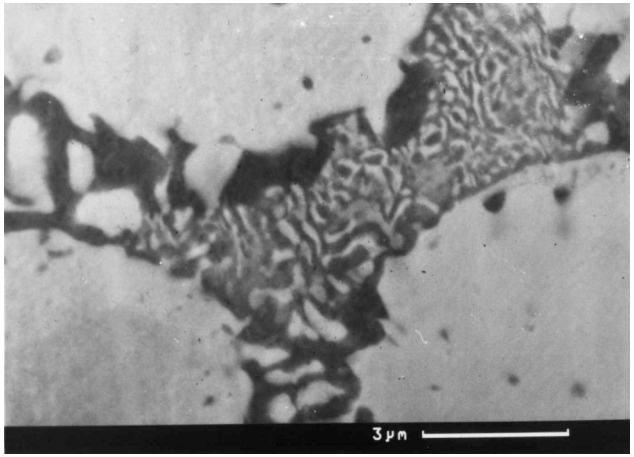

(d)

Figure 3.8 - caption on page 116

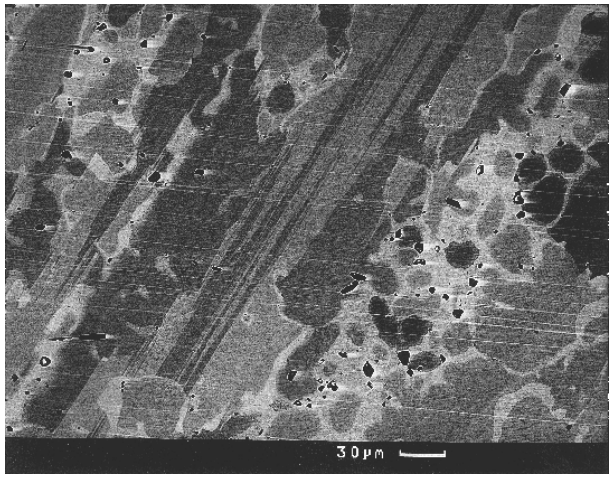

(e)

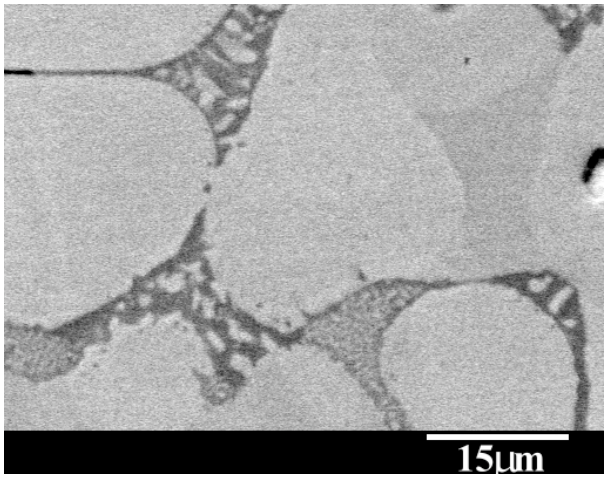

(f)

Figure 3.8 Microstructures of Pt - Rh - Zr alloys:
a) Pt - 15 %Rh - 23 %Zr as-cast - dendrites of twinned Rh_3Zr in a matrix of (Pt);
b) Pt – 8 %Rh – 15 %Zr after heat-treatment at 1100 °C - precipitated of γ' in a matrix of (Pt) and precipitates of (Pt) in former γ' dendrites;
c) Pt – 15 %Rh – 23 %Zr after heat-treatment at 1000 °C - former dendrites of RhZr with inter-dendritic Rh_3Zr and (Pt);
d) Pt – 30 %Rh – 23 %Zr after heat-treatment at 1000 °C - former dendrites of RhZr with inter-dendritic Rh_3Zr and (Pt);
e) Pt – 15 %Rh – 23 %Zr after heat-treatment at 1300 °C - former Rh_3Zr dendrites with substantial growth of (Pt) and regions of Rh_3Zr;
f) Pt – 30 %Rh – 23 %Zr after heat-treatment at 1300 °C - former dendrites of RhZr with inter-dendritic Rh_3Zr and (Pt).

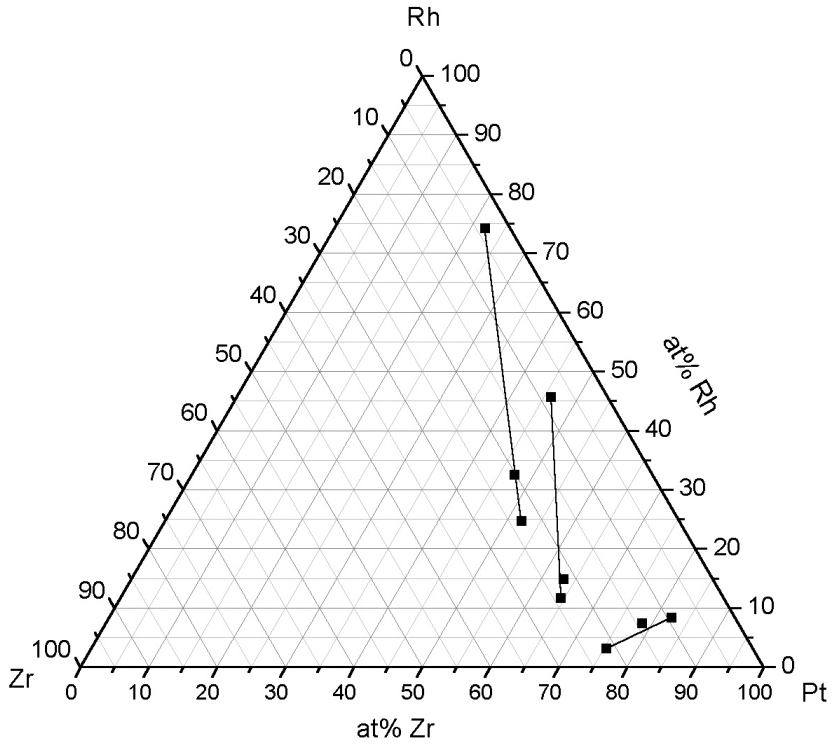

(a)

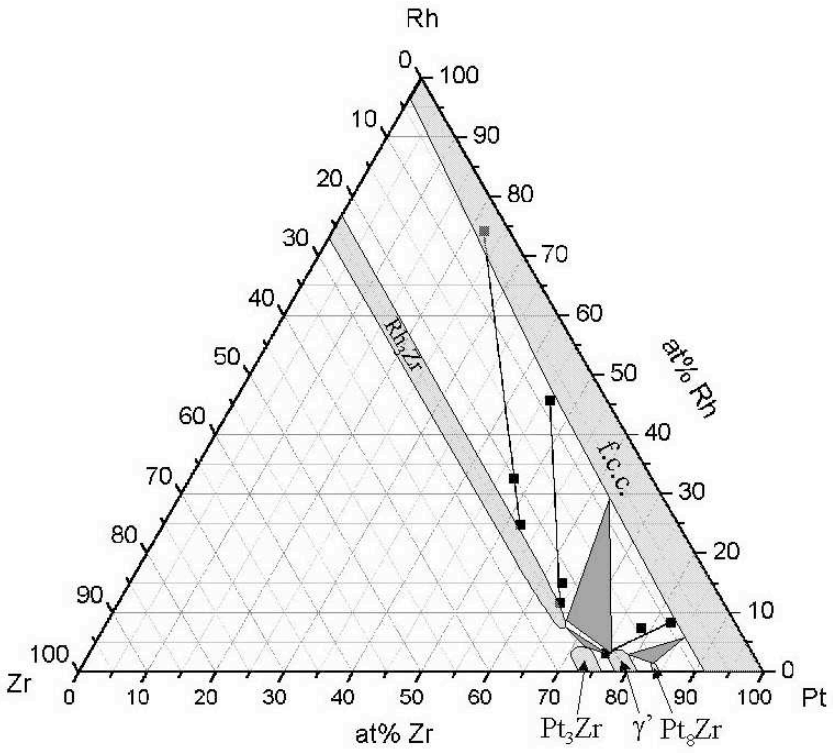

(b)

Figure 3.9 (a) Tie-lines in the Pt - Rh - Zr ternary system at 1000 °C and 1100°C. The central point on each line is the overall alloy composition; (b) Possible partial construction of the 1000 °C – 1100 °C isothermal section of the Pt-Rh-Zr ternary phase diagram based on the tie lines in (a) and the known form of the Pt-Zr binary phase equilibrium diagram.

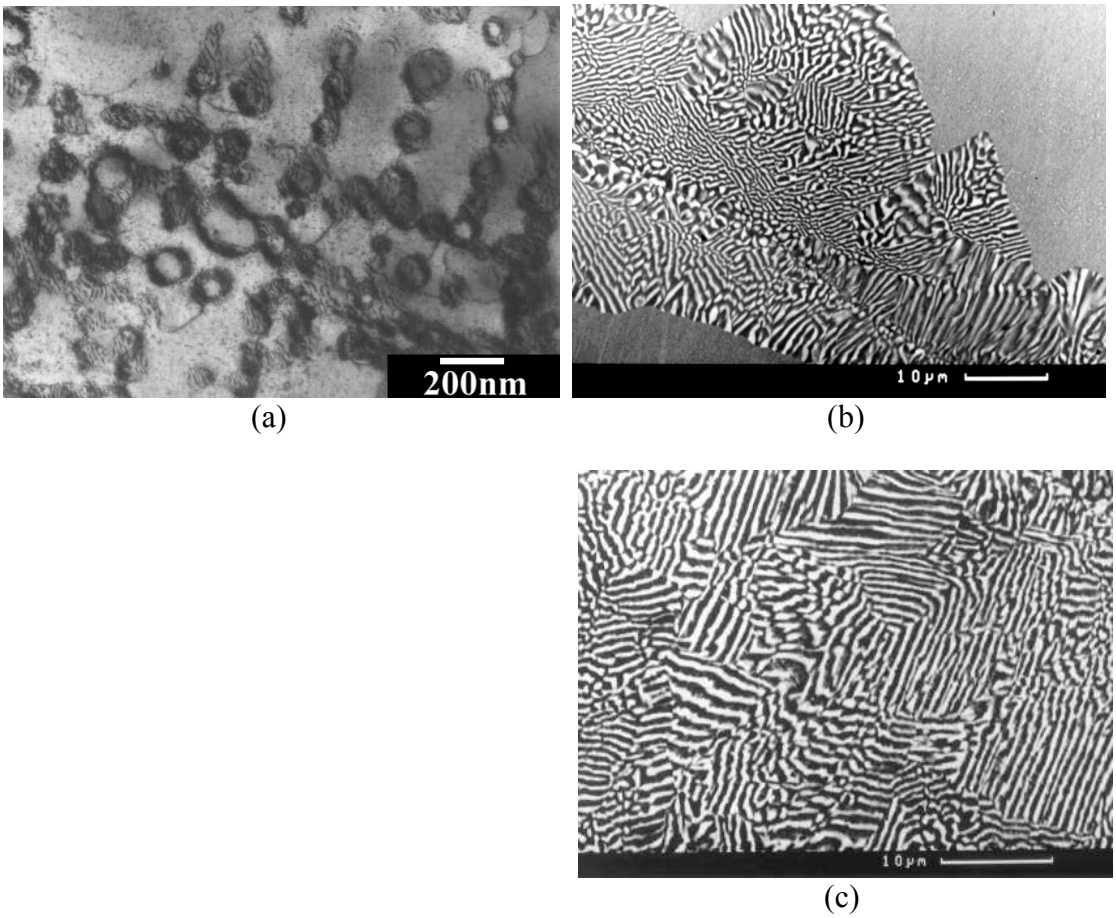

(a) (b)

(c)

Figure 3.10 Microstructures of Pt - Rh - Hf alloys:
a) Pt - 10 %Rh - 13 %Hf after heat-treatment at 1100 °C - precipitates of Rh_3Hf in a matrix of (Pt). Former dendrites of Rh_3Hf were also present, but are not shown in this diagram;
b) Pt - 30 %Rh - 13 %Hf after heat-treatment at 1000 °C - lamellae of (Pt,Rh) (dark) and Rh_3Hf (light) growing into a decomposing single-phase f.c.c. region (grey);
c) Pt - 30 %Rh - 13 %Hf after heat-treatment at 1300 °C - lamellae of Rh_3Hf (light) and (Pt,Rh) (dark).

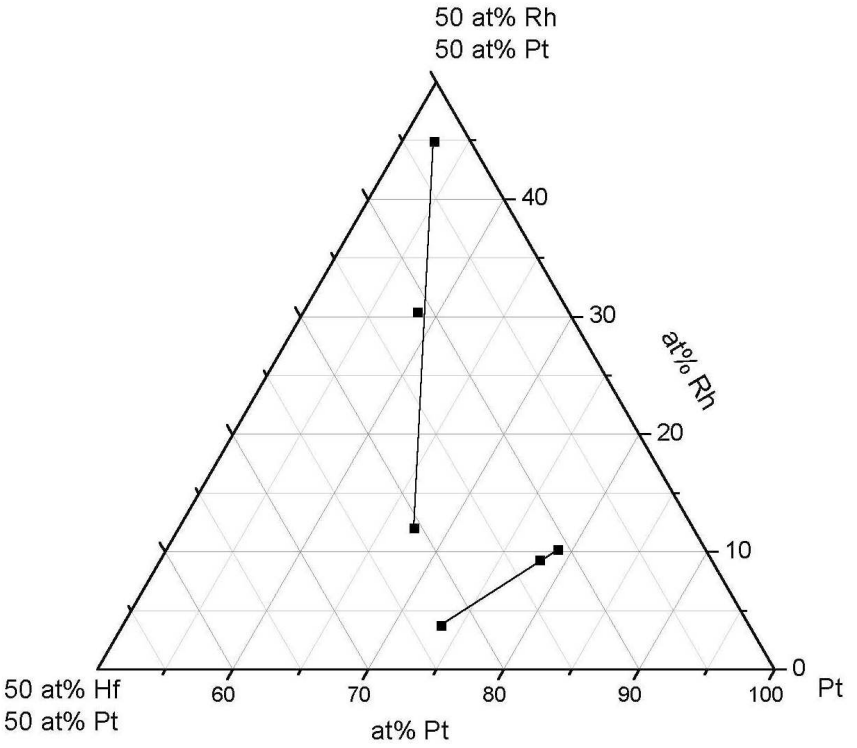

(a)

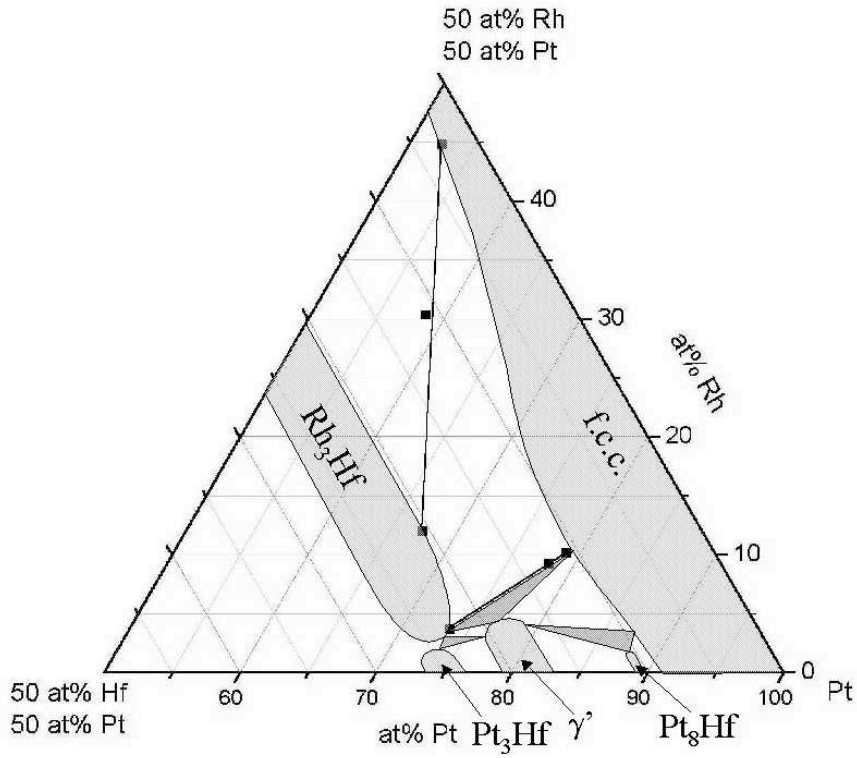

(b)

Figure 3.11 (a) Tie-lines in the Pt-Rh-Hf ternary system at 1000 °C – 1100 °C. The central point on each line represents the overall alloy composition; (b) Possible partial construction of the 1000 °C – 1100 °C isothermal section of the Pt-Rh-Hf ternary phase diagram based on the tie-lines in (a) and the known form of the Pt-Hf binary phase equilibrium diagram.

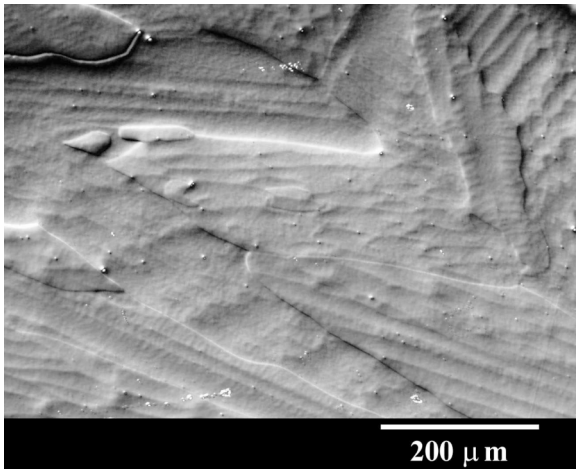

(a)

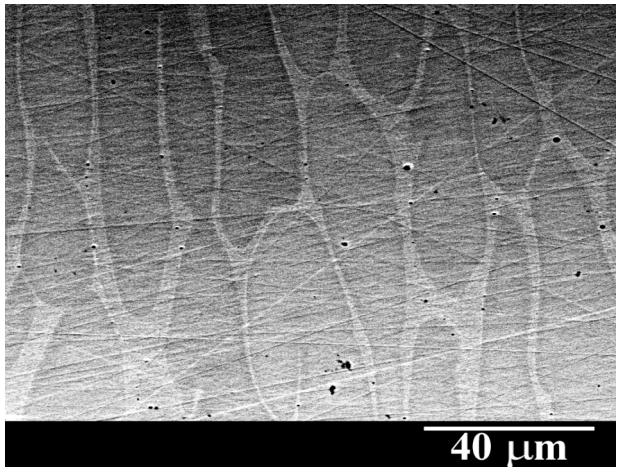

(b)

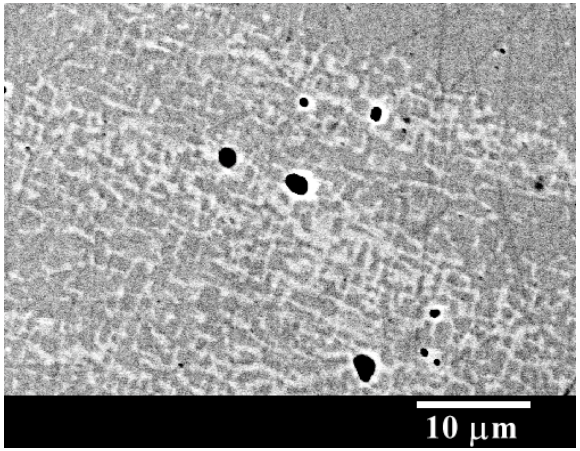

(c)

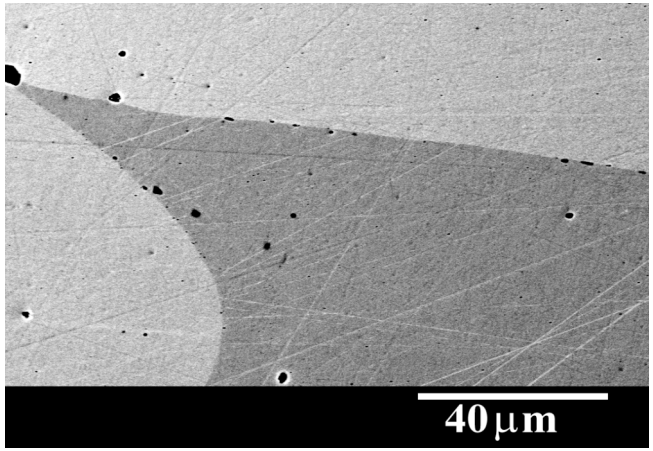

(d)

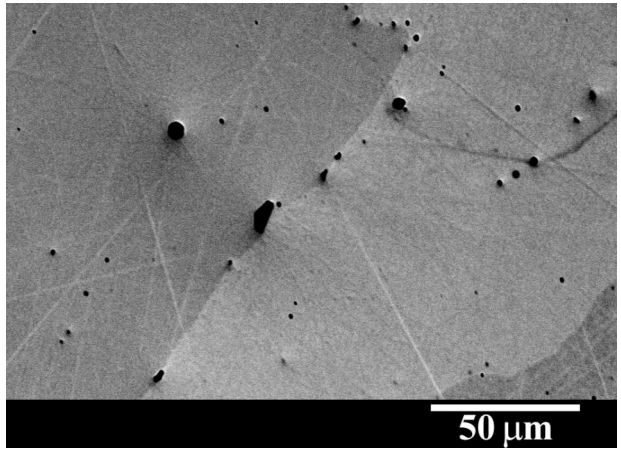

(e)

Figure 3.12 - caption on page 121

Figure 3.12 Pt - Ti - Cr microstructures:
(a) Pt - 7at%Ti - 13 at%Cr as-cast (Nomarski interference contrast) - dendrites of (Pt);
(b) Pt - 15at%Ti - 13 at%Cr as-cast - dendrites of Pt_3(Ti,Cr) in a matrix of (Pt);
(c) Pt - 7at%Ti - 13 at%Cr after heat treatment at 1200 °C - regions of a two-phase mixture of precipitated f.c.c. and Pt_3(Ti,Cr). The remainder of the sample was Pt_3(Ti,Cr);
(d) Pt - 10at%Ti - 10 at%Cr after heat treatment at 1200 °C - polygonal grains of single-phase Pt_3(Ti,Cr);
(e) Pt - 15at%Ti - 13 at%Cr after heat treatment at 1200 °C - polygonal grains of single-phase Pt_3(Ti,Cr).

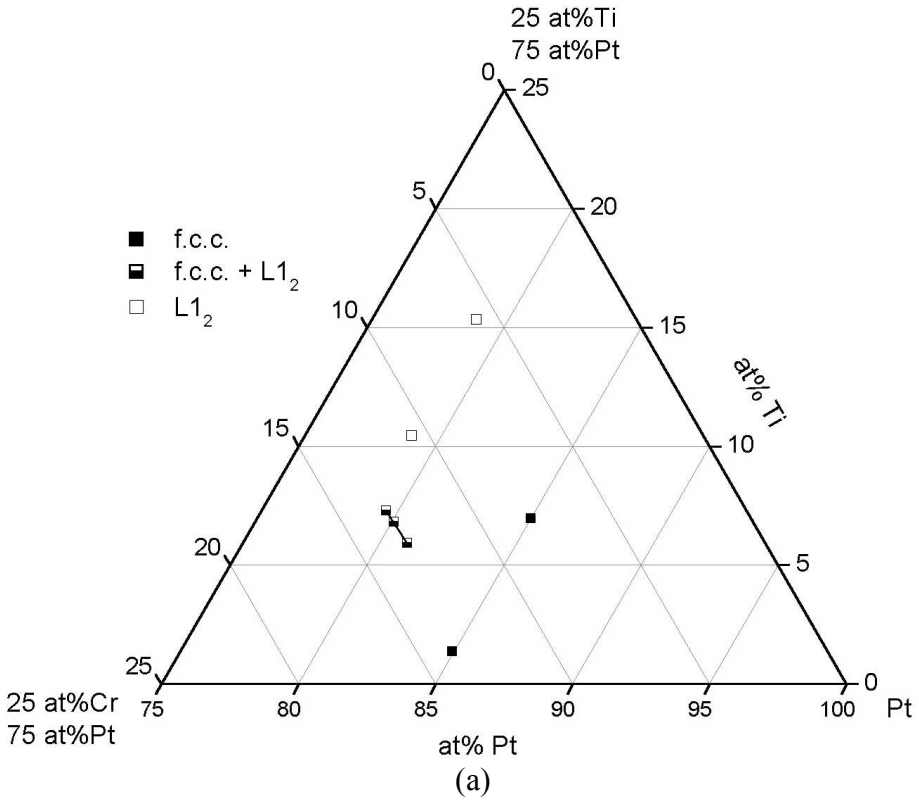

(a)

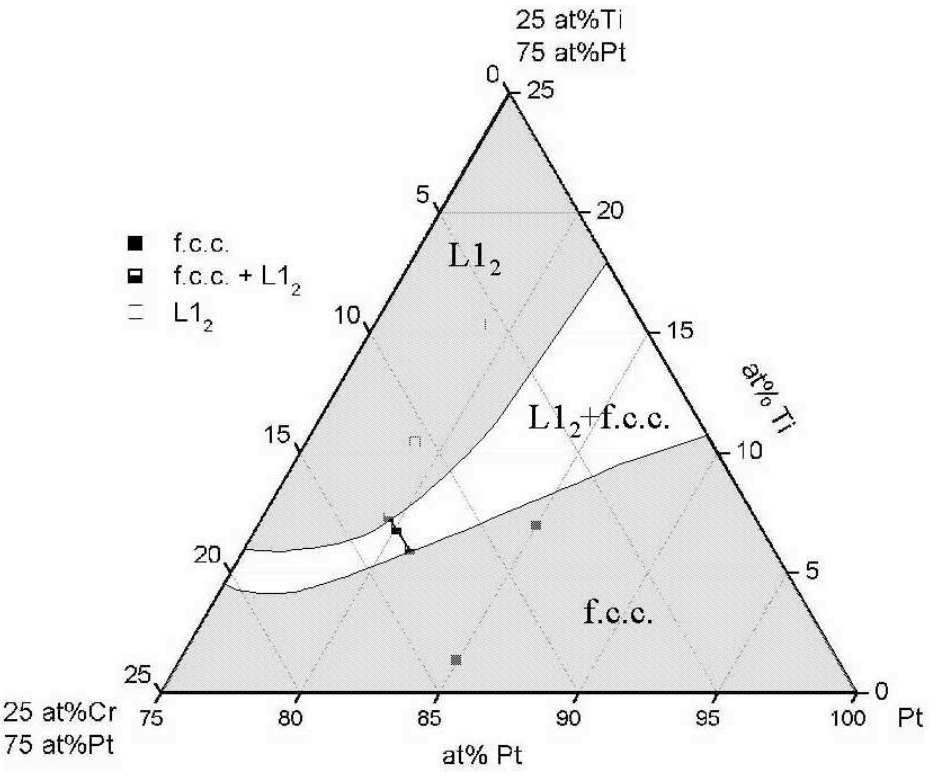

(b)

Figure 3.13 (a) Compositions and associated microstructures at 1200 °C in the Pt - Ti - Cr ternary system, with the tie line for the two-phase sample; (b) Possible partial construction of the 1200 °C isothermal section of the Pt - Ti - Cr ternary phase diagram.

Chapter 4 Mechanical Properties of Pt-Based f.c.c. - $L1_2$ Alloys

As seen in chapter 1, in recent years there has been a great deal of interest in PGM-based two-phase alloys, including those that mimic the microstructure of the nickel-base superalloys. Such alloys have been shown to possess exceptional strength and creep resistance at temperatures up to 1800 °C, due to their high melting point and microstructure consisting of small $L1_2$ precipitates in a fcc matrix. This chapter describes the mechanical properties and microstructure of two Pt-based f.c.c. - $L1_2$ alloys, which were selected based on the results presented in chapter 3.

4.1 Review of Previous Work

Wee, Noguchi, Oya and Suzuki first reported the high strength and temperature dependence of strength of Pt-based $L1_2$ intermetallics in a series of publications beginning in 1979 [1-3]. Hot hardness tests were conducted on many Pt-based alloys including Pt_3Cr, Pt_3Ti, Pd_4Ti, Pt_3Al and Pt_4Hf. Their work showed the high hardness of many Pt-based $L1_2$ phases, which for the phases Pt_4Hf and Pt_3Ti was much higher than Ni_3Al at all temperatures (see figure 4.1).

One patent has been found in the area of two-phase Pt-based alloys (disregarding oxide dispersion-strengthened alloys), which was filed by G. L. Selman of Johnson Matthey in 1971 [4]. This patent describes the "dispersion strengthening" of alloys based on Pt, Pd and Rh by adding up to 20 at% of one or more of the lanthanides, Sc, Ti, V, Y, Zr, Nb, Hf and Ta. The strengthening effect of the precipitates is only illustrated for trace additions (< 0.1 %Zr or Ti in Pt – 25 %Rh). This method of dispersion strengthening is distinct from the interfacial strengthening observed in a superalloy. In *dispersion-strengthened* alloys the second phase particles are small and well-spaced, causing dislocations to bow (Orowan bowing) under increased stress to pass and leave a dislocation loop around the particle. In *interfacial strengthening* the precipitate phase takes up to about 65 % of the volume of the alloy, so the dislocations must attempt to pass through the precipitates if they are to propagate. The precipitates are semi- or fully coherent, so that there may be a strain field

at the interface if the misfit is slightly positive or negative. As the precipitate is ordered, passage of a dislocation must create an anti-phase boundary on the slip plane, which in some cases is energetically unfavourable, as described in an earlier chapter (see section 1.2.2), and the stress required to force a dislocation through the precipitate will be higher than through the matrix. In Selman's patent it is likely to have been a coincidence that the choice of the upper concentration limit was 20 % (which would make many of the alloy systems above *interfacially strengthened*), and may have been prompted by the high solubility of Ti in the f.c.c. phase (Pt).

Harada and co-workers at NIMS in Japan, who first invented the concept of a "refractory superalloy", have patented these alloys [5], in which they claim a range of compositions based on Ir and Rh. It is likely there is some overlap between their patent and that of Selman.

The results of Hill and co-workers [6-10], as part of a collaborative program with the Department of Materials Science and Metallurgy, University of Cambridge, have shown that Pt-based alloys can be produced which possess the desired microstructure (figure 4.2). The alloys are based on the precipitates Pt_3Al and Pt_3Ti, with various solid-solution strengthening elements such as Re, Ru, Cr and Ni. Of the tested alloys the most promising for oxidising environments were those containing large amounts of Al (about 14 at%), as these formed an adherent alumina scale on their surface (figure 4.3). The mechanical properties were found to be at least equivalent to PM2000 (an oxide dispersion-strengthened Fe-base alloy considered to have excellent high-temperature strength and oxidation resistance) at temperatures up to 1200 °C, above which no data was presented for the PM2000. Some of the mechanical property results for the above alloys are shown in figures 4.4 and 4.5.

4.2 Experimental

The alloys chosen for testing were based on results presented in chapter 3, in which two-phase f.c.c. - $L1_2$ regions were observed in several ternary systems. Alloys were not

produced in all ternary systems in which a two-phase region existed, as in a preliminary oxidation test the oxidation behaviour of the Pt - Rh - Zr system was found to be very poor compared to the Pt - Rh - Hf system (see figures 4.6 and 4.7). Alloys for mechanical testing were hence produced in the Pt - Rh - Hf and Pt - Ti - Cr systems.

The alloys were made by arc-melting from pure elements. Starting materials were Pt sponge (99.97 wt%), Rh sponge (99.95 wt%), Hf sponge (99.5 wt%, main impurity 0.3 wt%Zr), Ti sponge (99.9 wt%) and Cr (99.99 wt%). These elements were arc-melted together into a rod-shaped 30 g ingot under Ar at a pressure of 0.8 - 0.9 atm on a water-cooled copper hearth. Ingots were turned over and re-melted three or four times to ensure homogeneity. The as-cast rods were sealed in fused quartz tubes which were evacuated and back-filled with Ar. Heat-treatments were carried out in a chamber furnace. The heat-treatment schedule employed was two-stage, to attempt to produce a primary precipitate initially and a secondary precipitate in the second stage. The times and temperatures used were 180 h at 1150 °C and 72 h at 950 °C. The crystal structures of the phases produced were checked using XRD and TEM. The XRD conditions were the same as set out in chapter 2. Accurate lattice parameter determination was carried out using Philips X'Pert profile fitting software, to determine the misfit in each case.

4.2.1 The ElectroThermoMechanical Test Unit (ETMT)

Mechanical properties determination was carried out in the UK National Physical Laboratory's Electro-ThermoMechanical Test unit (ETMT), which was chosen for its temperature capability and small sample size. A schematic diagram of the ETMT is shown in figure 4.8. This system has been shown to reliably reproduce test results gained using other methods (e.g. conventional testing of large specimens in a load frame) [13].

4.2.1.1 Sample Preparation

Samples for the ETMT were machined by spark erosion and were 40 mm long with a cross-section of 2 x 1 mm. Thermocouples were produced by fusing pure Pt and

Pt – 13 wt%Rh wires at one end. The thermocouple was spot-welded to the larger face (2 mm wide) at the mid-point of the specimen, or slightly to one side if the sample exhibited a high level of porosity at one end. Electrical contacts were made by spot-welding short lengths of pure Pt wire onto the same face as the thermocouple, 1 mm either side. These contacts were for strain measurement, using the method set out below.

4.2.1.2 Operation of the ETMT

Samples are gripped in water-cooled brass crossheads. Sample heating is achieved by passing a current through the sample. As a result of the water cooling of the grips the temperature profile along the sample between the crossheads is approximately parabolic at lower temperatures. Above about 1200 °C the temperature distribution of the central portion of the sample is more uniform. The temperature variation in the central 2mm at 1100 °C has been measured to be ±6 °C, and it is in this region that most of the deformation takes place, if the material softens with increasing temperature. Any atmosphere can be introduced into the chamber. In this instance commercial purity Ar was used, to attempt to avoid any oxidation influencing the results.

4.2.1.3 Strain Determination

Strain measurement is achieved by measuring the change in resistance between the two electrical contacts spot-welded either side of the thermocouple. The resistance before deformation, R_o, is given by

$$R_o = rl_o/w_o t_o \qquad (1)$$

where r is resistivity, l_o is the original length between the contact points for measuring resistance and w_o and t_o are the original width and thickness of the testpiece. The instantaneous resistance during the test is hence given by

$$R_i = rl_i/w_i t_i. \qquad (2)$$

Assuming that volume remains constant,

$$V_o = V_i = l_o w_o t_o = l_i w_i t_i. \quad (3)$$

thus

$$R_o = r l_o^2 / V_o \text{ and } R_i = r l_1^2 / V_I \quad (4)$$

so

$$R_o / R_i = l_o^2 / l_i^2 \quad (5)$$

but since true strain, ε, is given by

$$\varepsilon = \ln (l_i / l_o) \quad (6)$$

then using equations (5) and (6),

$$\varepsilon = \ln \sqrt{R_i / R_o} \, . \quad (7)$$

One can therefore measure instantaneous resistance between the two contacts and use the measurement to determine strain. Contact resistance is negligible when compared to the resistance of the sample.

It is worth noting that the above derivation ignores the effects of defects, which is described by the following equation:

$$r = r_T + r_d$$

where r_T is resistivity due to thermal vibrations and r_d is resistivity due to defects [14]. The effect of the defects is independent of temperature. In the case of copper at room

temperature, material that has been deformed by 80 % has 97 % of the conductivity of pure annealed copper [14]. Given this rather small influence of deformation on the conductivity, for small strains it will be negligible and hence is able to be ignored in the present work.

4.2.2 Test Particulars – Pt - Rh - Hf Alloy

The loading approach employed was stepped compression testing. Compression was chosen due to the porosity of the alloys, as they proved to be quite brittle in tension. Compression testing may be conducted in the ETMT as, despite the length of the bar, the only deformation is in the central few millimetres and buckling may be avoided if the strain is not too large. Due to materials limitations stepped testing was deemed the best way to obtain the most information from the available samples. The test temperatures were
1000 °C to 1500°C in 100 °C increments. To examine the effect of prior deformation and thermal history one sample was tested first at 1500 °C and thereafter in 100 °C decrements. As this sample failed after the 1200 °C test another sample was tested at 1000 °C and 1100 °C (temperature increment).

The procedure of the test was as follows. The sample was loaded into the equipment and the chamber was purged with Ar for 15 minutes. The sample was then heated to the required temperature over a period of about 30 seconds, and was allowed to stabilise. The compression test was then conducted, operating under load control. The load was increased by 5 N (2.5 MPa) every second, beginning at zero load and continuing until a plastic strain of 0.2 % had been reached. The sample was then unloaded, heated or cooled to the next test temperature, again allowed to stabilise, and then tested again. After the test series had been completed the current was removed from the sample and it was allowed to air-cool to room temperature. As the grips were water-cooled the sample reached room temperature approximately 20 s after completion of the test.

In addition to the above stepped testing, a further sample was subjected to a compression test, to a strain where failure was initiated. This test was conducted under load control and again using a load increment of 5 N per second, and was ended when the sample failed.

With the remaining sample a creep test was carried out at 1300 °C, under an initial load of 200 N (100 MPa). The sample was heated to temperature, allowed to stabilise and then the load was introduced, being ramped to the target load at 5 N per second. After some time it was apparent that the load chosen had been too low to initiate failure within a reasonable time (one working day), and so the load was raised to 250 N (125 MPa) after a time of 1570 s at the initial load of 200 N.

4.2.3 Test Particulars - Pt-Ti-Cr Alloy

Samples were tested by Dr. Y. Yamabe-Mitarai at NIMS in Tsukuba, Japan, in conventional high-temperature compression testing apparatus, although due to time limitations the samples could not be heat-treated before being sent for testing. These samples proved far too brittle to be tested in the ETMT. Samples were supplied to Dr. Yamabe-Mitarai in the form of rectangular prisms, 2.9 x 2.9 mm in cross-section and 5.8 mm high, and were subjected to stepped compression testing, from 1000 °C to 1500 °C in 100 °C increments. Due to time pressures on the equipment in Japan only one sample was tested.

4.2.4 TEM Sample Preparation

Some samples were examined by TEM after completion of the tests, to examine the effects of deformation on the microstructure and to determine whether the precipitate phase was acting as an effective barrier to dislocation motion. Sample preparation was by the same method outlined in chapter 2.

4.3 Pt - 8.5 %Rh - 17 %Hf Results and Discussion

4.3.1 Microstructure of Test Alloy

The as-cast alloy showed irregular primary dendrites of an $L1_2$ phase in a f.c.c. matrix, which was confirmed by SEM (figure 4.9) and XRD (figure 4.10). The sample was polycrystalline with the width of a typical dendrite being approximately 300 μm. This shows that the composition chosen cannot be cast as a single phase. The primary dendrites are likely to be Rh_3Hf containing a significant amount of Pt substituting for the Rh, as observed in chapter 3.

After heat-treatment the alloy displayed two precipitate types - $L1_2$ precipitates (presumably Rh_3Hf containing a large amount of Pt) in the fcc matrix and fcc precipitates in the prior $L1_2$ dendrites (see figure 4.11). This indicates that the solubility of both the Hf in the fcc phase and the Pt and Rh in the $L1_2$ phase decreases with decreasing temperature, leading to the two precipitates observed (see figure 4.12 for a graphic representation of this phenomenon). The $L1_2$ precipitates in the fcc matrix had no definite shape, unlike the case for the NBSAs. They were approximately spherical to ovoid, with a network of interfacial dislocations. The XRD results showed that the lattice parameters of the two phases were fcc: (3.944 ± 0.002) Å and $L1_2$: (3.994 ± 0.001) Å, which gives a room-temperature misfit of 1.27 % using the equation:

$$\Delta a = \frac{a_1 - a_0}{a_o} \times 100$$

where a_1 is the lattice parameter of the precipitate phase and a_0 is that of the matrix. This is quite high compared to conventional Ni-base superalloys, which generally exhibit misfits of less than 0.5 % at room temperature. The X'Pert program also produced an estimate of 51.1 % by weight of the $L1_2$ phase.

4.3.2 Strength Versus Temperature

4.3.2.1 Data Manipulation and Analysis

The change in cross-sectional area of a sample after a test could not be taken into account for the subsequent tests, but would have been extremely small since the sample was loaded only to just past 0.2 % plastic strain. This implies the change in cross-sectional area would have been no more than about 2.0 % after six tests, but this would lead to a slight over-estimation (in compression testing) of the stress for the later tests on a particular sample, since the cross-section would be increasing slightly with each test. The opposite would be true in tension, where the cross-section would decrease with each test and the strength value would be under-estimated if the original cross-section was used to calculate the stress for later tests, as needs to be the case in stepped testing.

The raw data for a test at 1000 °C is shown in figure 4.13. Note the wide spread of strain values for a given stress level - this is due to the noise in the resistance measurement. When the data are plotted as a moving average of approximately 30 points (the sampling interval was 0.05 s) the noise diminishes greatly, as shown in figure 4.14.

Despite the presence of the Ar atmosphere, the samples oxidised slightly during the test. This had the effect of increasing the resistance between the contacts, as the cross-section of metal was decreasing and was being replaced by higher-resistivity oxide. The effect of the oxidation was barely noticeable at 1000 °C (e.g. figure 4.14), but at 1200 °C and above it was quite severe. This oxidation was manifest in the plot of stress versus strain as a steepening of the initial part of the curve (i.e. increasing Young's modulus), and in severe cases caused the strain to initially appear negative upon loading the sample (see figure 4.15). To overcome this oxidation effect a curve was fitted to the resistance data previous to the test (figure 4.16), so that the contribution to change of resistance from the oxidation could be subtracted to leave the true change in resistance from deformation. This approach was quite successful for short-term tests, as can be seen in figure 4.17.

To measure proof stress, a line was drawn from 0.2 % strain on the strain axis parallel to the initial elastic portion of the curve so that they intersected. This intersection represents a plastic strain in the sample of 0.2 %, so that the "0.2 offset proof stress" ($\sigma_{0.2}$) may be

measured, which is a standard measure of the yield stress for materials not exhibiting a distinct yield point. As the elastic modulus changed with temperature then this was done for each individual test result.

4.3.2.2 Test Results - Stepped Compression Testing

The corrected averaged data for the tested samples are presented in figure 4.18. The first observation from the figure is that the proof stress decreases with increasing temperature. If this material displays anomalous strengthening with increasing temperature then the peak strength occurs at below 1000 °C, although based on the results of Suzuki it seems this would not be the case. The second observation to be made is that the Young's modulus appears higher at 1100 °C than at 1000 °C. Whether this is a real effect or due to oxidation is undetermined, although the effect is observed in both samples where the temperature was increasing between tests.

Agreement between duplicate tests was good, as can be seen in the proof stress versus temperature plot shown in figure 4.19. No influence of prior deformation was evident at the higher test temperatures (1400 °C and 1500 °C), and the $\sigma_{0.2}$ values for the sample with increasing temperature were actually lower than for the sample with decreasing temperature, despite the overestimation of stress levels due to prior deformation. This is opposite to the expected effect. Despite this, the values were within 20 % of each other.

When compared to values for pure Pt and strengthened Pt (solid solution strengthened and oxide dispersion strengthened), the excellent strengthening achieved by introduction of an $L1_2$ precipitate is evident. Figure 4.20 shows the averaged values of $\sigma_{0.2}$ for the Pt-Rh-Hf alloy compared with typical values for pure Pt and oxide dispersion strengthened (ODS) Pt - 10 wt%Rh. At 1000 °C, the Pt-Rh-Hf alloy has a $\sigma_{0.2}$ of approximately fifteen times that of pure Pt and seven times that of ODS Pt – 10 wt%Rh.

4.3.2.3 Test Results - Single Compression Test

The stress-strain curve from the single compression test to failure is shown in figure 4.21. The proof stress is approximately 215 MPa, which is consistent with the values given in figure 4.20. This shows that the prior thermal and deformation history in the stepped

testing approach has a negligible influence on $\sigma_{0.2}$ if the strain at each temperature is kept quite small.

The strain at failure was 4.9 %, which is low compared to that of pure platinum (40 % at room temperature [15], and likely to be higher at 1300 °C). This is most likely because the test was load-controlled, such that the UTS of the material was exceeded at 5 % strain. If strain control had been adopted then the strain to failure would have been larger. From this we can assume the UTS of the alloy at 1300 °C is the breaking stress, which was 355 MPa.

The sample failed by transverse fracture, although some buckling in the central hot portion was observed. This exposes the limitations of compression testing in the ETMT, as any non-axial load will eventually be manifest in sample buckling. Beyond small strains the sample is likely to fail by this method. If this were to happen in stepped testing it could be overcome by straining in tension until the sample becomes straight again, but this induces large amounts of deformation into the material which may influence the results of subsequent tests. The sample could be annealed between tests, but this would change the precipitate volume fraction and would hence affect results.

4.3.2.4 - Test Results - Single Creep Test Under Compression

The strain versus time curve from the compression creep test is shown in figure 4.22. The same approach was taken to correcting data as was used in the stepped compression testing, where the sample was allowed to stabilise at temperature and the change in resistance with time at zero load was approximated using a curve fit. This curve fit was subtracted from the test data to gain the true change in resistance due to the creep strain. It can be deduced from figure 4.22 that this approach was not entirely successful, as the creep strain in the first 3000 s appears to be negative. This is due to the curve fit slightly underestimating the true oxidation contribution to the resistance change. As the curve fit was based on approximately 600 s of data and the test lasted 12000 s, it is understandable that the oxidation effect was still evident in the "corrected" data. One could manipulate the data in such a way that the creep strain is positive, but any such manipulation would give

an arbitrary result where the true magnitude of the strain at any given point would depend solely on the curve fit chosen. For this reason the data will be interpreted as corrected in figure 4.22, and it is noted that the true strain to failure is greater than the 12 % shown on the graph.

The creep response could also be determined, however, by considering the displacement of the crosshead, since this will be unaffected by the oxidation of the sample. Figure 4.23 shows the crosshead displacement versus time for the creep test. This data is of no value, however, unless the creep response of the material over a range of temperatures is known. The reason for this is the temperature gradient along the sample - creep will be occurring in varying amounts along the bar, rather than just in the central region between the contacts. To determine the creep between the contacts one would need to integrate the function describing the amount of creep occurring in the test time as a function of temperature, where the lower and upper limits are room temperature and the maximum temperature in the bar. One could use a Larson-Miller parameter as the function for this integration, but for this approach to be valid one would have to assume that all creep is occurring at a constant rate at all temperatures and that failure strain is independent of load or temperature. In this case, with only one value of failure strain (quoted above from the resistance measurement results) and there being uncertainty with that value due to oxidation, significant error is likely to be introduced by using this method. In addition, with only one point to work with on a Larson-Miller plot, a slope must be assumed. The slope of a single-phase alloy (e.g. Pt – 10 wt%Rh) could be used, although the creep response due to the $L1_2$ precipitates may influence this slope somewhat. With these considerations in mind the estimation of the "true" creep response of the sample cannot be reliably obtained from the crosshead displacement given the limited data available. If more were known about the creep response of the material this conversion could be carried out with some confidence. Perhaps it would be easier to introduce a truly protective atmosphere (e.g. slightly reducing, such as 5 %H_2 in N_2, or dried Ar) into the sample chamber so that oxidation does not occur during the test and the above analysis would be unnecessary.

Despite the above problems with oxidation, the life at a given set of conditions has been determined. For the conditions of 1300 °C and 125 MPa (100 MPa for the first 2850 s of the test) the creep life was 3.3 h, which is far better than any other Pt-based material at these conditions. The results of Hill for two-phase alloys based on Pt - Al and Pt - 10 wt%Rh [6], the results of Knight and Taylor [16] for ODS Pt - 10 wt%Rh, and the result for the above test are plotted on a Larson-Miller plot (figure 4.24) for comparison purposes. It can be seen that the alloy developed by Hill was better than the Pt - Rh alloy, and that the Pt - Rh - Hf developed in this study is better still. Compared to Pt - 10 wt%Rh [16] which sustained 31 MPa for 3.3 h at 1300 °C, the Pt - Rh - Hf alloy sustains four times the load for the same failure time. This comparison, however, is not strictly correct, since in compressive loading the true stress on the sample continuously decreases, whilst in tension it constantly increases. Despite this the results show that the Pt - Rh - Hf alloy possesses very good creep strength compared to other Pt-based materials.

4.4 Pt - 6.5 %Ti - 13 %Cr Results And Discussion

4.4.1 Microstructure

The sample produced for testing at NPL (figure 4.25) was two-phase. In the inter-dendritic regions this sample contained cuboidal/spherical γ' precipitates of approximately 100 nm in diameter in a matrix of γ, although most of the sample consisted of a phase that appeared to have been prior γ' dendrites. The width of the interdendritic regions within which the precipitates in figure 4.25 existed were approximately 500 nm, and constituted a very small volume fraction of the alloy.

The sample tested at NIMS was not examined prior to testing. It is likely that it consisted of a large volume fraction of γ' dendrites with inter-dendritic γ.

4.4.2 Strength Versus Temperature

Unlike the output from the ETMT, the data provided by the compression test on the load frame required no further processing to account for extraneous effects such as the oxidation seen above. The plots of stress versus strain for the various temperatures are shown in figure 4.26, and the calculated 0.2 % proof stress versus temperature in figure 4.27. As for the Pt - Rh - Hf alloy in section 4.3, there was no distinct yield point; instead a gradual yield was observed, as is characteristic of most f.c.c metals. Figure 4.27 shows the strength decreasing continuously over the temperature range 1000 °C – 1500 °C, with a surprisingly low elastic modulus (6.3 GPa).

This strength level of the Pt - Ti - Cr alloy is much lower than that of the Pt - Rh - Hf alloy discussed above. There may be several reasons for this, but the two most likely are the microstructure and the second phase. As discussed above, the Pt - Ti - Cr alloy was unable to be heat-treated before testing due to time restrictions. While this is regrettable, the results are useful for comparison purposes, although the heat-treated strength is likely to be higher than the as-cast strength, at least at the lower end of the temperature range investigated. At higher temperature precipitate dissolution is likely to occur. The second phase present was dendritic rather than existing as small precipitates, so the motion of dislocations through the f.c.c. phase would have been relatively unhindered in the tested condition. Suzuki did not investigate the dendritic phase, $Pt_3(Ti,Cr)$, although in his work the high-temperature strengths of Pt_3Ti and Pt_3Cr were shown to be significantly lower than that of "Pt_4Hf", which is the γ' strengthening phase in the Pt-Rh-Hf alloy discussed above. It appears that the proof strength of the mixed γ' phase $Pt_3(Ti,Cr)$ is similar to that of the equivalent binary phases Pt_3Ti and Pt_3Cr.

In figure 4.28, the Pt - Rh - Hf and Pt - Ti - Cr results are compared to those of Hill. It can be seen that the 0.2 % proof stress of the Pt - Rh - Hf alloy is far higher than the Pt - Al - X alloys of Hill, approximately double the strength of the best of Hill's alloys (Pt - Al - Re). The Pt - Ti - Cr alloy exhibited similar performance to the better Pt - Al - X alloys, namely Pt - Al - Re and Pt - Al - Ru.

4.5 TEM Investigation of As-Deformed Structure

TEM samples were produced from several Pt-Rh-Hf mechanical test samples, to assess the effect of the deformation on the microstructure, and to determine the effectiveness of the precipitates as barriers to dislocation motion. Two samples were examined, one being the sample which was subjected to stepped compression testing beginning at 1500 °C followed by 100 °C decrements to a final test at 1200 °C, and the second sample being that which was subjected to a single compression test to failure at 1300 °C. These will be referred to as samples A and B respectively.

4.5.1 Sample A

Images were taken close to a {001} zone axis, with the sample oriented in a two-bean condition. A number of dislocations are visible in figure 4.29, as well as some precipitates. The majority of dislocations observed were rather bowed, and appear hindered in their motion by the precipitates present.

While it was an aim of this experimental program to produce an alloy with a high volume fraction of γ', it is apparent that heating to 1500 °C results in a dramatic decrease in the γ' volume fraction through particle dissolution. The volume fraction of γ' in this sample was far lower than in the as-heat-treated samples. This will most likely be a result of the solubility of Hf in γ being higher at 1500 °C than at the final heat treatment temperature (950 °C).

4.5.2 Sample B

In this sample there was a very low volume fraction of γ' compared to as-heat-treated samples, which is to be expected since the test temperature for this sample was 1300 °C and significant precipitate dissolution will have occurred. The dislocation density was quite high in this sample, and there appears to be a greater degree of tangling between dislocations than in sample A. This is no doubt due to the total deformation being far higher in this sample than in sample A. In addition to the dislocation density, a large

number of stacking faults were observed (see figure 4.30, imaged in a two-beam condition), existing on a plane containing [110] since they were edge-on when viewed down the [110] zone axis. In most f.c.c. metals at room temperature the plane of the stacking fault is {111}, and this direction certainly contains <110> variants so that may certainly be true of this case as well.

It can be seen that shear bands of dissociated partial dislocations are present in the as-deformed alloy (see figure 4.31). It can be seen that the spacing of the pairs of partial dislocations is regular along their length, and it is fair to assume that the Burgers vectors for each half of one pair of the partial dislocations would be the same along the slip band.

In most $L1_2$ phases, the <110> dislocation may dissociate into two 1/2 <112> partial dislocations, separated by a stacking fault. In this instance there is some visual evidence of a stacking fault between the partial dislocations in the bright-field image. Contrast arising from stacking faults within the f.c.c. phase appears as bands of alternating dark and light stripes, and will appear perpendicular to the dislocation lines between the pairs of partial dislocations. Some intensity variation can be seen along the length of the dislocation pairs, which may be a result of a stacking fault.

The absence of the stacking faults in sample A might be a result of sample annealing between tests. Another explanation may be that sample A was not subjected to as much plastic deformation as sample B - total plastic deformation in sample A was less than 2 %, while in the latter it was approximately 6 % at failure.

4.6 Conclusions

This chapter has described investigations into the microstructure and mechanical properties of a Pt - Rh - Hf and a Pt - Ti - Cr alloy. It has been shown that two-phase Pt alloys can be produced with a bimodal distribution of $L1_2$ precipitates in a f.c.c. matrix.

It was observed that the Pt - 8.5 %Rh - 17 %Hf alloy possessed a microstructure consisting of discrete large (several hundred nanometres) and fine (less than 100 nm) γ' precipitates (based on the binary γ' phase observed in the Pt-Hf binary system in chapter 2) in a matrix of f.c.c. (Pt). The misfit between these phases was relatively high (compared to that of most NBSAs).

The proof stress and creep resistance under Ar of the Pt - 8.5 %Rh - 17 %Hf alloy were shown to be several times higher than that of pure Pt and an ODS Pt-Rh alloy. The introduction of the precipitates into the alloy increased proof stress by 7 times (compared to a Pt - 10 wt% Rh alloy, which approximates the matrix), and by 15 times when compared to pure platinum. The creep resistance was also shown to be relatively good compared to single-phase and other two-phase (Pt) alloys.

The mechanical properties of the Pt - Ti - Cr alloy tested were shown to be inferior to those of the Pt - Rh - Hf alloy tested. The proof stress of the Pt - Ti - Cr alloy was found to be lower than that of the Pt - Rh - Hf alloy, though still better than the proof stress of several other two-phase Pt alloys. The alloy appeared to be very brittle at room temperature, and no measure of ductility was gained at high temperature due to the stepped testing approach employed.

The above indicates the Pt - Rh - Hf alloy developed possesses the high-temperature proof stress required of a high-temperature creep-resistant structural material based on Pt.

4.7 References

1. D-M. Wee and T. Suzuki, Trans. JIM, **20** 634 (1979)
2. D-M. Wee, O. Noguchi, Y. Oya and T. Suzuki, Trans. JIM, **21** 237 (1979)
3. T. Suzuki and Y. Oya, J. Mat. Sci., **16** 2737 (1981)
4. British Patent 1 238 013
5. US patent 6071470
6. P. Hill, PhD Thesis, Univ. Witswatersrand (2001)
7. IM Wolff and P J Hill, Plat. Metals Rev. **44** 158 (2000)
8. PJ Hill, LA Cornish, P Ellis and MJ Witcomb, J. Alloy. Compound., **322** 166 (2001)
9. PJ Hill, Y Yamabe-Mitarai and IM Wolff, Scripta Mat. **44** 42 (2001)
10. PJ Hill, T Biggs, P Ellis, J Hohls, S Taylor and IM Wolff, Mat. Sci. Eng. A **301** 167 (2001)
11. C. Capdevilla, Y.L. Chen, N.C.K. Lassen, A.R. Jones and H.K.D.H. Bhadeshia, Mat. Sci. Tech. **17** 693 (2001)
12. B Roebuck, R Morrell and PM Mummery, Mat. Sci. Tech., **16** 817 (2000)
13. B Roebuck, MG Gee, JD Lord and LN McCartney, Mat. Sci. Tech., **14** 1001 (1998)
14. D. R. Askeland, "The Science and Engineering of Materials", Chapman and Hall, London, 1984, p 644-646.
15. Platinum Metals Review, **1** 61 (1957)
16. JR Knight and B Taylor, Powder Met., 10 108 (1962)
17. A. S. Darling, International Metals Reviews, 91-122 (1973)
18. Y. Yamabe-Mitarai, Y. Ro, T. Maruko, T. Yokokawa and H. Harada, Proc. Structural Intermetallics 1997, The Minerals, metals and Materials Society, Warrendale, 805-814 (1997)
19. D. Cox, PhD Thesis, University of Cambridge (2000)

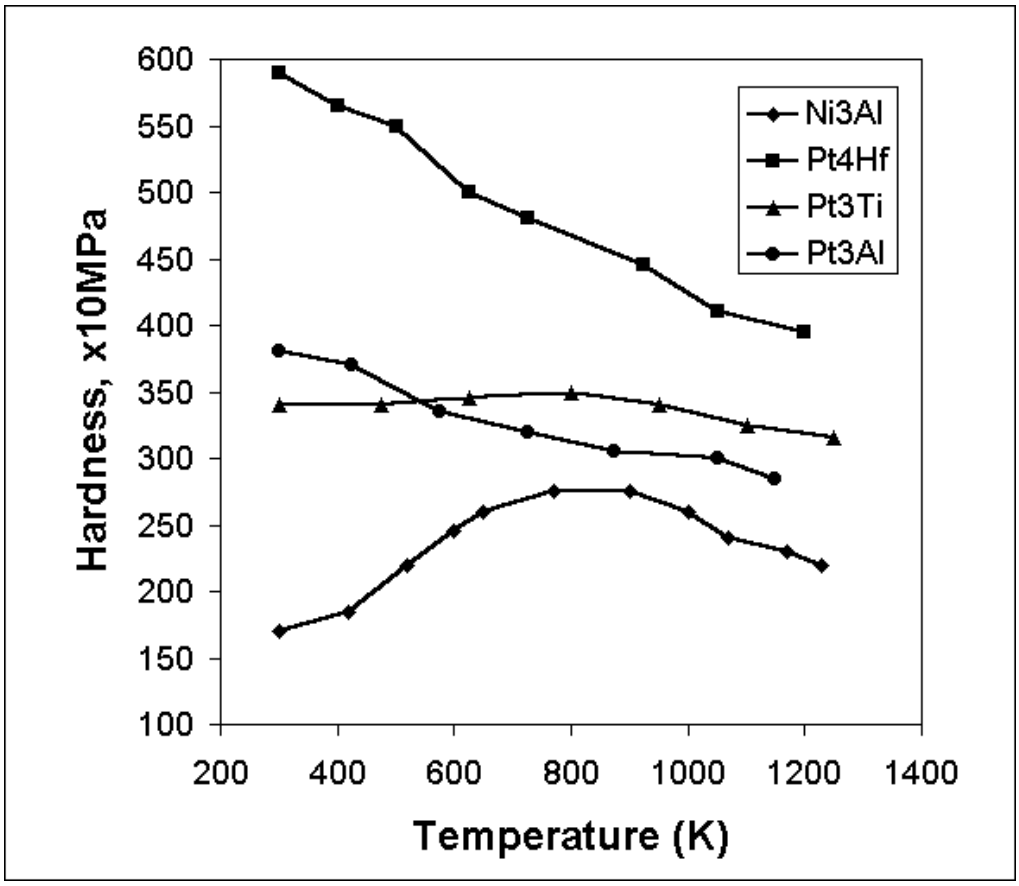

Figure 4.1 Suzuki's data for the hot hardness of Pt-based $L1_2$ phases [1,2]

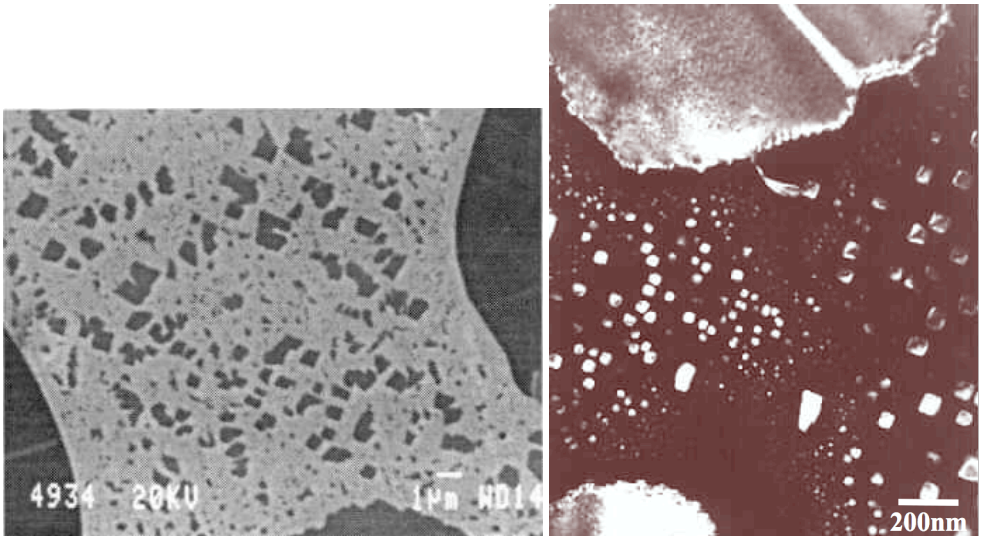

(a) (b)

Figure 4.2 Microstructure of:
(a) a heat-treated Pt - Ru - Al alloy – cuboidal $L1_2$ precipitates in a f.c.c. matrix, plus $L1_2$ dendrites (backscattered SEM image), and
(b) a heat-treated Pt - Al - Cr alloy (dark field TEM image, no **g** given) [6]

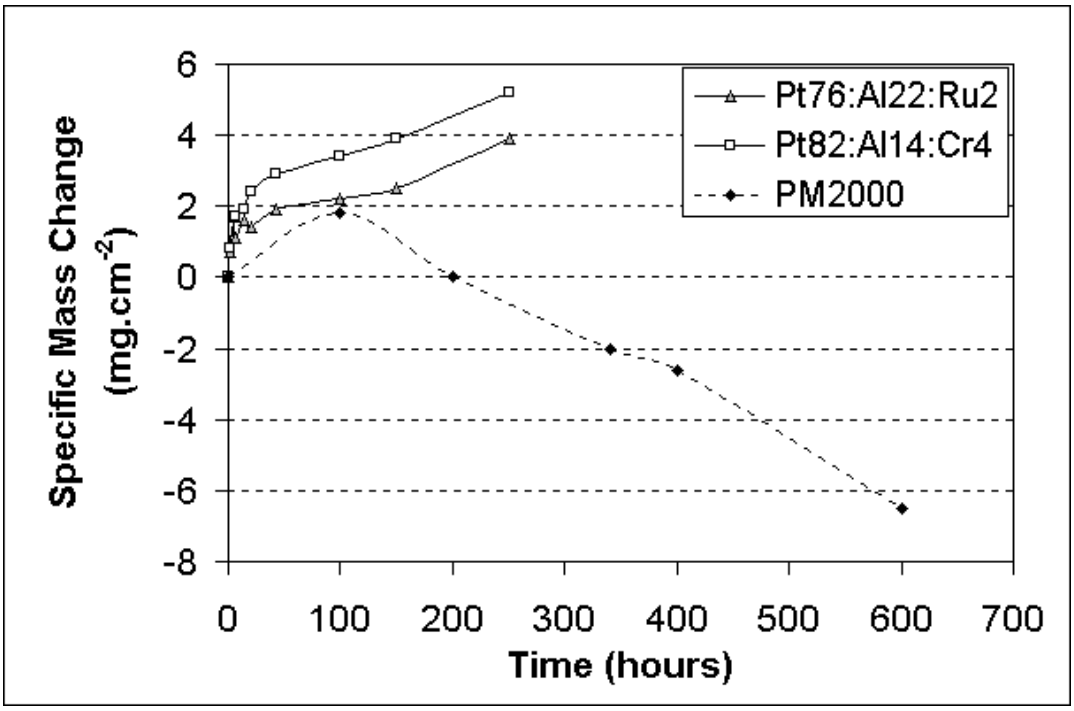

Figure 4.3 Oxidation behaviour for two Pt-based alloys in long-term static oxidation tests. Data for PM2000 are also included for comparison. [6]

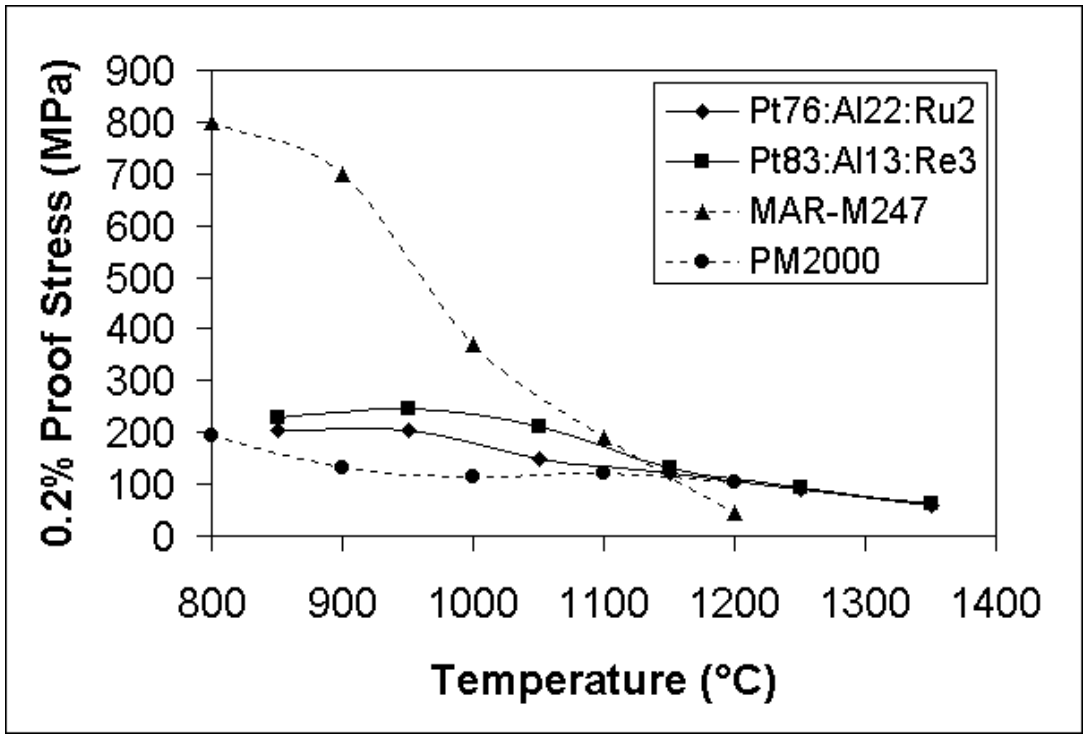

Figure 4.4 Plot of 0.2 % proof stress versus temperature for Pt - Al - Ru and Pt - Al - Re alloys, compared with PM2000 and Mar-M247 [6]

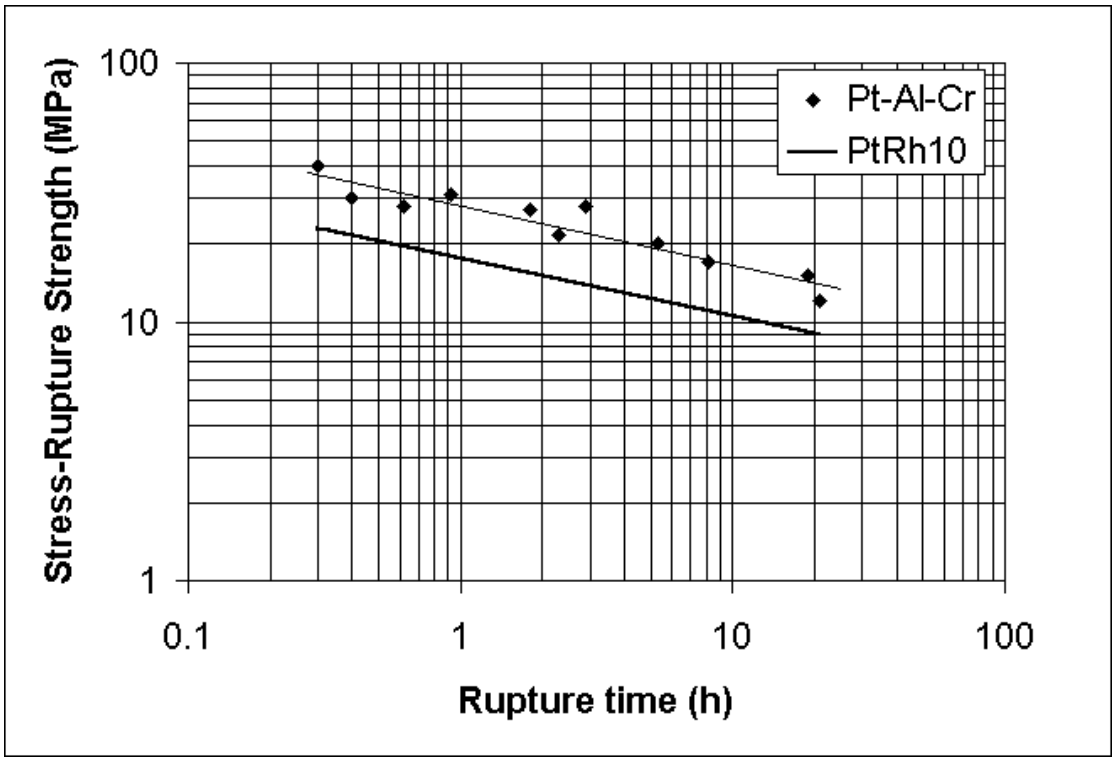

Figure 4.5 Creep data for a Pt - Al - Cr alloy at 1300 °C. Note the similarity in slope between the single-phase and the two-phase Pt alloys. [6]

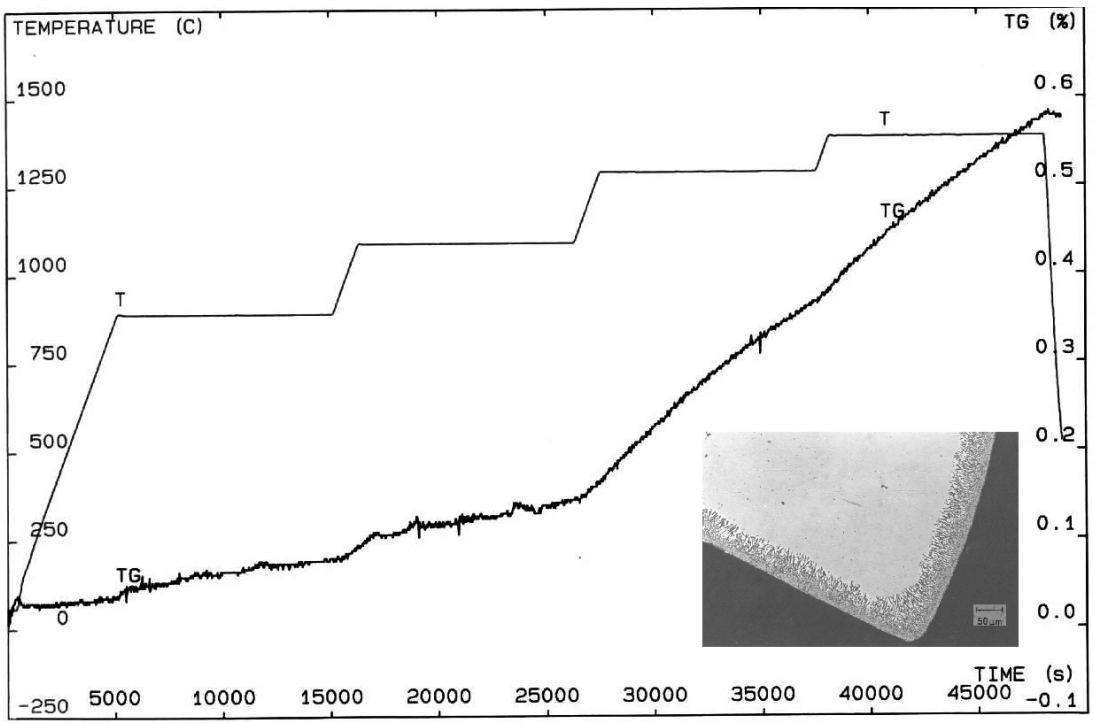

Figure 4.6 Preliminary oxidation test of Pt - 13 at%Hf alloy in a static air atmosphere. The inset picture shows the extent of the oxide growth within the sample.

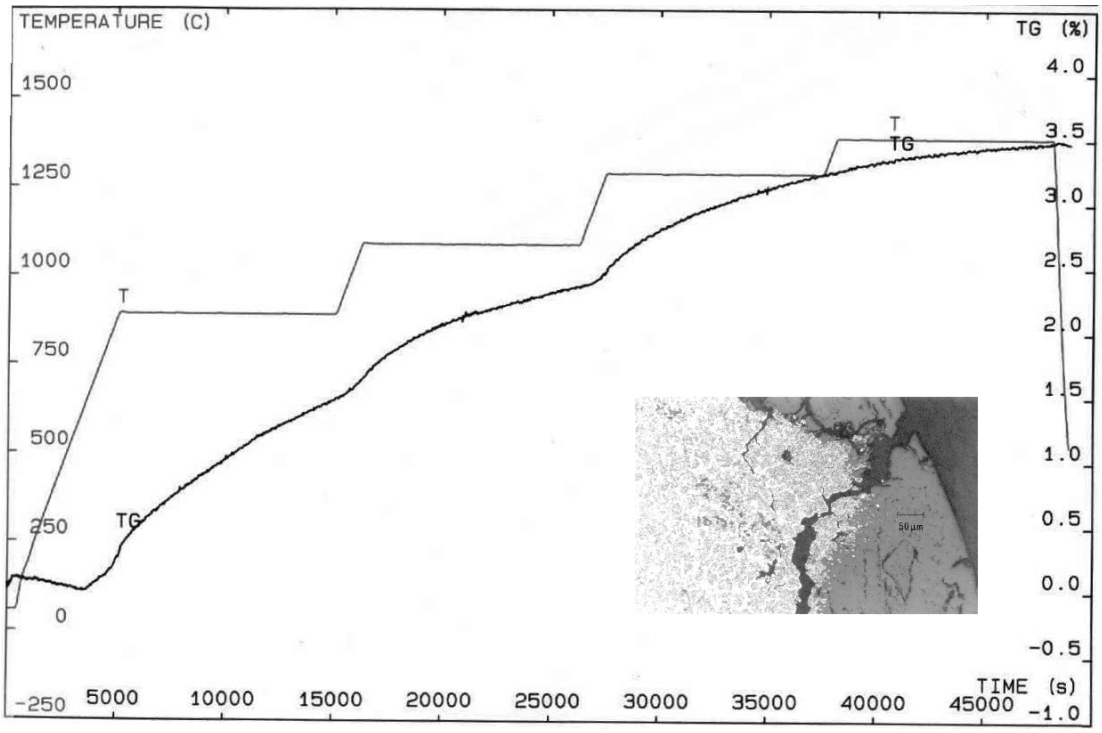

Figure 4.7 Preliminary oxidation test of Pt - 23 at%Zr alloy in a static air atmosphere. The inset picture shows the extent of the oxide growth within the sample.

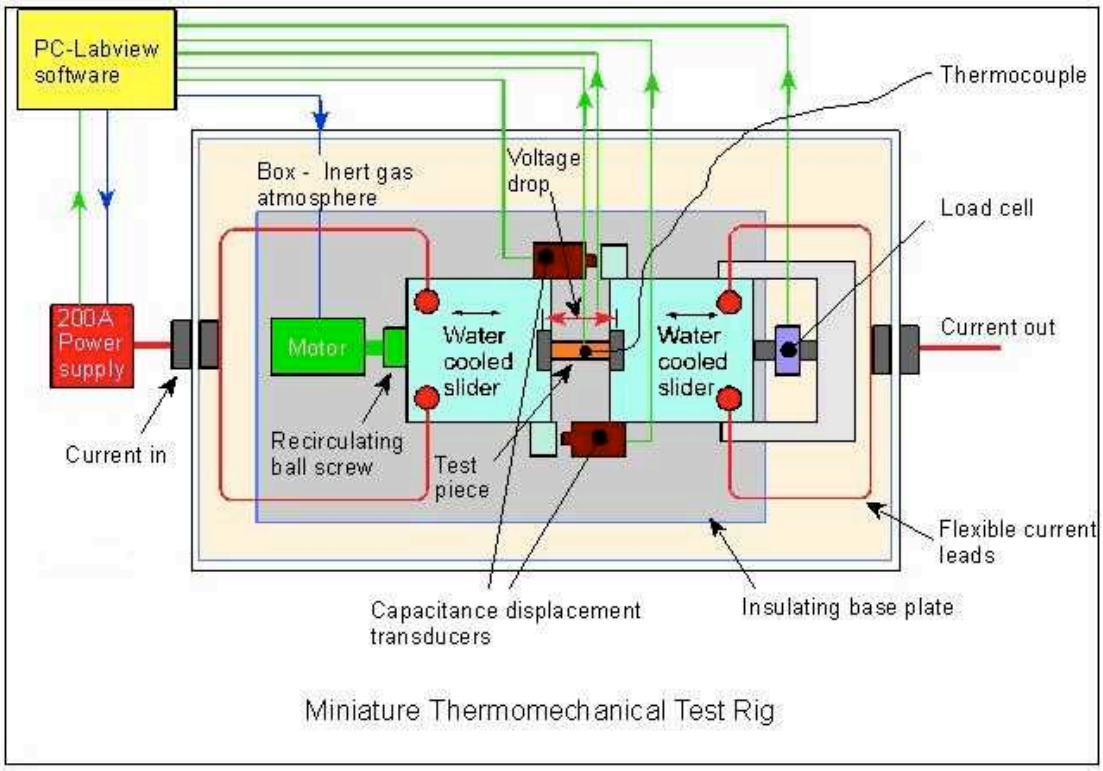

Figure 4.8 Schematic diagram of the ETMT used for mechanical testing in this chapter.

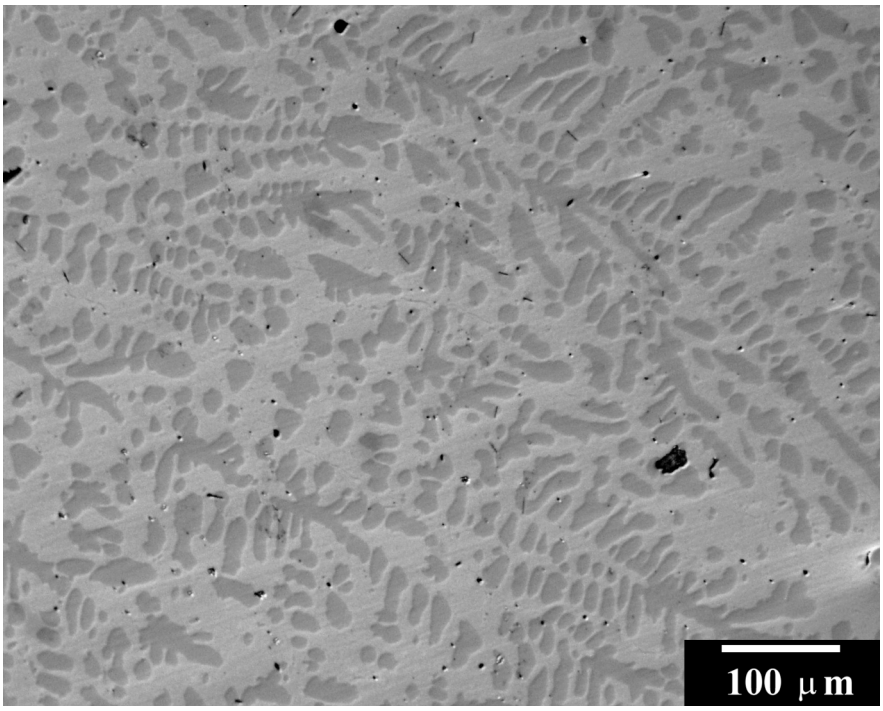

(a)

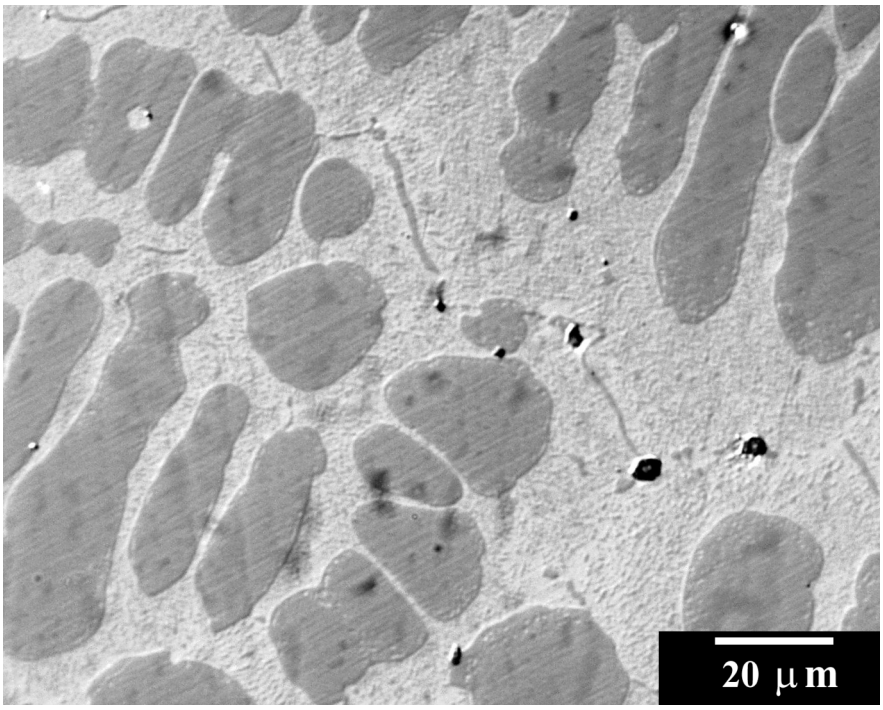

(b)

Figure 4.9 Nomarski interference contrast image of the Pt - Rh - Hf test alloy (polished to 0.05 μm colloidal SiO_2, no etch):
(a) low magnification image showing the as-cast structure of $L1_2$ dendrites in a f.c.c. matrix, and
(b) higher magnification image showing precipitation within the matrix and the surface regions of the dendrites.

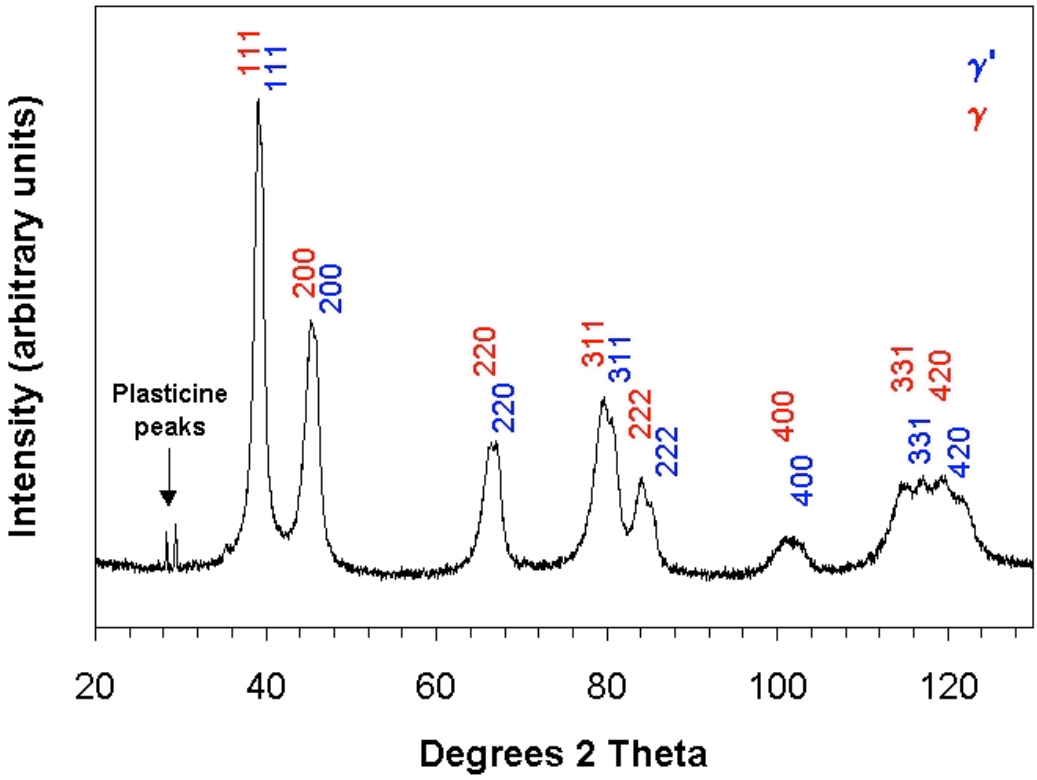

Figure 4.10 XRD trace of the Pt - Rh - Hf test alloy, showing two phases based on f.c.c..

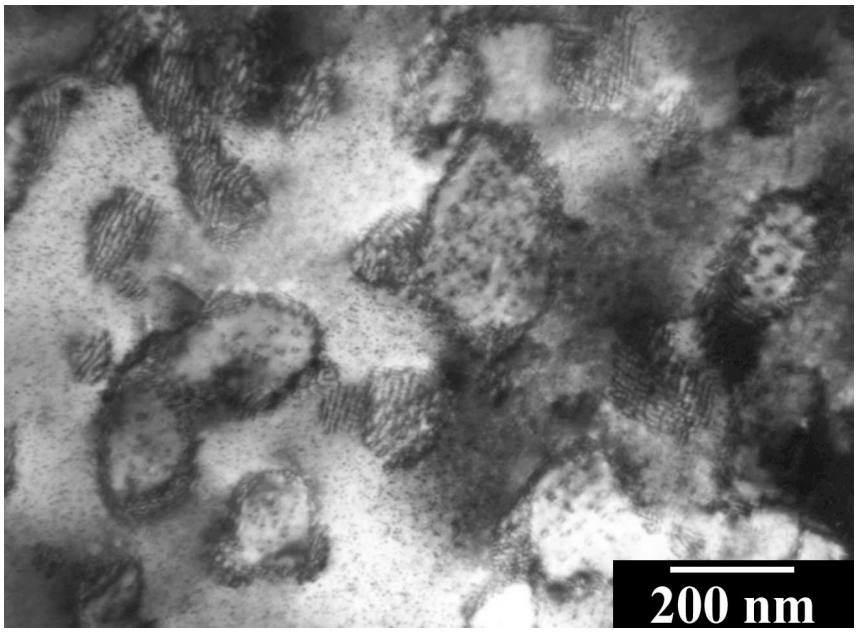

(a)

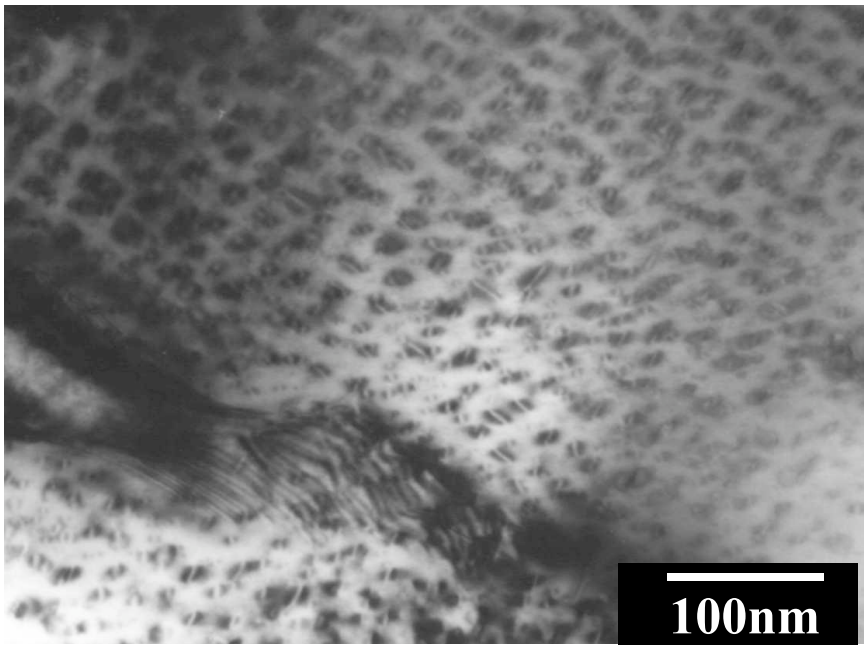

(b)

Figure 4.11 TEM bright-field images of the Pt - Rh - Hf alloy after heat-treatment:
(a) $L1_2$ precipitates in the f.c.c. matrix, and
(b) f.c.c. precipitates in the $L1_2$ dendrites

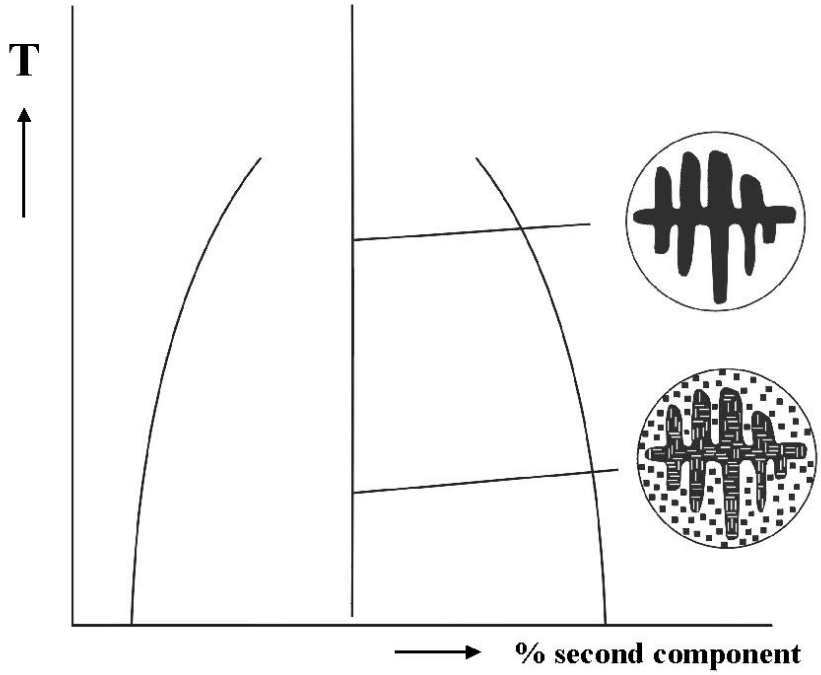

Figure 4.12 Diagrammatic representation of the development of two precipitates during heat treatment.

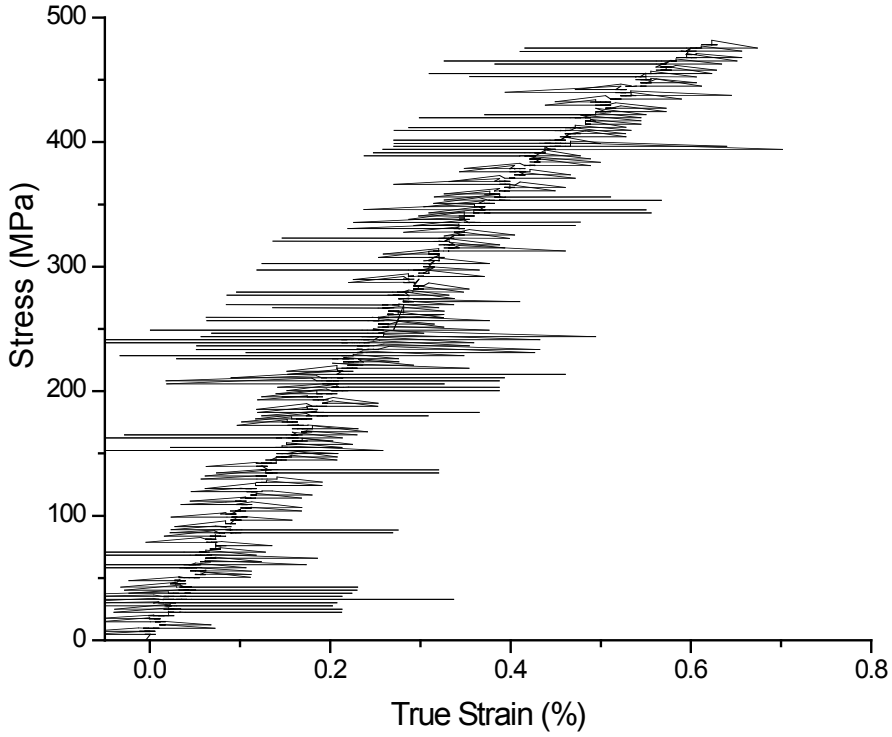

Figure 4.13 Raw stress-strain data plot for a Pt - Rh - Hf sample tested at 1000 °C, illustrating the noisy nature of the raw data.

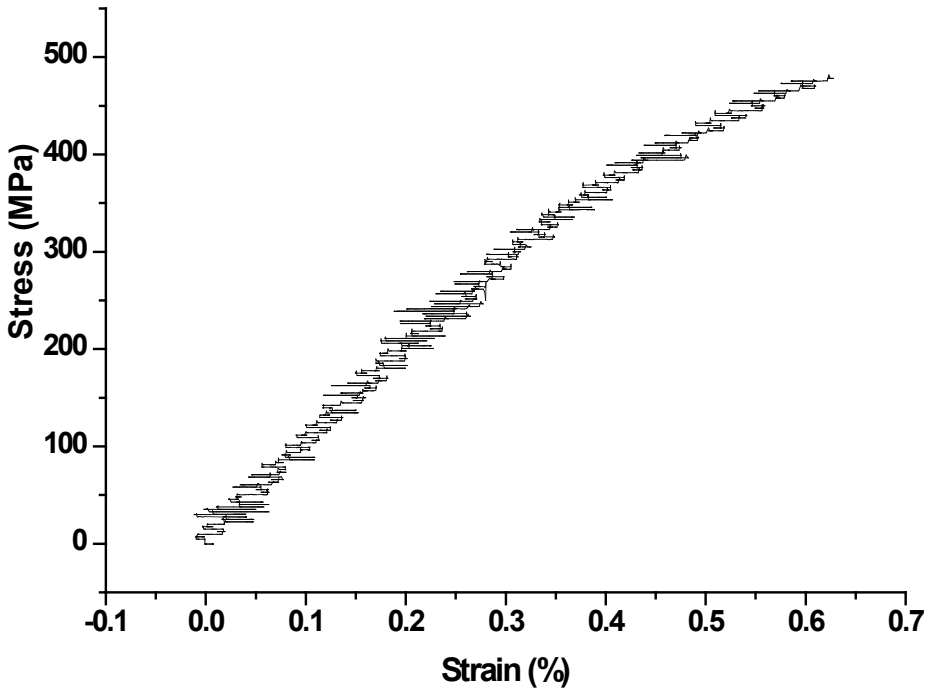

Figure 4.14 An 11-point moving average plot of the data in figure 4.13.

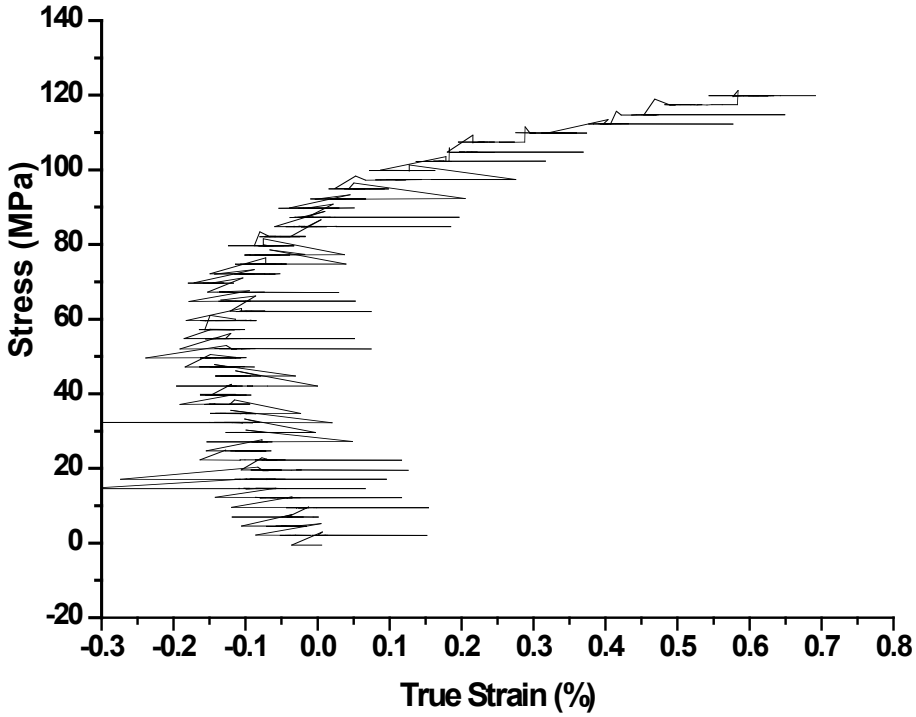

Figure 4.15 The effect of oxidation during the test on the test data – an apparent negative Young's Modulus for a Pt - Rh - Hf sample tested at 1500 °C.

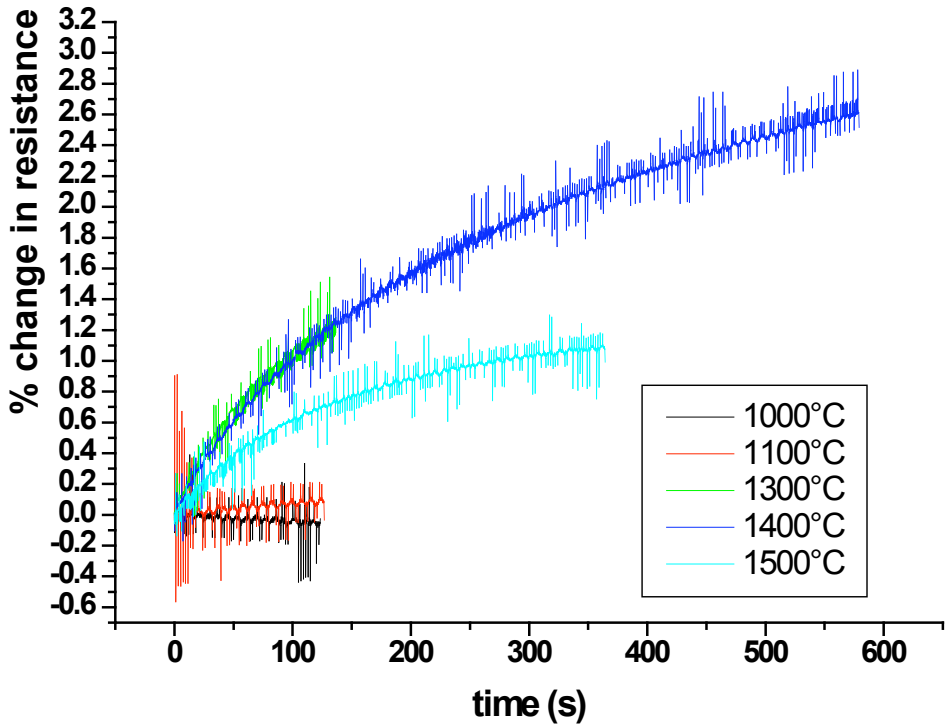

Figure 4.16 Change in sample resistance in Pt - Rh - Hf samples due to oxidation before testing.

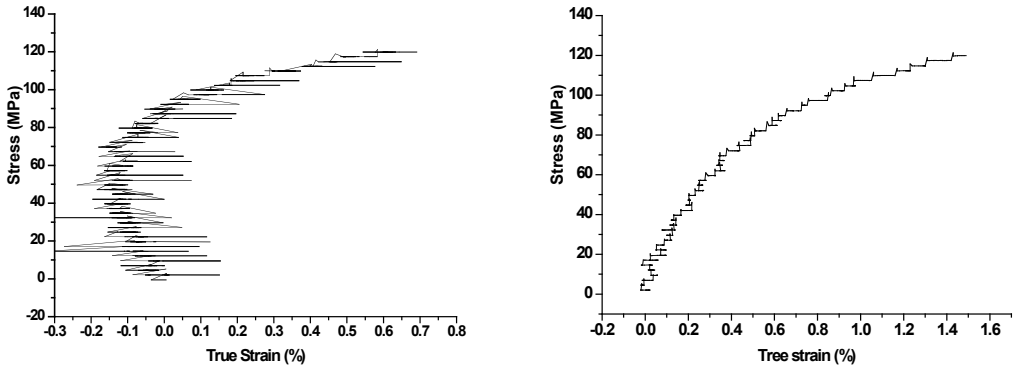

(a) (b)

Figure 4.17 Correction of data in figure 4.15 for oxidation:
(a) before correction, and
(b) after correction and averaging.

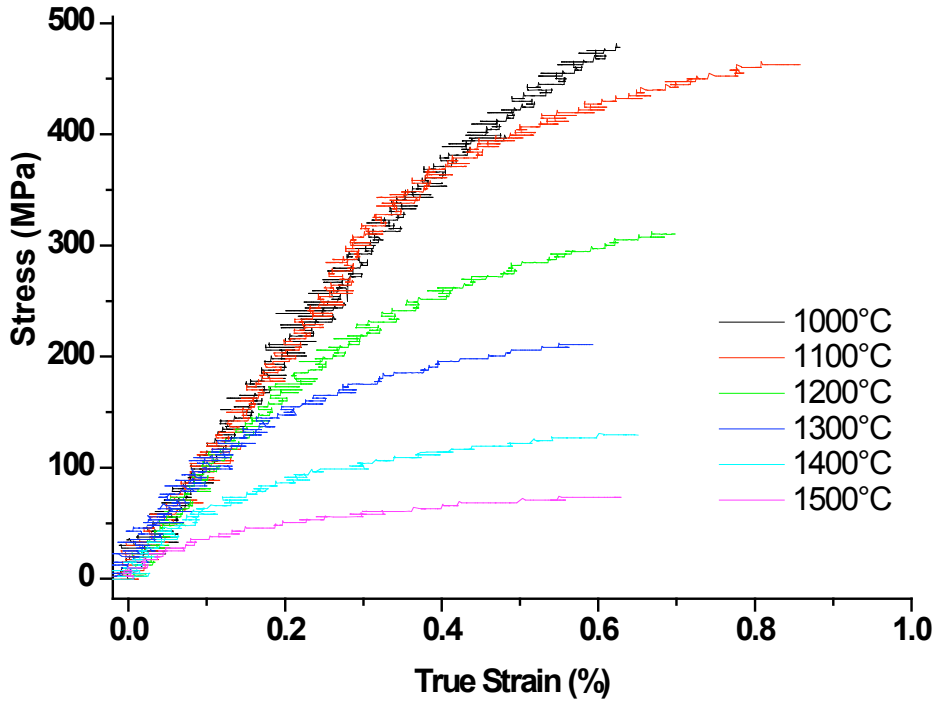

Figure 4.18 Oxidation-corrected and averaged set of curves obtained from one Pt - Rh - Hf sample.

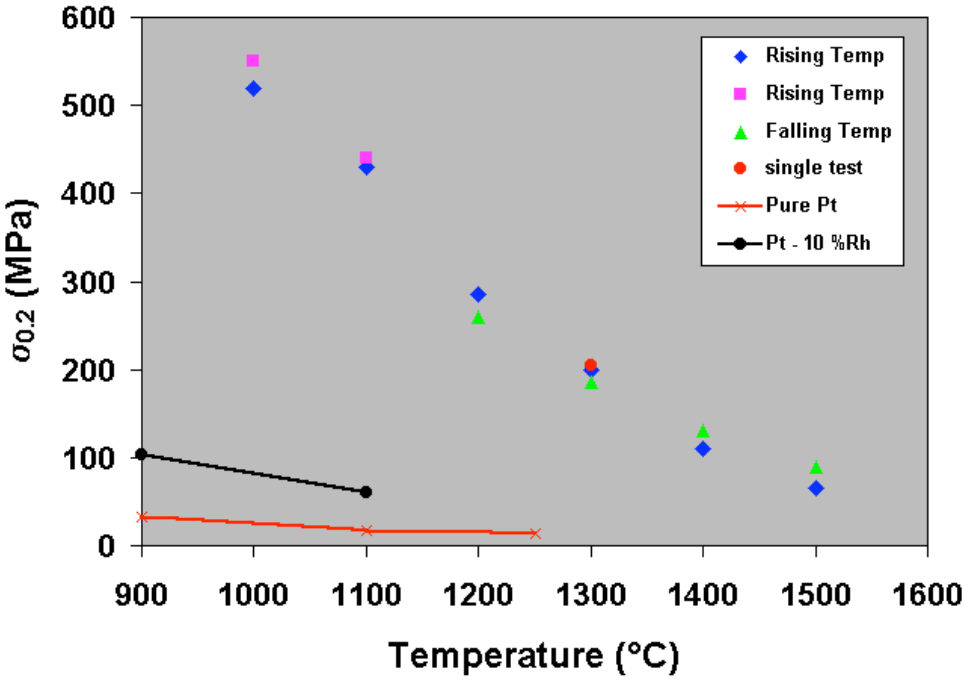

Figure 4.19 Proof stress versus temperature for all Pt - Rh - Hf samples, and compared to pure Pt and Pt - 10 wt%Rh alloy [16,17].

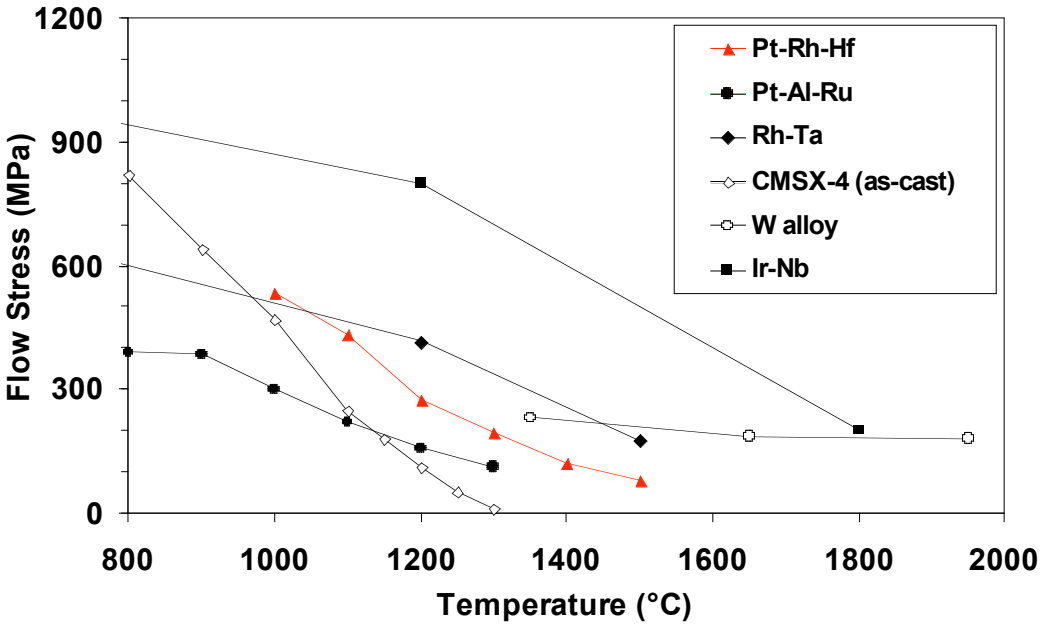

Figure 4.20 Plot comparing the 0.2 % proof stress of Pt - Rh - Hf alloy with that of some other alloys [6, 18, 19].

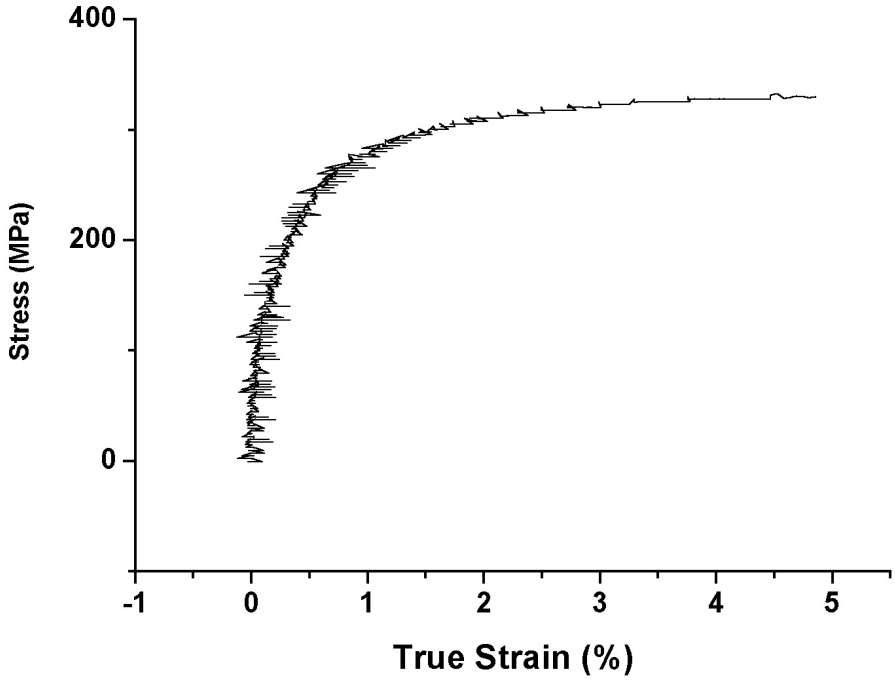

Figure 4.21 Stress-strain curve for the Pt – Rh - Hf sample subjected to a single compression test at 1300 °C.

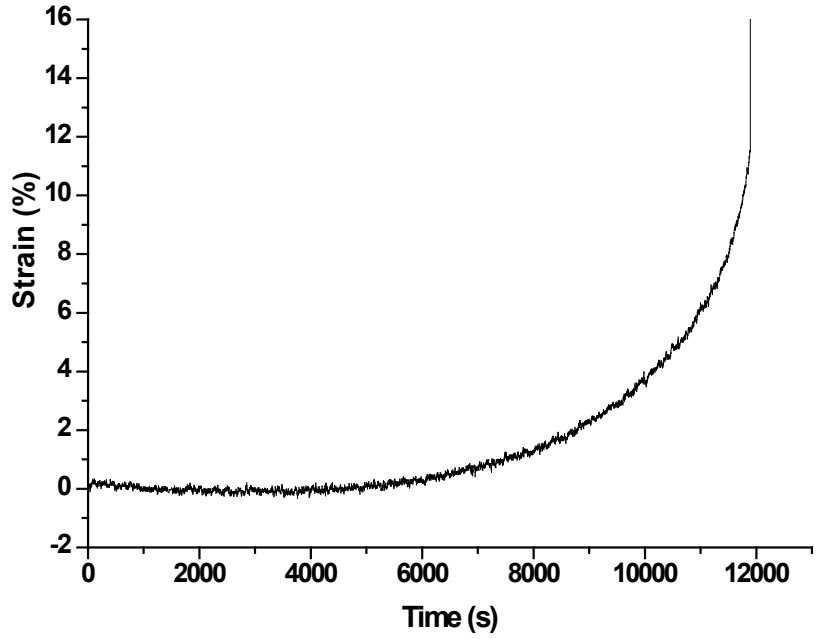

Figure 4.22 Creep data for the single Pt-Rh-Hf creep test, corrected for oxidation. Note that the strain decreases initially, which indicates the correction was not completely successful.

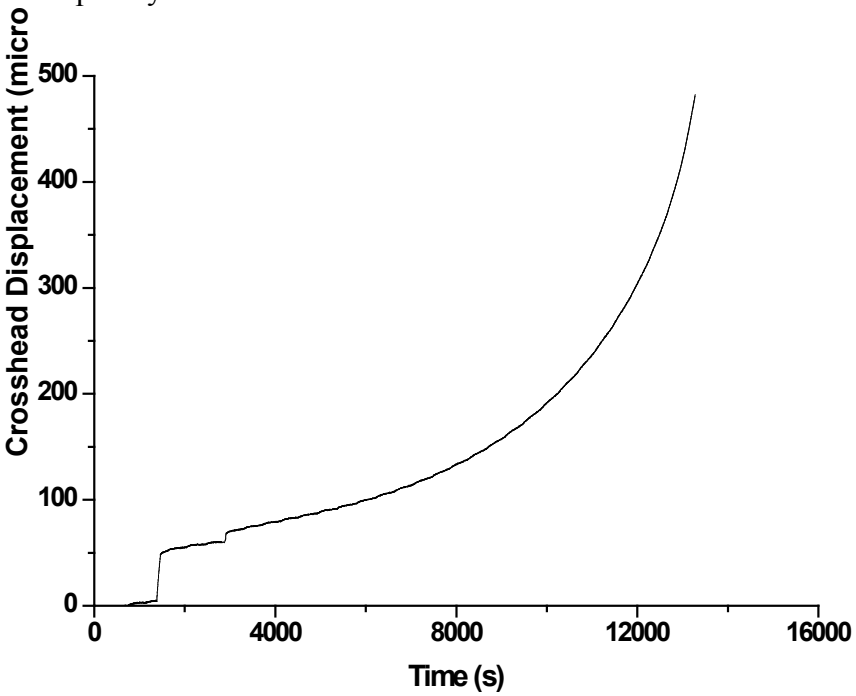

Figure 4.23 Plot of crosshead displacement versus time for the creep test. Conversion of crosshead displacement rate to strain is quite complicated and requires more data than are available for this alloy. The step at 3000 s is due to a load increase.

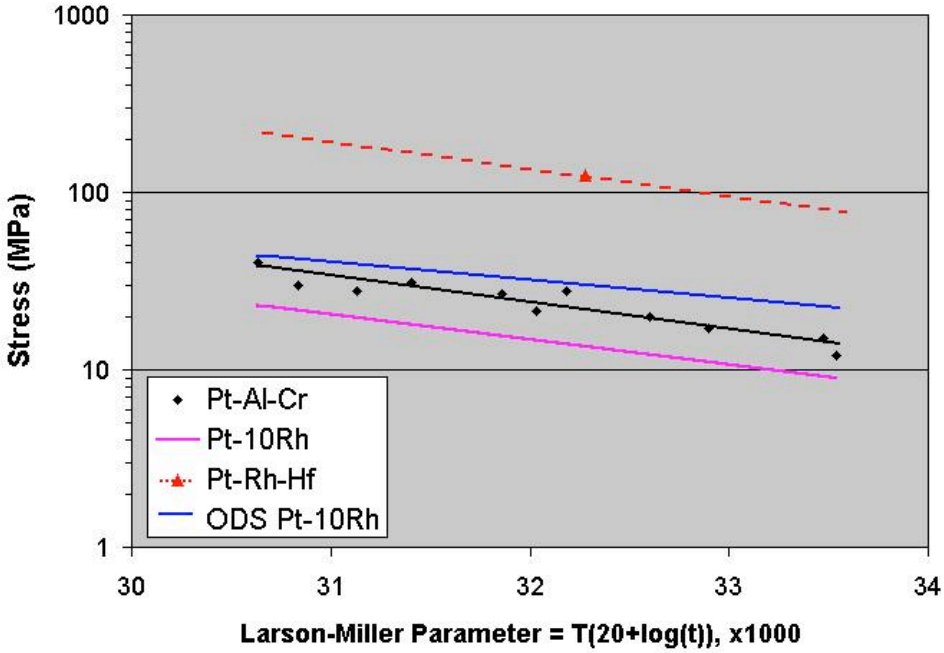

Figure 4.24 Larson-Miller plot of creep data for various Pt alloys [6,16] and for the Pt - Rh - Hf alloy. Note that all results except that for Pt - Rh - Hf have been obtained in tension, and are hence not directly comparable to the Pt - Rh - Hf point that was obtained in compression as the true stress in tensile loading continuously increases whereas in compressive loading it will continuously decrease.

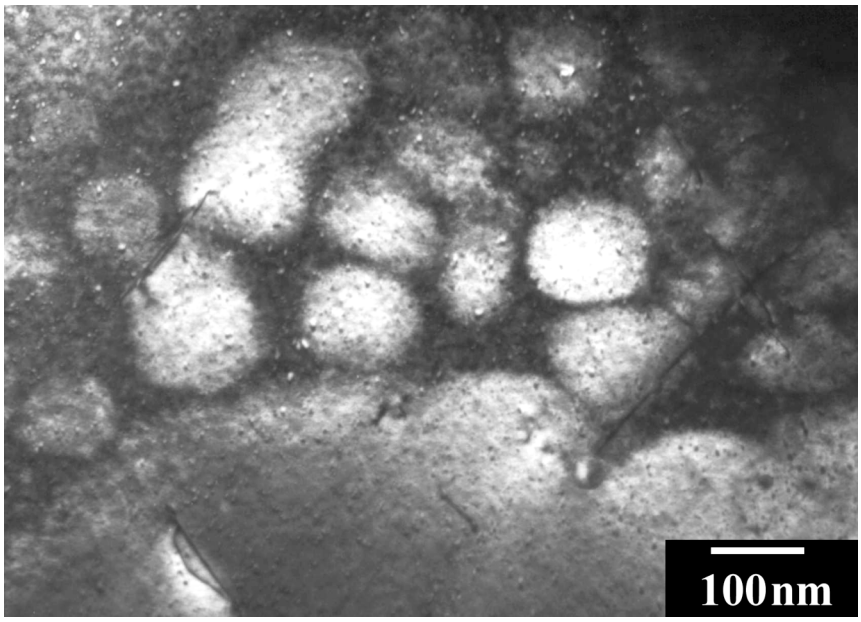

Figure 4.25 Heat-treated microstructure of the Pt - Ti - Cr alloy (**g** = 100). This was the first melt produced, which proved unsuitable for testing with the ETMT.

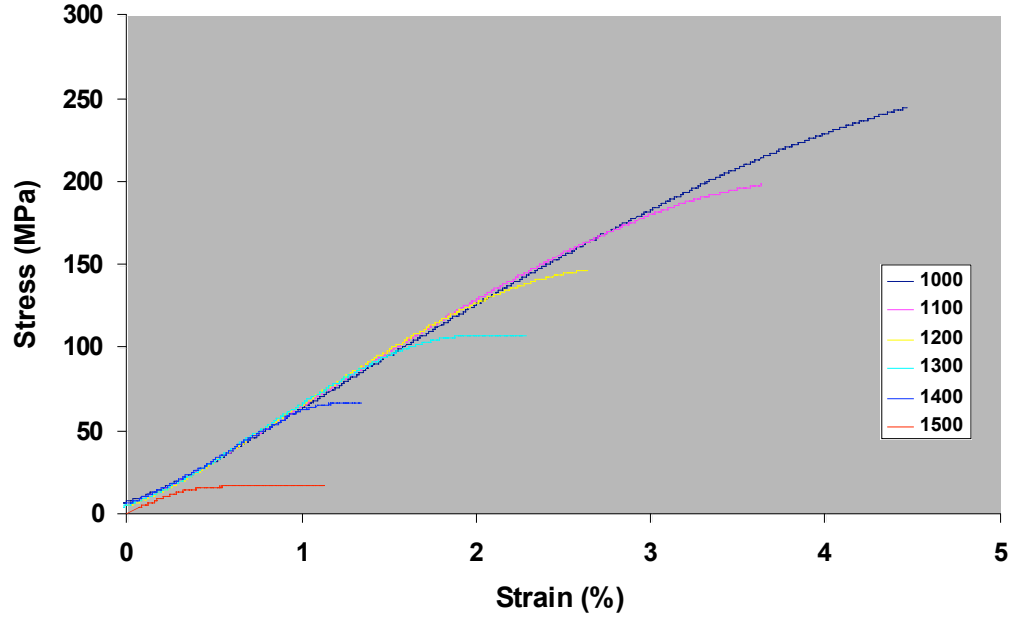

Figure 4.26 Stress-strain curves for the Pt - Ti - Cr sample tested in compression.

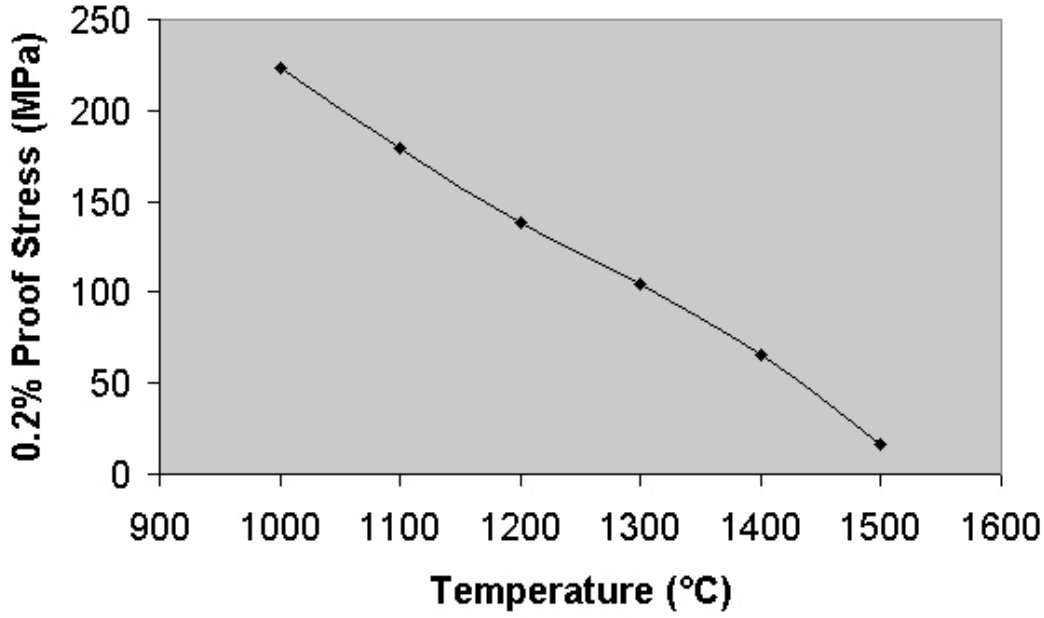

Figure 4.27 Plot of 0.2 % proof stress versus temperature for the Pt - Ti - Cr alloy.

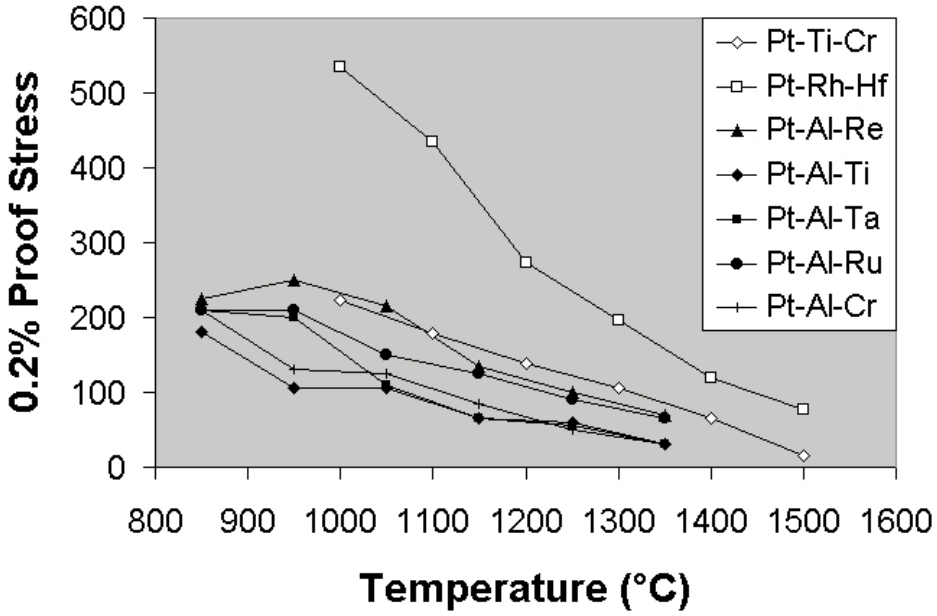

Figure 4.28 Comparison of the proof strength versus temperature for the Pt - Rh - Hf alloy, the Pt - Ti - Cr alloy and the alloys of Hill [6].

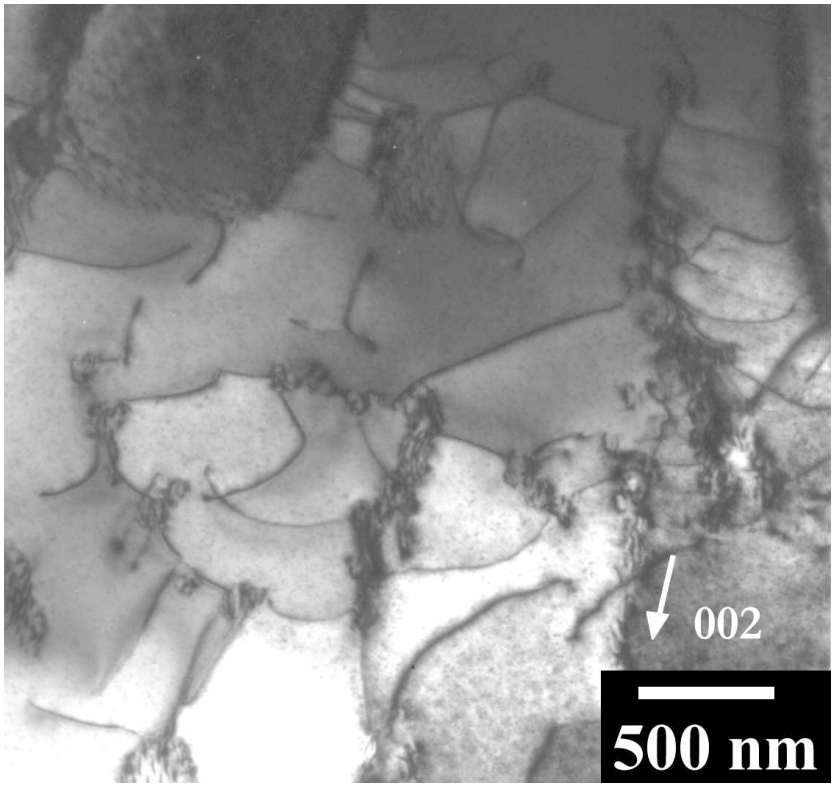

Figure 4.29 Dislocation interaction with precipitates in a Pt - Rh - Hf sample tested in 100 °C decrements from 1500 °C to 1200 °C. Note the low precipitate volume fraction, and the dislocation bowing between precipitates in the lower left of the image.

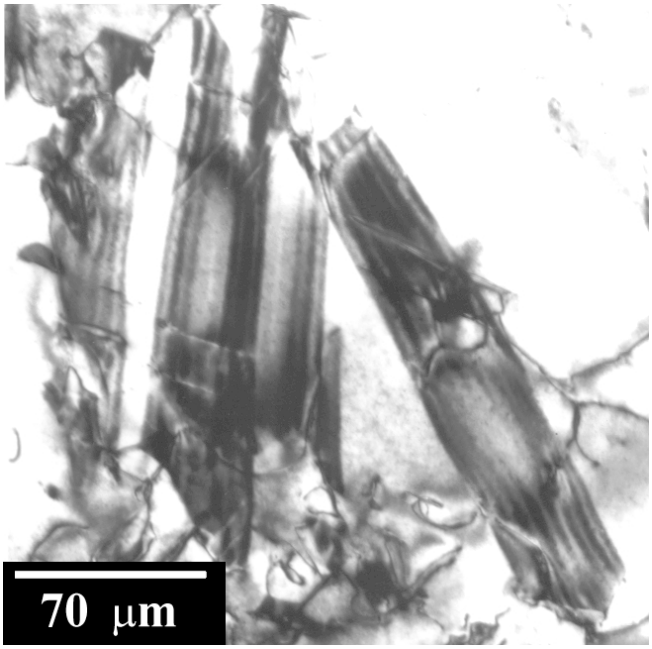

(a)

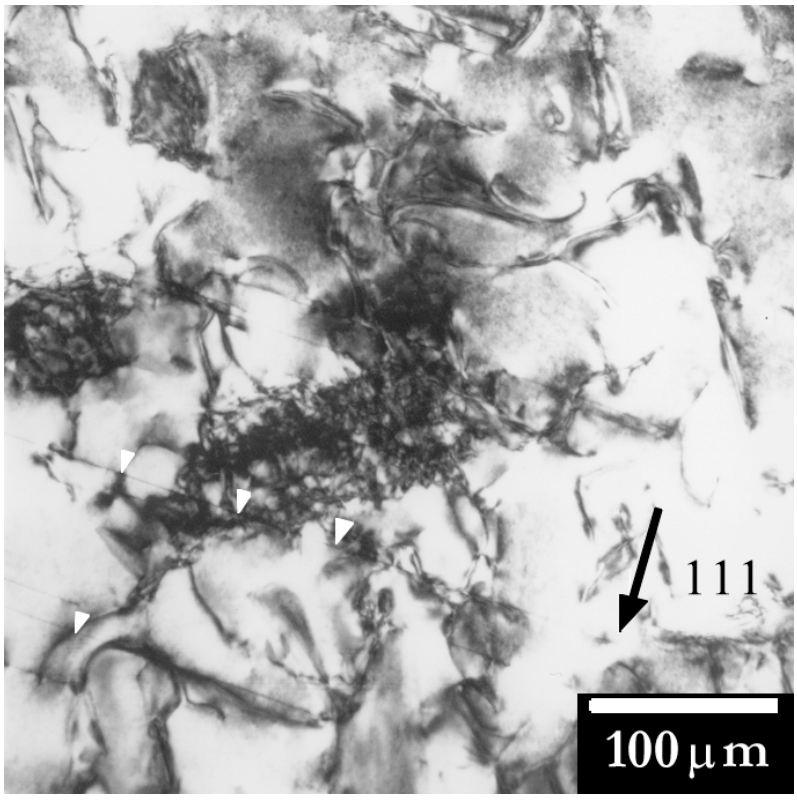

(b)

Figure 4.30 (a) Stacking faults in a Pt - Rh - Hf sample tested at 1300 °C, viewed near a {001} zone axis, and
(b) other stacking faults (arrowed) viewed edge-on down a {111} zone axis.

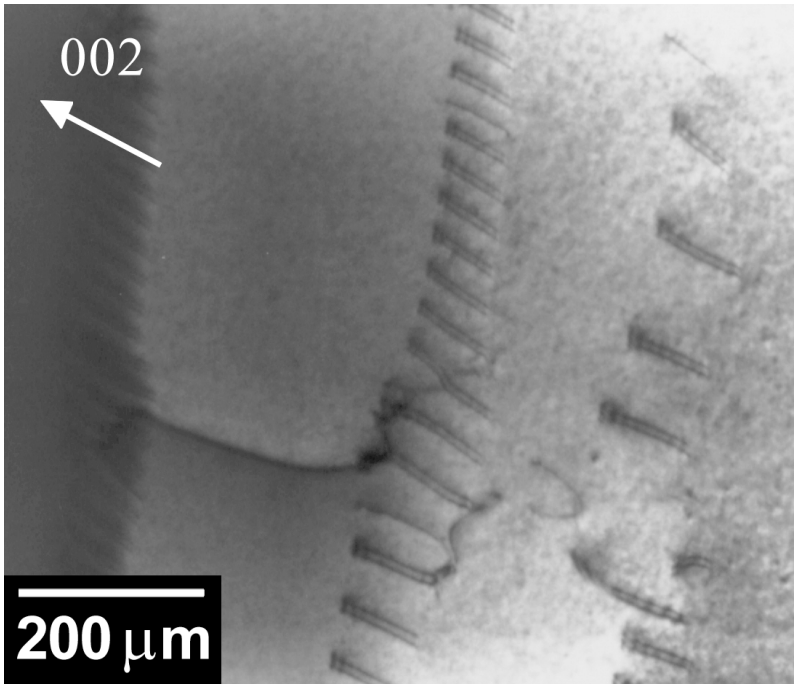

Figure 4.31 Shear bands of pairs of partial dislocations in a Pt - Rh - Hf sample tested at 1300 °C. Stacking fault contrast (alternate dark and light banding) is just visible between the pairs of partials in the lower right corner of the image.

Chapter 5 Summary of Conclusions and Further Work

5.1 Summary of conclusions

This thesis aimed to answer the question "can a high-temperature alloy be produced, using Pt as a base, utilising the γ-γ' microstructure that has been responsible for the success of the Ni-base superalloys"? Platinum was chosen as a base due to its higher melting point than Ni (1769 °C for Pt versus 1455 °C for Ni), its f.c.c. crystal structure, and its excellent oxidation resistance.

In chapter two the alloying behaviour of Pt was examined, and candidate systems investigated. In the case of the Pt - Hf and Pt - Zr systems, the binary phase equilibria of two systems were investigated as the published Pt - Zr diagram was not believed to be accurate, and no diagram had been produced for the Pt - Hf system. In both systems it was shown that, in addition to the hexagonal superlattice at 3:1 (Pt:X where X = Zr or Hf) stoichiometry, two other phases existed closer to the Pt end of the diagram. In both systems a phase was identified at approximately 19 at%(Zr or Hf) with the $L1_2$ structure, though with some substitution of Pt onto the Zr or Hf sites. In addition to this phase, another intermetallic compound Pt_8X (X=Hf or Zr) was identified, which has the same structure as Pt_8Ti, a tetragonal superlattice. The presence of this phase means it is not possible to produce a γ-γ' superalloy mimic in either binary system. The Pt - Zr diagram was modified according to the results obtained, and the Pt - Hf diagram was plotted for the first time.

In chapter three, ternary alloys from the systems Pt - Rh - Zr, Pt - Rh - Hf and Pt - Ti - Cr were investigated. In the Pt - Rh - Hf and Pt - Rh - Zr systems, it was found that the Rh_3X (X=Hf or Zr) intermetallic existed almost the whole way across the isothermal sections plotted, and that this phase was stabilised by the addition of a small amount of Rh (thought to be less than 10 at%Rh). In both systems large two-phase f.c.c. - γ' phase fields were identified, based on the (Pt,Rh) solid solution and the Rh_3X (X=Zr or Hf) intermetallic. In the Pt - Ti - Cr system, it was found that the low-temperature Pt_3Cr and congruently

melting Pt_3Ti phases (both $L1_2$) were connected across the diagram, and a temperature-composition region was identified in which a two-phase f.c.c. - $L1_2$ alloy could be produced. For each system an indication of the ternary phase equilibrium in the region 1000 °C – 1200 °C was gained.

Following on from the above results, in chapter four, two alloys were chosen for mechanical testing. A Pt - Rh - Hf alloy and a Pt - Ti - Cr alloy were melted and heat-treated, and in both alloys regions were produced consisting of $L1_2$ precipitates in a f.c.c. matrix. The mechanical properties of the Pt - Rh - Hf alloy were found to be excellent, with proof stresses higher than any other Pt alloy found. A basic creep test indicated that the creep properties exceed those of ODS single-phase Pt alloys, and other two-phase Pt alloys produced at MINTEK. The proof stress of the Pt - Ti - Cr alloy was found to be much lower than that of the Pt - Rh - Hf alloy. One serious limitation of the Pt - Rh - Hf system was identified, that being the lack of high-temperature oxidation resistance in the alloy tested.

5.2 Further Work

On the basis of the above conclusions, it appears that the Pt - Rh - Hf alloy has sufficient strength to be used at temperatures up to approximately 1300 °C – 1400 °C in structural applications. The main drawback, though, is the performance of the alloy in oxidising atmospheres at high temperature.

In the parallel work at MINTEK, the excellent oxidation resistance of Pt - Al - X alloys (where X = Ni, Ru or Ti and, to a limited extent, Re) was demonstrated, and compared to other high-temperature alloys, such as PM2000. The oxidation resistance of the Pt - Al - Ru alloy was found to be better than PM2000 at up to 1400 °C, with very little weight loss or gain after long-term exposure (on the order of 250 h) to an air atmosphere. The high-temperature proof strength of these alloys, however, was lower than the Pt - Rh - Hf alloy developed in this thesis.

It would therefore seem that an alloy based on Pt - Hf - Al may solve the oxidation problem in the Pt - Hf and Pt - Rh - Hf systems. The intermetallic phase Pt_3Al has the $L1_2$ structure at high temperature, but possesses a low-temperature variant that makes it unattractive as a strengthening phase in a binary Pt - Al alloy.

Further work should therefore focus initially on the Pt - Hf - Al ternary system, examining the phase relationships in the region between the Pt_3Al and γ' (Pt - Hf $L1_2$ intermetallic). Further to this, the effect of Al addition to the Pt - Rh - Hf alloy (or in partial substitution for the Hf) should be examined. In particular the effect of the Al on the microstructure and phase equilibria, oxidation behaviour, and mechanical properties should be examined.

Other alloying additions which stabilise the $L1_2$ phase to produce a two-phase region should be investigated. Additions such as Ir, Ru and Ni should be examined for their effect on phase equilibria, oxidation behaviour, and mechanical properties. The price of Rh fluctuates widely, so any lower-cost addition would make the alloy more attractive for use in structural components.

No successful studies on the high temperature slip behaviour of these alloys have been conducted to date. A preliminary weak-beam study attempted on the Pt - Rh - Hf alloy proved unsuccessful, but it did show that the alloys are not too dense for such an approach. It would be useful to understand whether the operative slip systems in these alloys are the same as in Ni-base superalloys, for modelling as well as alloy design purposes.

It is believed the above experiments will lead to an alloy with a combination of high-temperature strength and oxidation resistance, as well as adequate creep resistance. Work beyond this could seek to tailor the misfit of the alloy, identify a composition that solidifies as a single phase, and investigate more rigorously the mechanical properties (such as fatigue behaviour and notch sensitivity).